THESIS FOR THE DEGREE OF LICENTIATE OF ENGINEERING

Control of Energy Storage Equipped Shunt-connected Converter for Electric Power System Stability Enhancement

MEBTU BEZA

Department of Energy and Environment
CHALMERS UNIVERSITY OF TECHNOLOGY
Gothenburg, Sweden, 2012

Control of Energy Storage Equipped Shunt-connected Converter for Electric Power System Stability Enhancement
MEBTU BEZA

Devision of Electric Power Engineering
Department of Energy and Environment
Chalmers University of Technology
SE–412 96 Gothenburg
Sweden
Telephone +46 (0)31–772 1000

Printed by Chalmers Reproservice
Gothenburg, Sweden, 2012

To mum whose strength is my courage!

Control of Energy Storage Equipped Shunt-connected Converter for Electric Power System Stability Enhancement

MEBTU BEZA
Department of Energy and Environment
Chalmers University of Technology

Abstract

Flexible AC Transmission System (FACTS) controllers, both in shunt and series configuration, are widely used in the power system for power flow control, to increase the loading capability of an existing line and to increase the security of the system by enhancing its transient stability. Among the FACTS controllers family, the Static Synchronous Compensator (STATCOM) is a key device for the reinforcement of the stability in an AC power system. The STATCOM provides transient stability enhancement (TSE) and Power Oscillation Damping (POD) by controlling the voltage at the point of common coupling by using reactive power injection.
This thesis investigates the application of the STATCOM with energy storage (here named E-STATCOM) to improve the dynamic performance of the power system. In particular, the focus of this work is on the development of a cost-effective control system for the E-STATCOM for POD and TSE. This is achieved using a signal estimation technique based on a modified Recursive Least Square (RLS) algorithm, which allows a fast and selective estimation of the low-frequency electromechanical oscillations in the measured signals during power system disturbances. The output of the POD and TSE controllers are active and reactive power references that are to be injected by the E-STATCOM. The performance of the POD and TSE controllers is validated both via simulation and through experimental verification. The robustness of the control algorithm against system parameter changes is verified through the tests. It is shown that with the selected input signals for the controller (based on local measurements), the E-STATCOM is able to guarantee a uniform stability enhancement regardless of its location in the power network.

Index Terms: Signal estimation technique, electromechanical oscillation, power oscillation damping (POD), recursive least square (RLS), static synchronous compensator, energy storage, transient stability.

Acknowledgments

My sincere gratitude goes to my supervisor Assoc. Prof. Massimo Bongiorno for bringing me into the research world in the first place and for his friendly, meticulous and unreserved guidance through out the project. Thank you very much for your effort to make the best of conditions when things get frustrating and for graciously sharing all your materials. I would also like to thank my examiner Prof. Lina Bertling for reviewing the thesis and for her continuous encouragement.

This work has been funded by ELFORSK under the Elektra Project with project number ”36075” and the financial support is greatly appreciated.

My acknowledgments go to the members of the reference group Dr. Tomas Larsson (ABB Power Technologies FACTS), Prof. Lennart Ängquist (KTH), Prof. Per Norberg (Vattenfall) and Prof. Torbjörn Thiringer (Chalmers) for the nice discussions and inputs through the course of the work.

Many thanks go to all members at the division, especially Mattias, Waqas, Feng, Amin, Nicolas, Kalid and Georgios for the help during laboratory tests. I am grateful to Magnus Ellsén, Jan-Olov Lantto, Aleksander Bartnicki and Robert Karlsson for the help in the various practical issues while working in the laboratory.

Special thanks go my roommates Tarik, Amin and Mattias for making the office as much a fun place as possible.

Finally, I would like to thank my family and friends for everything.

Mebtu Beza
Gothenburg, Sweden
May, 2012

List of Acronyms

AVR	Automatic Voltage Regulator
PSS	Power System Stabilizer
FACTS	Flexible AC Transmission System
TCSC	Thyristor Controlled Series Capacitor
SSSC	Static Synchronous Series Compensator
STATCOM	Static Synchronous Compensator
E-STATCOM	Static Synchronous Compensator with Energy Storage
VSC	Voltage Source Converter
POD	Power Oscillation Damping
TSE	Transient Stability Enhancement
LPF	Low-pass Filter
RLS	Recursive Least Square
PLL	Phase-Locked Loop
PCC	Point of Common Coupling
PWM	Pulse Width Modulation
FFT	Fast Fourier Transform

Contents

Chapter 1

Introduction

1.1 Background and motivation

The continuous growth of electrical loads result in today's transmission system to be used close to their stability limits. Due to political, economic and environmental reasons, it is not always possible to build new transmission lines to relieve the overloaded lines and provide sufficient transient stability margin. In this regard, the use of Flexible AC Transmission Systems (FACTS) controllers in the transmission system can help to use the existing facilities more efficiently and improve stability of the power system [1]. One example that is a cause of concern for the stability of the power system is low-frequency electromechanical oscillation in the range of 0.2 - 2 Hz [2][3]. Sometimes, damping of the power oscillations from the generator system such as power system stabilizers (PSS) might not be sufficient to maintain the stability of the system and FACTS controllers both in shunt and series configuration have been widely used to enhance stability of the power system [4][5][6][7][8]. In the specific case of shunt-connected FACTS controllers such as Static Synchronous Compensator (STATCOM) and Static Var Compensator (SVC), Transient Stability Enhancement (TSE) and Power Oscillation Damping (POD) can be achieved by controlling the voltage at the point of common coupling (PCC) using reactive power injection. However, one drawback of the shunt configuration for this kind of applications is that the voltage at the PCC should be varied around the nominal voltage and this reduces the amount of damping that can be provided by the compensator. Moreover, the amount of injected reactive power to impact the PCC voltage depends on the short circuit impedance seen at the PCC. Injection of active power on the other hand affects the PCC voltage angle without varying the voltage magnitude significantly.

Among the shunt-connected FACTS controllers, a STATCOM has been applied both at distribution level to mitigate power quality phenomena and at transmission level for voltage control and POD [1][9][10]. Although typically used for reactive power injection only, by equipping the STATCOM with an energy storage connected to the DC-link of the converter (named E-STATCOM), a more flexible control of the transmission system can be achieved [11][12][13][14]. An installation of a STATCOM with energy storage is already found in the UK for power flow management and voltage control [15][16]. The introduction of wind energy and other distributed

generations will pave the way for more energy storage into the power system and auxiliary stability enhancement function is possible from the energy sources [17][18]. Because injection of active power is used temporarily during transient, incorporating the stability enhancement function in systems where active power injection is primarily used for other purposes [19] could be attractive.

The control of E-STATCOM for power system stability enhancement has been researched in several papers [20][21][22][23]. However, the impact of the location of the E-STATCOM on its dynamic performance is typically not treated. When active power injection is used for POD, the location of the E-STATCOM has a significant effect on its dynamic performance. Moreover, the control strategy of the device for POD is similar to the one utilized for PSS [24] where a series of wash-out and lead-lag filter links are used to generate the control input signals. However, this kind of control action is effective only at the operating point where the design of the filter links is optimized and its speed of response is limited by the frequency of the electromechanical oscillations. The problem will be more significant when more than one oscillation frequency, local and inter-area oscillations for example, with relatively equal degree of participation exist in the power system [3][24] and a proper separation of the frequency components is required.

1.2 Purpose of the thesis and main contributions

The purpose of the thesis is to investigate the application of energy storage equipped shunt-connected converter (E-STATCOM) to the transmission system. The ultimate goal is to design an effective controller for the E-STATCOM to achieve power system stability enhancement function such as POD and TSE. An optimal control algorithm for power oscillation damping with minimum active power injection will be developed and the performance of the device at different locations in the power system will be investigated. The control strategy, which is based on online estimation of the power oscillation components following system disturbances, will be designed to be robust against system parameter changes. The developed algorithms will be verified through simulation and experiment.

To the best of the author's knowledge, the main contributions of the thesis are:

- Develop a generic signal estimation algorithm based on a Recursive Least Square (RLS) algorithm with variable forgetting factor. An RLS algorithm with variable forgetting factor and frequency adaptation is implemented. This enables a fast and selective estimation of different frequency components.

- Develop an adaptive POD controller using RLS algorithm with variable forgetting factor for E-STATCOM. A POD controller is designed to adapt to system parameter changes and stability enhancement is provided irrespective of the connection point of the E-STATCOM with minimum active power injection.

1.3 Structure of the thesis

The thesis is organized into eight chapters with the first Chapter describing the background information, motivation and contribution of the thesis. Chapter 2 - 3 gives a theoretical base on problems of power system dynamics and the strategies used to improve power system stability. Chapter 2 briefly discusses stability of the power system using a simplified single machine infinite bus system and Chapter 3 describes the application of FACTS controllers, both series-connected and shunt-connected, in power systems. Among the shunt-connected FACTS controllers, E-STATCOM which will be the focus of the thesis will also be described briefly. Chapter 4 - 7 represents the main body of the thesis. Chapter 4 discusses a generic signal estimation algorithm based on RLS algorithm with variable forgetting factor. Its application for specific examples is included with validation in simulation. Chapter 5 describes the control of E-STATCOM where the current controller is improved to deal with distorted grids using the result in chapter 4. The Chapter concludes with a simulation verification of the results. Chapter 6 addresses the main objective of the work where application of E-STATCOM for POD and TSE is discussed. The POD controller is designed using the improved RLS algorithm described in Chapter 4 and its performance for system parameter changes is verified through simulation. Chapter 7 discusses the experimental verification of the results in Chapter 4 - 6. Finally, the thesis concludes with a summary of the results achieved and plans for future work in Chapter 8.

1.4 List of publications

The publications originating from the project are:

I. M. Beza and M. Bongiorno, ”Application of recursive least square (RLS) algorithm with variable forgetting factor for frequency components estimation in a generic input signal,” in *Energy Conversion Congress and Exposition (ECCE), 2012 IEEE,* Sept. 2012 [*Accepted for publication*]

II. M. Beza and M. Bongiorno, ”Improved discrete current controller for grid-connected voltage source converters in distorted grids,” in *Energy Conversion Congress and Exposition (ECCE), 2012 IEEE,* Sept. 2012 [*Accepted for publication*]

III. M. Beza and M. Bongiorno, ”A fast estimation algorithm for low-frequency oscillations in power systems,” in *Power Electronics and Applications (EPE 2011), Proceedings of the 2011-*14^{th} *European Conference on,* 30 2011-Sept. 1 2011, pp. 1-10

IV. M. Beza and M. Bongiorno, ”Power oscillation damping controller by static synchronous compensator with energy storage,” in *Energy Conversion Congress and Exposition (ECCE), 2011 IEEE,* Sept. 2011, pp. 2977-2984

The author has also contributed to the following publication not included in the thesis.

Chapter 1. Introduction

1. M. Beza and S. Norrga, ”Three-level converters with selective Harmonic Elimination PWM for HVDC application,” in *Energy Conversion Congress and Exposition (ECCE), 2010 IEEE*, Sept. 2010, pp. 3746-3753

Chapter 2

Power system modeling and stability

2.1 Introduction

To study the dynamics of the electric power system, modeling of the different power system components is necessary . Here, the model of a synchronous generator is described in detail. Simplifications to the model are made in order to simplify the mathematical model to derive the controllers. Moreover, the dynamics of the power system are studied using a simple single machine infinite bus system.

2.2 Synchronous generator model

The model of the synchronous generator could include Automatic Voltage Regulators (AVR) and Power System Stabilizers (PSS). To simplify the mathematical model, these elements are not included in the model to be described here. For a better understanding of power system stability and required simplifications for transient stability studies, a detailed model of the synchronous machine including flux dynamics in stator and rotor windings (field and damping windings) will be derived here. Figure 2.1 presents the stator and rotor circuit of a synchronous machine where a rotating dq reference frame of the generator is used to model the machine. In this dq coordinate system, the rotor field flux is synchronized to the d-axis. In this model, three damping windings, one in the d-axis (winding $1d$) and two in the q-axis ($1q$ and $2q$), that give the synchronous machine different time constants are considered.

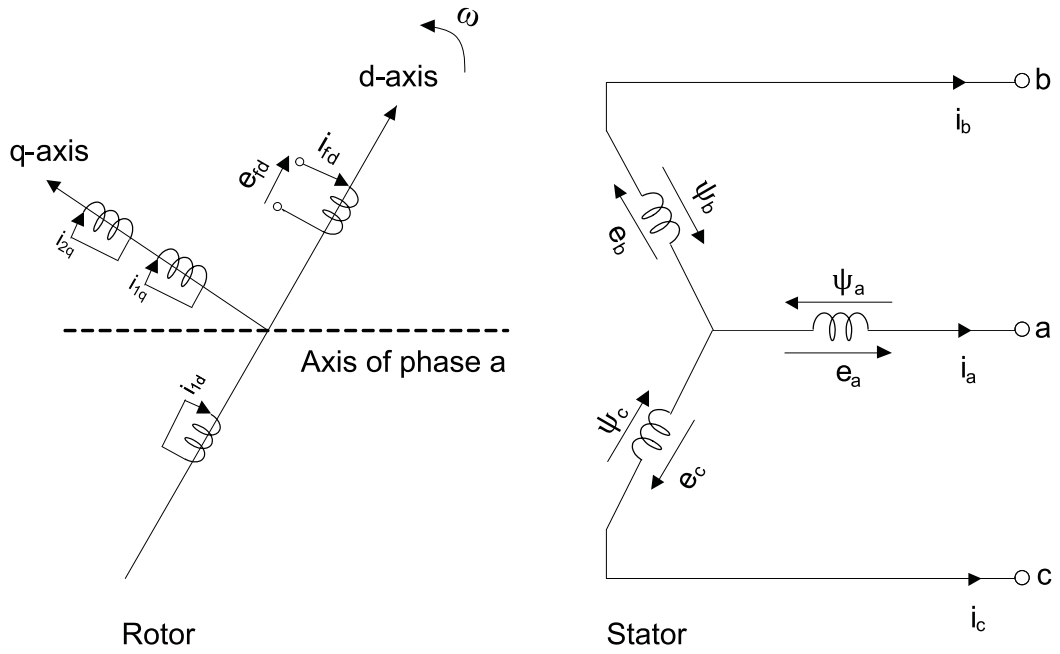

Fig. 2.1 Circuit of a synchronous machine; Left: rotor circuit with field winding (fd) and damper windings (1d, 1q, 2q), Right: Stator circuit with phase windings (a, b, c).

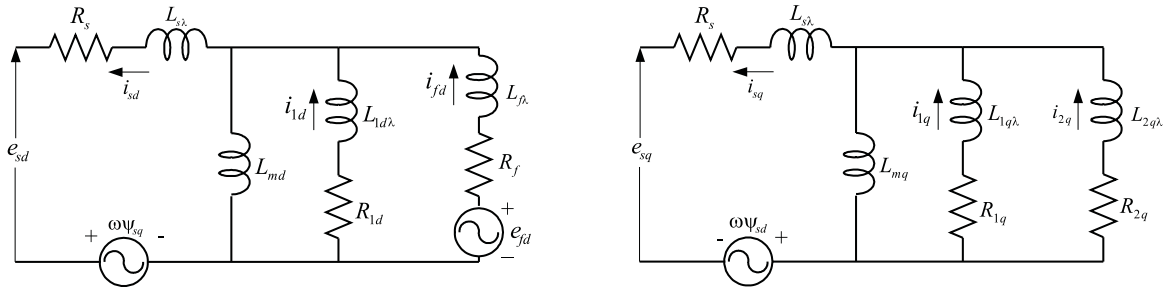

Fig. 2.2 Synchronous machine model in rotating dq-reference frame. Left: equivalent circuit in d-direction; Right: equivalent circuit in q-direction.

With the signal reference given in Fig. 2.2, the voltage equations for the stator and rotor circuit can be expressed in per-unit as [24]

$$\begin{aligned} e_{sd} &= \tfrac{1}{\omega_0}\tfrac{d\psi_{sd}}{dt} - \omega\psi_{sq} - R_s i_{sd} \\ e_{sq} &= \tfrac{1}{\omega_0}\tfrac{d\psi_{sq}}{dt} + \omega\psi_{sd} - R_s i_{sq} \\ e_{fd} &= \tfrac{1}{\omega_0}\tfrac{d\psi_{fd}}{dt} + R_f i_{fd} \\ 0 &= \tfrac{1}{\omega_0}\tfrac{d\psi_{1d}}{dt} + R_{1d} i_{1d} \\ 0 &= \tfrac{1}{\omega_0}\tfrac{d\psi_{1q}}{dt} + R_{1q} i_{1q} \\ 0 &= \tfrac{1}{\omega_0}\tfrac{d\psi_{2q}}{dt} + R_{2q} i_{2q} \end{aligned} \tag{2.1}$$

In the equations above, the signals $[e_{sd}, e_{sq}]$, $[\psi_{sd}, \psi_{sq}]$ and $[i_{sd}, i_{sq}]$ are the stator voltage, stator flux and stator current components respectively in the dq reference frame and ω_0 is the

base angular frequency. The rotor circuit flux, currents and applied field voltage are given by $[\psi_{fd}, \psi_{1d}, \psi_{1q}, \psi_{2q}]$, $[i_{fd}, i_{1d}, i_{1q}, i_{2q}]$ and e_{fd}, respectively. Assuming identical magnetizing inductances between the stator windings, field windings and damper windings, the flux linkages can be expressed as

$$\begin{aligned}
\psi_{sd} &= -L_{sd} i_{sd} + L_{md} i_{fd} + L_{md} i_{1d} \\
\psi_{sq} &= -L_{sq} i_{sq} + L_{mq} i_{1q} + L_{mq} i_{2q} \\
\psi_{fd} &= -L_{md} i_{sd} + L_{fd} i_{fd} + L_{md} i_{1d} \\
\psi_{1d} &= -L_{md} i_{sd} + L_{md} i_{fd} + L_{1d} i_{1d} \\
\psi_{1q} &= -L_{mq} i_{sq} + L_{1q} i_{1q} + L_{mq} i_{2q} \\
\psi_{2q} &= -L_{mq} i_{sq} + L_{mq} i_{1q} + L_{2q} i_{2q}
\end{aligned} \tag{2.2}$$

Denoting with the subscripts "m","'λ", "s","f" and "1" or "2", the mutual, leakage, stator, field and damper winding inductances respectively, the different inductances in (2.2) are defined as

$$\begin{aligned}
L_{sd} &= L_{md} + L_{s\lambda} \\
L_{sq} &= L_{mq} + L_{s\lambda} \\
L_{fd} &= L_{md} + L_{f\lambda} \\
L_{1d} &= L_{md} + L_{1d\lambda} \\
L_{1q} &= L_{mq} + L_{1q\lambda} \\
L_{2q} &= L_{mq} + L_{2q\lambda}
\end{aligned}$$

From (2.2), the currents can be expressed as a function of the fluxes as

$$\mathbf{i} = L^{-1} \boldsymbol{\psi} \tag{2.3}$$

where $\boldsymbol{\psi} = [\ \psi_{sd} \quad \psi_{sq} \quad \psi_{fd} \quad \psi_{1d} \quad \psi_{1q} \quad \psi_{2q}\ ]^{\mathrm{T}}$, $\mathbf{i} = [\ i_{sd} \quad i_{sq} \quad i_{fd} \quad i_{1d} \quad i_{1q} \quad i_{2q}\ ]^{\mathrm{T}}$ and the inductance matrix L is given by

$$\mathbf{L} = \begin{bmatrix}
-L_{sd} & 0 & L_{md} & L_{md} & 0 & 0 \\
0 & -L_{sq} & 0 & 0 & L_{mq} & L_{mq} \\
-L_{md} & 0 & L_{fd} & L_{md} & 0 & 0 \\
-L_{md} & 0 & L_{md} & L_{1d} & 0 & 0 \\
0 & -L_{mq} & 0 & 0 & L_{1q} & L_{mq} \\
0 & -L_{mq} & 0 & 0 & L_{mq} & L_{2q}
\end{bmatrix}$$

Using (2.1)-(2.2), the model of the synchronous generator can be derived in state space form with fluxes $\boldsymbol{\psi}$ as state variables as

$$\frac{d\boldsymbol{\psi}}{dt} = (\mathbf{L}^{-1}\mathbf{R} + \mathbf{W})\boldsymbol{\psi} + \mathbf{B}_1 e_{fd} + \mathbf{F}_1 \begin{bmatrix} e_{sd} \\ e_{sq} \end{bmatrix} \tag{2.4}$$

where the matrices $\mathbf{R}$, $\mathbf{B}_1$, $\mathbf{F}_1$ and $\mathbf{W}$ are given by

$$\mathbf{R} = \omega_0 \begin{bmatrix} R_s & 0 & 0 & 0 & 0 & 0 \\ 0 & R_s & 0 & 0 & 0 & 0 \\ 0 & 0 & -R_f & 0 & 0 & 0 \\ 0 & 0 & 0 & -R_{1d} & 0 & 0 \\ 0 & 0 & 0 & 0 & -R_{1q} & 0 \\ 0 & 0 & 0 & 0 & 0 & -R_{2q} \end{bmatrix}, \quad \mathbf{B}_1 = \omega_0 \begin{bmatrix} 0 \\ 0 \\ 1 \\ 0 \\ 0 \\ 0 \end{bmatrix}, \quad \mathbf{F}_1 = \omega_0 \begin{bmatrix} 1 & 0 \\ 0 & 1 \\ 0 & 0 \\ 0 & 0 \\ 0 & 0 \\ 0 & 0 \end{bmatrix}$$

$$\mathbf{W} = \omega_0 \begin{bmatrix} 0 & \omega & 0 & 0 & 0 & 0 \\ -\omega & 0 & 0 & 0 & 0 & 0 \\ 0 & 0 & 0 & 0 & 0 & 0 \\ 0 & 0 & 0 & 0 & 0 & 0 \\ 0 & 0 & 0 & 0 & 0 & 0 \\ 0 & 0 & 0 & 0 & 0 & 0 \end{bmatrix} \tag{2.5}$$

2.3 Equation of motion

In case of unbalances between the mechanical and the electrical torque acting on the rotor, the equation of motion for a synchronous generator can be expressed in per-unit as in (2.6) - (2.7) [24] where ω, K_{Dm}, T_{mg} and T_{eg} in per unit represent the angular speed, mechanical damping torque coefficient, mechanical torque input and electrical torque output of the generator, respectively. The inertia constant of the generator system expressed in seconds is denoted as H_{g}. The expression for the electrical torque of the generator T_{eg} depends on the model used for the synchronous generator and for the model in (2.4).

$$2H_{\mathrm{g}}\frac{d\omega}{dt} = T_{\mathrm{mg}} - T_{\mathrm{eg}} - K_{\mathrm{Dm}}\omega \tag{2.6}$$

$$\frac{d\delta_{\mathrm{g}}}{dt} = \omega_0\omega - \omega_0 \tag{2.7}$$

The angle δ_{g} represents the angular position of the generator rotor with respect to a reference frame rotating at a constant frequency of ω_0.

$$T_{\mathrm{eg}} = \psi_{sd}i_{sq} - \psi_{sq}i_{sd} \tag{2.8}$$

Expressing the currents as a function of the fluxes, the electrical torque can be expressed as

$$T_{\mathrm{eg}} = (\mathbf{C}_1\boldsymbol{\psi}\mathbf{C}_2 - \mathbf{C}_2\boldsymbol{\psi}\mathbf{C}_1)\mathbf{L}^{-1}\boldsymbol{\psi} \tag{2.9}$$

with the matrices $\mathbf{C}_1$ and $\mathbf{C}_2$ defined as

$$\mathbf{C}_1 = [\ 1 \quad 0 \quad 0 \quad 0 \quad 0 \quad 0\ ], \quad \mathbf{C}_2 = [\ 0 \quad 1 \quad 0 \quad 0 \quad 0 \quad 0\ ]$$

2.4 Transmission network model

A single line diagram of the transmission system where a synchronous generator is connected to an infinite bus is shown in Fig. 2.3. The transmission system is represented by two transformers with leakage reactances [X_{t1}, X_{t2}] and a transmission line with resistance R_{L} and reactance X_{L} at nominal frequency. The infinite bus is represented by a constant voltage $\underline{V}_i$ and a constant frequency ω_0.

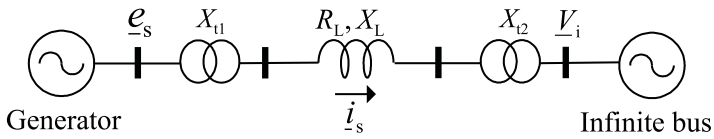

Fig. 2.3 Single line diagram of a synchronous generator connected to an infinite bus.

Taking the rotor position as a reference (see Section 2.2), the voltage vector $\underline{V}_i$ can be expressed in the dq-reference frame as [24]

$$\underline{V}_i = V_{id} + jV_{iq} = V_i \sin(\delta_{\mathrm{g}}) + jV_i \cos(\delta_{\mathrm{g}}) \tag{2.10}$$

where δ_{g} representing the angle with which the internal voltage of the generator leads the infinite bus voltage. Using the notation in Fig. 2.3, the transmission network model in the generator dq-reference frame is given by

$$\underline{e}_s = \underline{V}_i + R_{\mathrm{L}}\underline{i}_s + j\omega X_{\mathrm{e}}\underline{i}_s + \frac{X_{\mathrm{e}}}{\omega_0}\frac{d\underline{i}_s}{dt} \tag{2.11}$$

where

$$X_{\mathrm{e}} = X_{\mathrm{t1}} + X_{\mathrm{L}} + X_{\mathrm{t2}}$$

In component form, the network dynamics can be expressed as function of fluxes and rotor angle as

$$\begin{bmatrix} e_{sd} \\ e_{sq} \end{bmatrix} = \begin{bmatrix} \sin(\delta_{\mathrm{g}}) \\ \cos(\delta_{\mathrm{g}}) \end{bmatrix} V_i + \mathbf{ZCL}^{-1}\boldsymbol{\psi} + \frac{X_{\mathrm{e}}}{\omega_0}\mathbf{CL}^{-1}\frac{d}{dt}\boldsymbol{\psi} \tag{2.12}$$

where $\mathbf{Z}$ and $\mathbf{C}$ are given by

$$\mathbf{Z} = \begin{bmatrix} R_{\mathrm{L}} & -\omega X_{\mathrm{e}} \\ \omega X_{\mathrm{e}} & R_{\mathrm{L}} \end{bmatrix}, \quad \mathbf{C} = \begin{bmatrix} \mathbf{C}_1 \\ \mathbf{C}_2 \end{bmatrix} \tag{2.13}$$

2.5 Combined electrical and mechanical equations

Combining (2.1) - (2.11), the single machine infinite bus system can be represented by an 8^{th} order, time varying and nonlinear system as

$$\begin{aligned}
&\tfrac{d}{dt}\omega = -\tfrac{1}{2H_{\text{g}}}\left[(\mathbf{C}_1\boldsymbol{\psi}\mathbf{C}_2 - \mathbf{C}_2\boldsymbol{\psi}\mathbf{C}_1)\mathbf{L}^{-1}\boldsymbol{\psi} + K_{\text{Dm}}\omega\right] + \tfrac{1}{2H_{\text{g}}}T_{\text{mg}} \\
&\tfrac{d}{dt}\delta_{\text{g}} = \omega_0\omega - \omega_0 \\
&\tfrac{d\boldsymbol{\psi}}{dt} = \mathbf{A}_1^{-1}\mathbf{A}_2\boldsymbol{\psi} + \mathbf{A}_1^{-1}\mathbf{F}_1 V_i \begin{bmatrix} \sin(\delta_{\text{g}}) \\ \cos(\delta_{\text{g}}) \end{bmatrix} + \mathbf{A}_1^{-1}\mathbf{B}_1 e_{fd}
\end{aligned} \tag{2.14}$$

with $\mathbf{I}$ representing an identity matrix, $\mathbf{A}_1$ and $\mathbf{A}_2$ are given by

$$\mathbf{A}_1 = \mathbf{I} - \tfrac{X_{\text{e}}}{\omega_0}\mathbf{F}_1\mathbf{C}\mathbf{L}^{-1}, \quad \mathbf{A}_2 = \mathbf{L}^{-1}\mathbf{R} + \mathbf{W} + \mathbf{F}_1\mathbf{Z}\mathbf{C}\mathbf{L}^{-1} \tag{2.15}$$

To reduce system order and facilitate understanding of the low-frequency electromechanical dynamics, the following assumptions can be made to the model in 2.14 [24].

1. The transformer voltage terms $\frac{d\psi_{sd}}{dt}$ and $\frac{d\psi_{sq}}{dt}$ in (2.1) are neglected which removes the dynamics in the stator flux. To be consistent with this simplification, steady state relations can be used for representing the interconnecting transmission network where the network transient is ignored by neglecting $\frac{di_{\text{s}}}{dt}$ in (2.11). This simplification is applied in (2.14) by setting $\mathbf{A}_1 = \mathbf{I}$ in (2.15).

2. The change in speed is so small to affect the voltage equations in (2.1) and can be neglected ($\omega \approx$1 pu). This has a counterbalancing effect of the simplification made in the previous point as far as low-frequency rotor oscillations are concerned. This results the matrices $\mathbf{W}$ in (2.5) and $\mathbf{Z}$ in (2.13) to be constants resulting the model in (2.14) to be time invariant.

With these simplifications, the model in (2.14) will be reduced to a nonlinear, time invariant 6^{th} order system with $\mathbf{x} = [\ \omega \quad \delta_{\text{g}} \quad \psi_{fd} \quad \psi_{1d} \quad \psi_{1q} \quad \psi_{2q}\ ]^{\text{T}}$ as state variables and $\mathbf{u} = [\ T_{\text{gm}} \quad e_{fd}\ ]^{\text{T}}$ as inputs. Linearizing around a stationary operating point $(\mathbf{x}_0, \mathbf{u}_0)$, a time invariant linear model describing the dynamics of the single machine infinite bus system can be expressed in the form of

$$\frac{d\boldsymbol{\Delta}\mathbf{x}}{dt} = \mathbf{A}\boldsymbol{\Delta}\mathbf{x} + \mathbf{B}\boldsymbol{\Delta}\mathbf{u} \tag{2.16}$$

The notation $(\boldsymbol{\Delta}\mathbf{x}, \boldsymbol{\Delta}\mathbf{u})$ represents a small signal variation around an equilibrium point $(\mathbf{x}_0, \mathbf{u}_0)$. The inputs to the model in (2.16) (ΔT_{mg} and Δe_{fd}) are outputs from the prime mover and excitation system respectively which are not modeled in this analysis.

2.6 Simplified model for system stability studies

The model in (2.16) includes dynamics of the rotor flux $[\Delta\psi_{fd}, \Delta\psi_{1d}, \Delta\psi_{1q}, \Delta\psi_{2q}]$. With the assumption that the rotor flux in a generator changes slowly following a disturbance in the time frame of transient studies [24], the model in (2.16) can be further simplified to obtain a constant flux model (so called *classical model*) of a synchronous generator. In this model the rotor flux dynamics are neglected and the synchronous generator is represented by a voltage source of constant magnitude V_{g} and dynamic rotor angle δ_{g} behind a transient impedance X'_{d}. The voltage V_{g} represents the internal voltage magnitude of the synchronous generator just before disturbance. Figure 2.4 shows the equivalent circuit of the single machine infinite bus system where the resistive losses are neglected. In this equivalent circuit, the angle of the infinite bus is taken as reference.

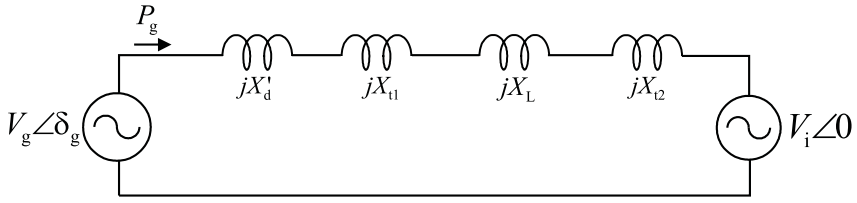

Fig. 2.4 Equivalent circuit of a single machine infinite bus system with the classical model of the synchronous generator.

Using steady state relation for the network equation, the expression for the transient electrical torque of the generator T_{eg} in pu is given by

$$T_{\mathrm{eg}} \approx P_{\mathrm{g}} = \frac{V_{\mathrm{g}} V_i \sin(\delta_{\mathrm{g}})}{X} \tag{2.17}$$

where

$$X = X'_{\mathrm{d}} + X_{\mathrm{t1}} + X_{\mathrm{L}} + X_{\mathrm{t2}}$$

Using the classical model of the synchronous generator, the electromechanical equation describing the dynamics of the single machine infinite bus system is expressed as

$$\frac{d}{dt}\begin{bmatrix} \Delta\omega \\ \Delta\delta_{\mathrm{g}} \end{bmatrix} = \begin{bmatrix} -K_{\mathrm{Dm}}/2H_{\mathrm{g}} & -K_{\mathrm{Se}}/2H_{\mathrm{g}} \\ \omega_0 & 0 \end{bmatrix} \begin{bmatrix} \Delta\omega \\ \Delta\delta_{\mathrm{g}} \end{bmatrix} + \begin{bmatrix} 1/2H_{\mathrm{g}} \\ 0 \end{bmatrix} \Delta T_{\mathrm{mg}} \tag{2.18}$$

where the synchronizing torque coefficient K_{Se} is given by

$$K_{\mathrm{Se}} = \frac{dT_{\mathrm{eg}}}{d\delta_{\mathrm{g}}} = \frac{V_{\mathrm{g}} V_{\mathrm{i}} \cos(\delta_{\mathrm{g0}})}{X}$$

To see the impact of neglecting the rotor flux dynamics, the model in (2.16) (*variable flux model*) and (2.18) (*constant flux model*) are compared for a particular operating point. A synchronous

generator rated at 2220 MVA, 24 kV and 60 Hz is used for the comparison. The parameters of the generator in per-unit are given in Table 2.1 [24]. The results for the two models are summarized in Table 2.2.

TABLE 2.1. PARAMETERS OF THE SYNCHRONOUS GENERATOR

Parameter	Value	Parameter	Value
L_{md}	1.65	R_s	0.003
L_{mq}	1.60	R_f	0.006
$L_{s\lambda}$	0.16	R_{1d}	0.0248
$L_{f\lambda}$	0.153	R_{1q}	0.0061
$L_{1d\lambda}$	0.14	R_{2q}	0.0227
$L_{1q\lambda}$	0.706	K_{Dm}	0
$L_{2q\lambda}$	0.11	$H_{\mathrm{g}}[s]$	3.5

TABLE 2.2. COMPARISON OF SYNCHRONOUS MACHINE MODEL

Results	*Variable flux model*	*Constant flux model*
System poles	-0.1731±j6.4813	±j6.387
	-37.8472, -25.1137, -0.2005, -2.0518	
Oscillation frequency, ω_{osc}	1.0319 Hz	1.0165 Hz
Damping constant at ω_{osc}	0.1713	0

The variation of the electrical torque ΔT_{eg}, which comprises of a damping torque component that varies in phase with the rotor speed variation and a synchronizing torque component that varies in phase with the rotor angle variation, for the two models can be expressed as in (2.19). The variation of the damping torque coefficient K_{De} and synchronizing torque coefficient K_{Se} as a function function of frequency is shown in Fig. 2.5 for the two models.

$$\Delta T_{\mathrm{eg}} = K_{\mathrm{Se}} \Delta\delta_{\mathrm{g}} + K_{\mathrm{De}} \Delta\omega \tag{2.19}$$

where

$$K_{\mathrm{Se}} = \mathrm{Real}\left\{\frac{\partial T_{\mathrm{eg}}}{\partial \delta_{\mathrm{g}}}\right\} \quad , \quad K_{\mathrm{De}} = \mathrm{Real}\left\{\frac{\partial T_{\mathrm{eg}}}{\partial \omega}\right\}$$

As the results in Table 2.2 and Fig. 2.5 show, including the rotor flux dynamics does not change the low-frequency electromechanical oscillation significantly. A damping torque component is provided while the synchronizing torque component is reduced slightly when compared to the case with constant rotor flux model. This is due to the impact of the damping windings, which is neglected when using the classical model. Because, the classical model provides a simplified model for power system stability analysis, this model will be used for controller design in Chapter 6. Moreover, using the classical model of the synchronous generator where the electrical damping is zero, the damping controller design will be based on a conservative assumption.

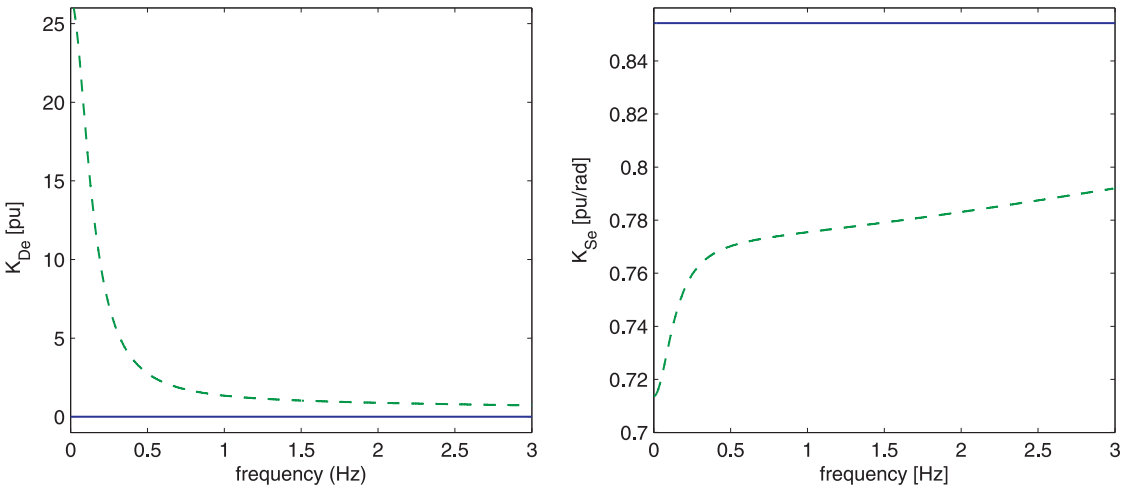

Fig. 2.5 Variation of damping (left) and synchronizing (right) torque coefficients for *variable flux model* (dashed) and *constant flux model* (solid).

2.7 Power system stability

The dynamic solution to the simplified system represented by (2.18) usually consist of low-frequency electromechanical oscillations in $\Delta\omega$ and $\Delta\delta_{\mathrm{g}}$. To investigate the transient stability of the system following disturbances, the Equal-area criterion is commonly used [25]. For this, the system in Fig. 2.4 is assumed to transfer an initial steady state power of $P_{\mathrm{g0}} = P_{\mathrm{m}}$ to the infinite bus. Figure 2.6 shows an example of the power angle curve for the system before, during and after a disturbance. A lower power output during the fault results the generator to accelerate and increase its rotor angle. When the fault is removed, the machine will start to decelerate as the power output is higher than the mechanical power input. But the generator angle δ_{g} keeps increasing until the kinetic energy gained during acceleration during the fault is totally balanced by the kinetic energy lost during deceleration, in this case at δ_3 where area ABCE = area DEFG. This implies that the first swing stability of the system depends on whether the available deceleration area DEFH of the post-fault system is greater than the acceleration area ABCD during the fault.

As an example, the single machine infinite bus system in Fig. 2.4 is simulated to study its transient stability for different fault clearing time t_{c}. In this example, the mechanical damping is assumed zero. When the fault clearing time is increased beyond the critical value $t_{\mathrm{c,cri}}$, the available deceleration area will be less than the acceleration area during fault leading to loss of synchronism of the generator. This is shown with a continuous increase of the rotor angle in Fig. 2.7.

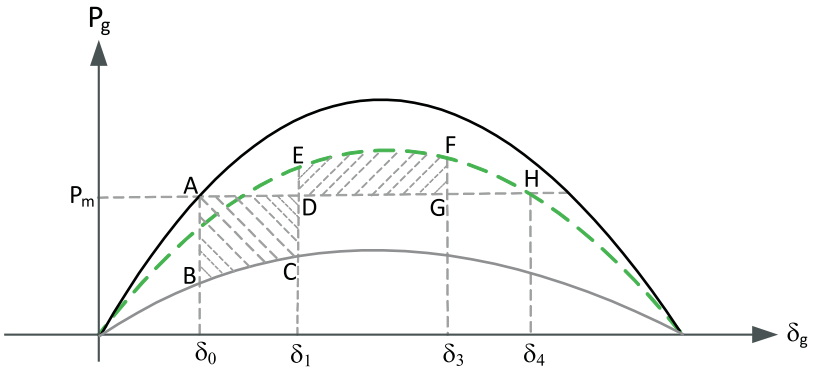

Fig. 2.6 Power angle curve for single machine infinite bus system before (black), during (gray solid) and after (dashed) fault.

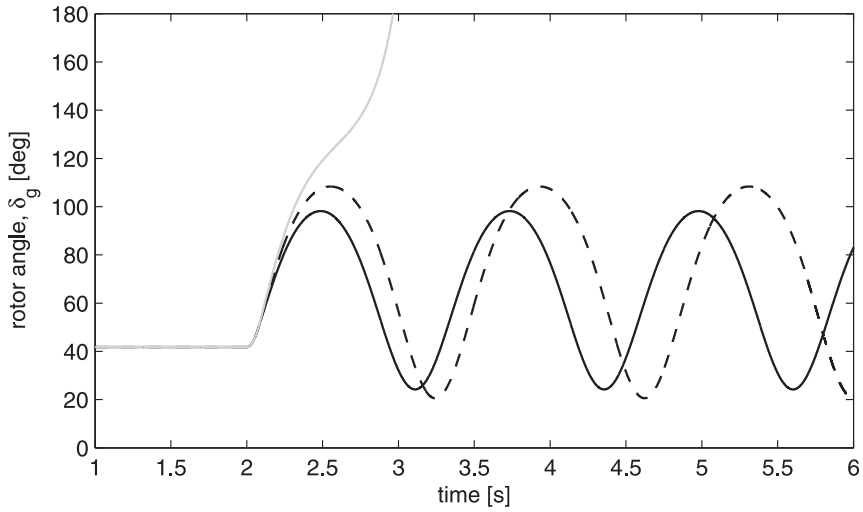

Fig. 2.7 Rotor angle variation of the generator following a three-phase fault for a fault clearing time $t_c = t_{c1}$ (black solid), t_{c2} (black dashed) and t_{c3} (gray solid) with $t_{c1} < t_{c2} < t_{c,cri} < t_{c3}$.

2.8 Conclusions

In this chapter, the modeling of a single machine infinite bus system has been presented. Starting with a detail model of the synchronous generator, the required simplifications for easier power system stability analysis have been been discussed. Using the simplified model and with the aid of the Equal-area criterion, the transient stability of the single machine infinite bus system has been described. Furthermore, the impact of the fault clearing time on the system stability has been briefly discussed. To ensure the stability of system, different enhancement functions can been applied from the generator system, controllable loads or FACTS controllers [1][24]. This is achieved by increasing the deceleration area during the first swing of the generator angle. The subsequent rotor angle oscillation can be damped by using, for instance, a PSS in the voltage controller of a synchronous generator and FACTS controllers. Using the simplified model in Fig. 2.4, the application of FACTS controllers for power system stability enhancement [6][7] will be described in the next chapter.

Chapter 3

Use of FACTS controllers in power systems

3.1 Introduction

Power electronic based devices such as FACTS controllers have been applied both at distribution and transmission level [26]. At distribution, FACTS are typically used for mitigation of power quality phenomena and for integration of renewable sources, while at transmission level, they are mainly applied for power flow enhancement and control and to improve the system stability. The use of various FACTS controllers, both series-connected and shunt-connected, for transmission system application will be briefly discussed in this chapter. The focus will be on power oscillation damping and transient stability enhancement using reactive power compensation.

3.2 Need for reactive power compensation

Transmission lines are inductive at the rated frequency (50/60 Hz). This results in a voltage drop over the line that limits the maximum power transfer capability of the transmission system. By using reactive power compensation, the loading of the transmission line can be increased close to its thermal limit with enough stability margin. This can be achieved by using fixed reactive power compensation, such as series capacitors, or controlled variable reactive power compensation. The advantage with controlled variable compensation is that it counteracts system or load changes and disturbances. FACTS controllers can provide controlled reactive power compensation to the power system for voltage control, power flow control, power oscillation damping and transient stability enhancement [1]. The application of FACTS controllers for power system stability enhancement will be described in the following sections.

3.3 Series-connected FACTS controllers

As already described in Section 2.6, the power transfer capability of long transmission lines depends on the series reactive impedance of the line. By using series capacitor, the reactive impedance of the line can be reduced and this increases the transmittable power in the transmission system [27]. Fixed capacitors provide a constant series impedance ($-jX_{\mathrm{c}}$) and makes the transmission line virtually shorter. This helps to increase the transient stability of the power system. On the other hand, a controlled variable impedance can be obtained by using series-connected FACTS controllers such as Thyristor-controlled Seried Capacitor (TCSC) and Static Synchronous Series Compensator (SSSC). This gives the advantage of power flow control and power oscillation damping that can not be achieved by uncontrolled compensation. Figure 3.1 shows the schematics of the available series-connected reactive power compensators.

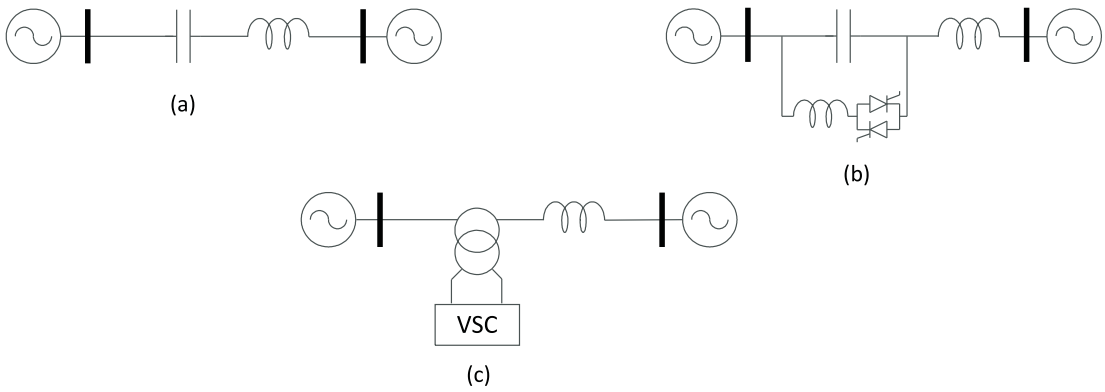

Fig. 3.1 Series-connected reactive power compensators; (a) Fixed series capacitor, (b) Thyristor-controlled Series Capacitor (TCSC), (c) Static Synchronous Series Compensator (SSSC).

To describe the increase in transient stability enhancement by series-connected reactive power compensation, the system in Fig. 2.4 is considered. If the steady state equivalent impedance of compensator is denoted by $-jX_c$, the power transfer along the line is expressed as

$$P_{\mathrm{g}} = \frac{V_{\mathrm{g}} V_{\mathrm{i}} \sin(\delta_{\mathrm{g}})}{X - X_{\mathrm{c}}} \tag{3.1}$$

Figure 3.2 shows an example of the effect of a fixed series compensation ($X_{\mathrm{c}} = 0.2X$) on the power angle curve. The transient stability margin for a given fault clearing time (at δ_1 in this case) is increased from area GFH for the uncompensated line to area $\mathrm{G_1F_1H_1}$ for the compensated line for the first swing of the generator angle. With the compensated system, the first swing of the generator angle ends at a lower angle (δ_2) than the uncompensated system (δ_3) where area DEFG = area $\mathrm{DE_1F_1G_1}$ representing the deceleration area for the two cases.

To see the effect of fixed compensation on power oscillation damping, the variation of the generator active power for fixed compensation case can be calculated as

$$\Delta P_{\mathrm{g}} \approx \frac{\partial P_{\mathrm{g}}}{\partial \delta_{\mathrm{g}}} \Delta\delta_{\mathrm{g}} + \frac{\partial P_{\mathrm{g}}}{\partial X_{\mathrm{c}}} \Delta X_{\mathrm{c}} = \frac{V_{\mathrm{g}} V_{\mathrm{i}} \cos(\delta_{\mathrm{g0}})}{\mathrm{X} - \mathrm{X_c}} \Delta\delta_{\mathrm{g}} + \frac{V_{\mathrm{g}} V_{\mathrm{i}} \sin(\delta_{\mathrm{g0}})}{(\mathrm{X} - \mathrm{X_c})^2} \Delta X_{\mathrm{c}} \tag{3.2}$$

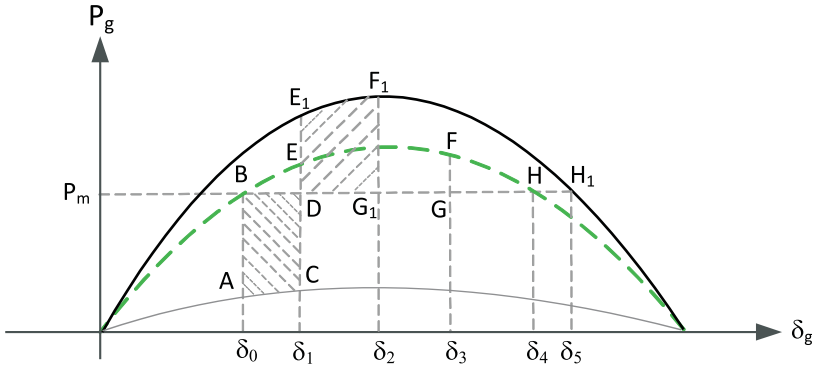

Fig. 3.2 Power angle curve for post-fault system with (black) and without (dashed) series reactive power compensation; Gray: Power angle curve during fault.

The electromechanical equation describing the single machine infinite bus system with fixed series compensation ($\Delta X_{\mathrm{c}} = 0$) becomes

$$\frac{d}{dt}\begin{bmatrix} \Delta\omega \\ \Delta\delta_{\mathrm{g}} \end{bmatrix} = \begin{bmatrix} 0 & -K_{\mathrm{Se1}}/2H_{\mathrm{g}} \\ \omega_0 & 0 \end{bmatrix}\begin{bmatrix} \Delta\omega \\ \Delta\delta_{\mathrm{g}} \end{bmatrix} + \begin{bmatrix} 1/2H_{\mathrm{g}} \\ 0 \end{bmatrix}\Delta T_{\mathrm{mg}} \tag{3.3}$$

where the synchronizing torque coefficient K_{Se1} is given by

$$K_{\mathrm{Se1}} = \frac{V_{\mathrm{g}} V_{\mathrm{i}} \cos(\delta_{\mathrm{g0}})}{\mathrm{X} - \mathrm{X_c}}$$

For simplicity, the damping from the mechanical system is neglected ($K_{\mathrm{Dm}} = 0$). It is clear from (3.3) that no damping is provided by fixed series compensation. But, the synchronizing torque coefficient K_{se1} is increased for the compensated system ($X_{\mathrm{c}} > 0$) compared to the uncompensated system ($X_{\mathrm{c}} = 0$). Therefore, the generator output power should be controlled to vary in response to the speed variation of the generator to provide power oscillation damping. This can be achieved by controlling the series compensation level X_c linearly with the generator speed variation using FACTS controllers such as TCSC as [6]

$$\Delta X_{\mathrm{c}} \approx C_1 \Delta\omega \tag{3.4}$$

The speed variation of the generator ($\Delta\omega$) for POD controller design can be measured or estimated. The algorithm used to estimate the generator speed variation for POD design will be described in the next section. The series-connected FACTS controllers provide an effective way for power flow control and system stability enhancement by controlling transmission line series impedance. One drawback associated with these devices is the complicated protection system required to deal with large short circuit currents.

3.4 Shunt-connected FACTS controllers

The voltage along a transmission can be controlled using shunt-connected FACTS controllers such as Thyristor-Controlled Reactor (TCR), Static Var Compensator (SVC) and Static Synchronous Compensator (STATCOM) [1]. The schematics of these devices is shown in Fig. 3.3.

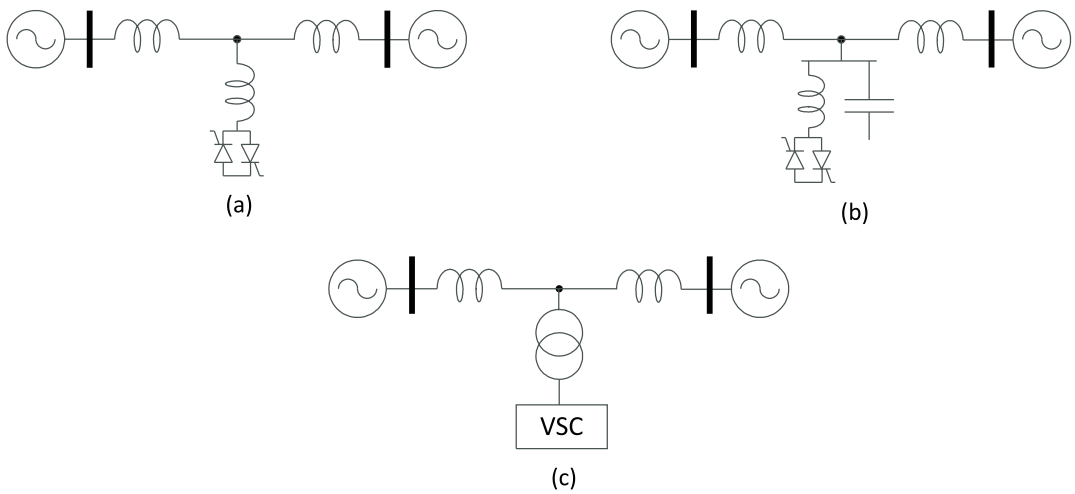

Fig. 3.3 Shunt-connected reactive power compensators; (a) Thyristor-controlled reactor (TCR), (b) Static Var Compensator (SVC), (c) Static Synchronous Compensator (SVC).

To show transient stability enhancement by shunt reactive power compensation, the system in Fig. 2.4 is considered and the shunt compensator is connected at the electrical midpoint. If the transmission end voltages are assumed equal ($V_\mathrm{g} = V_\mathrm{i}$), Figure 3.4 shows the voltage profile along the transmission line when the midpoint voltage is controlled such that $V_\mathrm{m} = V_\mathrm{i}$.

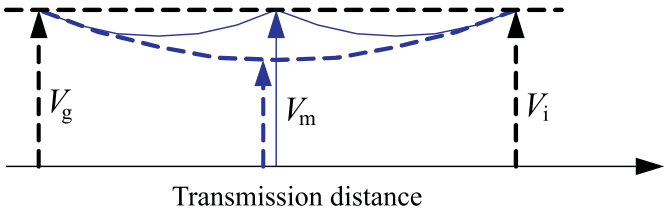

Fig. 3.4 Voltage profile along transmission line with shunt reactive power compensation (solid) and no compensation (dashed).

By controlling the PCC voltage, the power transfer over a line can be increased leading also to an increase in the transient stability. For the example in Fig. 3.4, the power flow along the transmission line is given by (3.5). For this particular case, the power angle curve for the system is shown in Fig. 3.5. The increase in stability margin for a given fault clearing time is clearly shown in the figure for the first swing of the generator angle. With the compensated system, the first swing of the generator angle ends at a lower angle (δ_2) than the uncompensated system (δ_3) where area DEFG = area $\mathrm{DE_1F_1G_1}$ representing the deceleration area for the two cases.

$$P_{\mathrm{g}} = 2\frac{V_{\mathrm{i}}V_{\mathrm{m}}\sin(\frac{\delta_{\mathrm{g}}}{2})}{X} \tag{3.5}$$

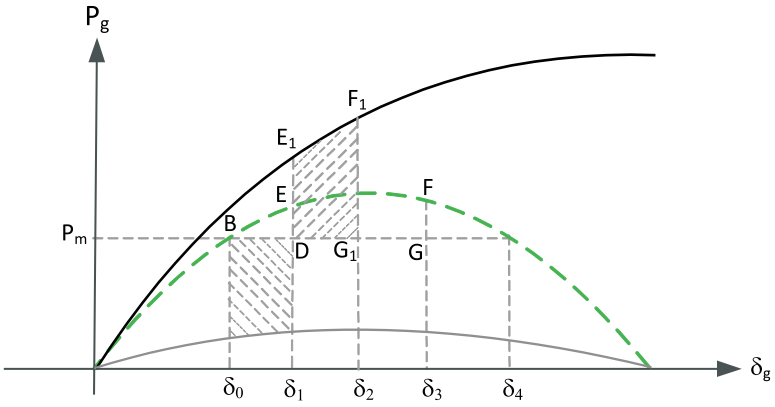

Fig. 3.5 Power angle curve for post-fault system with (black) and without (dashed) midpoint shunt reactive power compensation; Gray solid: Power angle curve during fault.

To see the effect of controlling the PCC voltage to a constant value on power oscillation damping, the variation of the generator power output for constant voltage control is calculated as

$$\Delta P_{\mathrm{g}} \approx \frac{\partial P_{\mathrm{g}}}{\partial \delta_{\mathrm{g}}}\Delta\delta_{\mathrm{g}} + \frac{\partial P_{\mathrm{g}}}{\partial V_{\mathrm{m}}}\Delta V_{\mathrm{m}} = \frac{V_{\mathrm{i}}V_{\mathrm{m}}\cos(\delta_{\mathrm{g0}}/2)}{\mathrm{X}}\Delta\delta_{\mathrm{g}} + \frac{2V_{\mathrm{i}}\sin(\delta_{\mathrm{g0}}/2)}{\mathrm{X}}\Delta V_{\mathrm{m}} \tag{3.6}$$

The electromechanical equation describing the single machine infinite bus system with constant voltage control ($\Delta V_{\mathrm{m}} = 0$) becomes

$$\frac{d}{dt}\begin{bmatrix}\Delta\omega\\ \Delta\delta_{\mathrm{g}}\end{bmatrix} = \begin{bmatrix}0 & -K_{\mathrm{Se2}}/2H_{\mathrm{g}}\\ \omega_0 & 0\end{bmatrix}\begin{bmatrix}\Delta\omega\\ \Delta\delta_{\mathrm{g}}\end{bmatrix} + \begin{bmatrix}1/2H_{\mathrm{g}}\\ 0\end{bmatrix}\Delta T_{\mathrm{mg}} \tag{3.7}$$

where the synchronizing torque coefficient K_{Se2} is given by (3.8). For comparison, the synchronizing torque coefficient K_{Se} for the uncompensated system is given by (3.9).

$$K_{\mathrm{Se2}} = \frac{V_{\mathrm{m}}V_{\mathrm{i}}\cos(\delta_{\mathrm{g0}}/2)}{X} \tag{3.8}$$

$$K_{\mathrm{Se}} = \frac{V_{\mathrm{g}}V_{\mathrm{i}}\cos(\delta_{\mathrm{g0}})}{X} \tag{3.9}$$

Again, the damping from the mechanical system is neglected. It is clear from (3.7) that no damping is provided by constant voltage control. But, the synchronizing torque coefficient is increased for the compensated system compared to the uncompensated system ($K_{\mathrm{se2}} > K_{\mathrm{se}}$). Therefore, an auxiliary controller for the shunt-connected compensator is needed to provide power oscillation damping to the system. This controller will produce a voltage magnitude modulation in order to counteract the oscillations in the generator rotor. With shunt reactive

power compensation, this is achieved by controlling ΔV_{m} linearly with the generator speed variation as [1]

$$\Delta V_{\mathrm{m}} \approx C_2 \Delta\omega \tag{3.10}$$

This requires measurement of the generator speed which in actual installation could be difficult or expensive. Another way is to estimate the speed variation of the generator from local signals such as power flow over a line or power frequency. The algorithm for estimation of the generator speed for POD design can be similarly applied for series-connected FACTS controllers. Considering the system in Fig. 2.4, the information on speed variation of the generator can be obtained from the derivative of the generator power output as

$$\frac{dP_{\mathrm{g}}}{d\delta_{\mathrm{g}}} \approx \frac{V_{\mathrm{g}} V_{\mathrm{i}} \cos(\delta_{\mathrm{g0}})}{\mathrm{X}} \Delta\omega \tag{3.11}$$

Due to the sensitivity to noise and disturbances, the derivative action can not be used directly. Conventionally, this is done instead by using a number of cascade filter links similar to the one used in PSS. With this approach, one or more washout filters are used to remove the power average and the required phase-shift (the phase-shift introduced by the derivative) is provided by a number of lead-lag filters as described in Fig 3.6.

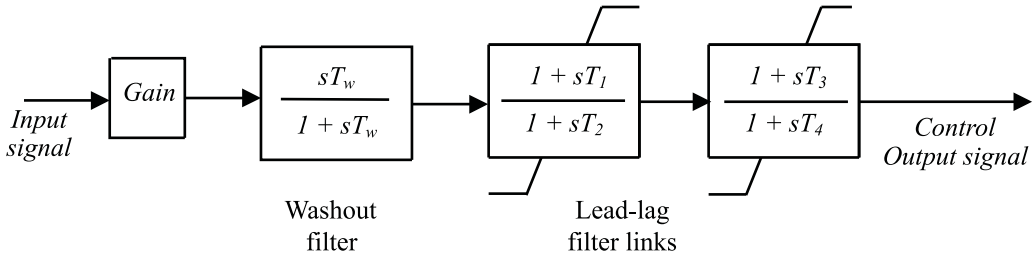

Fig. 3.6 Conventional filter set up to create a damping control input signal.

The problem with the setup in Fig. 3.6 is that the filter links must be designed for a particular oscillation frequency and the correct phase shift will be provided at that particular frequency. Moreover, as the cut-off frequency of the the washout filter to remove the average component should be well below the power oscillation frequency, it limits the speed of estimation for the required damping signal. An alternative approach is to use an estimation method based on a combination of low-pass filters (LPF) as proposed in [5]. Although this method presents better steady state and dynamic performance, its speed of response is tightly dependent on the frequency of the power oscillations to be damped (typically up to a few Hz). To overcome these drawbacks, an adaptive estimator based on an RLS algorithm with variable forgetting is proposed in this work [28]. This method will be described in Chapter 4 and its application for POD controller design will be shown in Chapter 6.

3.5 Energy storage equipped shunt-connected STATCOM

As mentioned earlier, FACTS controllers are designed to exchange only reactive power with the network in steady state. Power oscillation damping and transient stability enhancement by shunt-connected reactive power compensation is achieved by modulating the PCC voltage magnitude in order to affect the power flow over the line. The problem with this approach is that the voltage at the PCC should be kept within $\pm 10\%$ the nominal voltage [1] and this limits the level of damping or transient stability enhancement that can be achieved using only reactive power injection. Moreover, the amount of injected reactive power to impact the PCC voltage depends on the short circuit power of the grid at the connection point and might not be effective at some locations in the power system. Injection of active power on the other hand affects the voltage angle (transmission lines are effectively reactive) without varying the voltage magnitude significantly. Hence, effective power oscillation damping and transient stability enhancement can be achieved using active power injection. As the injection of active power is used temporarily during transient, this function can be incorporated in systems where the energy storage is already available for other purposes [19]. Many researches have already been made on integration of energy storage with STATCOM [11][12][13][14]. In this work, the focus will be on developing an efficient and adaptive control algorithm for power system stability enahcment using active and reactive power injection.

3.6 Conclusions

In this chapter, a brief overview of FACTS controllers for power system stability enhancement has been carried out. Both series and shunt-connected devices have been described. The impact of the controllers on the active power transferred over a transmission line as well as the system stability have been discussed. Furthermore, the need for auxiliary controllers to provide additional damping to the system has been addressed. As pointed out, in today's installations, the additional damping controllers are mainly based on the use of several filtering stages connected in cascade. To overcome the drawbacks of the POD controllers using filter links, an estimator based on RLS algorithm and its application for POD controller design will be described in the following chapters.

Chapter 4

Signal estimation techniques

4.1 Introduction

In the previous chapter, the need for signal estimation for proper design of the POD controller for a FACTS device has been discussed. The drawbacks of the methods used in actual installations, which are based on combination of cascaded filters have been briefly described. Thus, there is a need for a better estimation algorithm. In this chapter, estimation algorithm based on the use of filters will be described first. Then, the proposed signal estimation method, which is based on a RLS algorithm, will be developed. Even if the proposed algorithm can be applied for estimation of various signal components, the focus will be on estimation of low-frequency electromechanical oscillations, harmonics and sequence components in the power system.

4.2 Estimation methods

As explained in Section 3.4, a series of wash-out and lead-lag filter links connected in cascade as in Fig. 3.6 can be used to estimate power oscillation components for POD controller design in FACTS. Since the filter links are designed for a specific oscillation frequency and the correct phase shift will be provided at that particular frequency, this set up has a limitation. Moreover, as the cut-off frequency of the the washout filter to remove the average component should be well below the power oscillation frequency, it limits the speed of estimation for the required damping signal. A better approach is to use an estimation method based on a combination of low-pass filters (LPF), as proposed in [5]. Although this method presents better steady state and dynamic performance as compared to the system in Fig. 3.6, its speed of response is tightly dependent on the frequency of the power oscillations. To overcome this problem, an RLS based estimation algorithm with variable forgetting is proposed in this work [28].

To investigate the effectiveness of the considered estimation algorithms, a system consisting of a synchronous generator connected to an infinite bus through a transmission system as in Fig 4.1 is considered. As an example, a three phase line fault is applied to this system at $t = 20$ s with a subsequent line disconnection to clear the fault after 100 ms. This results in a low-frequency

oscillation in the transmitted active power as shown in Fig. 4.2.

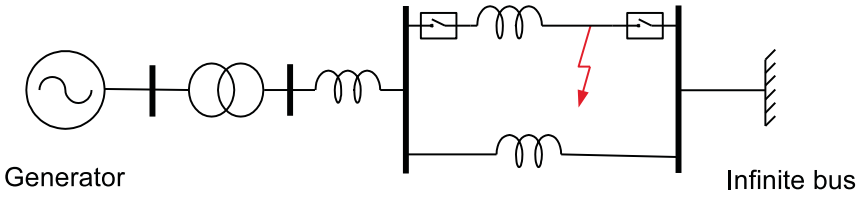

Fig. 4.1 A simple power system to model low-frequency power oscillation.

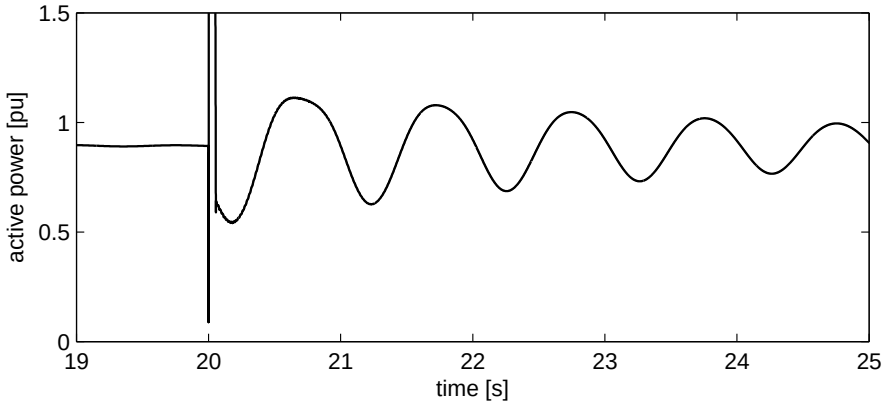

Fig. 4.2 Transmitted active power from the generator. Fault occurred at 20 s and cleared after 100 ms.

The purpose of the estimation method is to extract the oscillatory component of the input power signal for POD controller design. For this particular case, the generator output power (p), which is used as input for the estimation algorithm can be modeled as the sum of an average (P_0) and oscillatory component (P_{osc}) as

$$p(t) = P_0(t) + P_{\text{osc}}(t) = P_0(t) + P_{\text{ph}}(t)\cos[\omega_{\text{osc}}t + \varphi(t)] \tag{4.1}$$

The oscillatory component, P_{osc}, is expressed in terms of its amplitude (P_{ph}), frequency (ω_{osc}) and phase (φ). Observe that even if the specific application to power oscillations are considered in this section, the analysis is valid in the generic case of signal estimation [29]. In this section, the LPF based and RLS based methods will be described when used for estimation of low-frequency power oscillation components. The limitation of the LPF based method when fast estimation is needed will be shown. Further improvements to the RLS based method to increase its dynamic performance will be described in the next section.

4.2.1 Low-pass Filter (LPF) based method

Denoting $\underline{P}_{\text{ph}} = P_{\text{ph}}e^{j\varphi}$ as the complex phasor of the oscillatory component and $\theta_{\text{osc}}(t) = \omega_{\text{osc}}t$ as the oscillation angle, the active power in (4.1) can be rewritten as

$$p(t) = P_0(t) + \text{Real}\left[\underline{\text{P}}_{\text{ph}}(\text{t})\text{e}^{\text{j}\theta_{\text{osc}}(\text{t})}\right] = \text{P}_0(\text{t}) + \frac{1}{2}\underline{\text{P}}_{\text{ph}}(\text{t})\text{e}^{\text{j}\theta_{\text{osc}}(\text{t})} + \frac{1}{2}\underline{\text{P}}^*_{\text{ph}}(\text{t})\text{e}^{-\text{j}\theta_{\text{osc}}(\text{t})} \tag{4.2}$$

The expression in (4.2) separates the input signal into three frequency components (having characteristic frequency $0, \omega_{\text{osc}}$, and $-\omega_{\text{osc}}$) where the average P_0 and the phasor $\underline{P}_{\text{ph}}$ are slowly varying signals. By rearranging (4.2) and applying low-pass filtering, the estimate for the average $\tilde{P}_0$, the phasor $\underline{\tilde{P}}_{\text{ph}}$ and the oscillatory component $\tilde{P}_{\text{osc}}$ can be extracted from the input signal as [5][27]

$$\tilde{P}_0(t) = H_0\{p(t) - \tilde{P}_{\text{osc}}(t)\} \tag{4.3}$$

$$\underline{\tilde{P}}_{\text{ph}}(t) = H_{\text{ph}}\{[2p(t) - 2\tilde{P}_0(t) - \underline{\tilde{P}}^*_{\text{ph}}(t)e^{-j\theta_{\text{osc}}(t)}]e^{-j\theta_{\text{osc}}(t)}\} \tag{4.4}$$

$$\tilde{P}_{\text{osc}}(t) = \frac{1}{2}\underline{\tilde{P}}_{\text{ph}}(t)e^{j\theta_{\text{osc}}(t)} + \frac{1}{2}\underline{\tilde{P}}^*_{\text{ph}}(t)e^{-j\theta_{\text{osc}}(t)} \tag{4.5}$$

where H_0 and H_{ph} represent the transfer function of the low-pass filters to extract the average and the phasor component, respectively. The block diagram of this method is shown in Fig. 4.3. For the various notations, a signal or parameter $\tilde{x}$ represents an estimate of the actual value x.

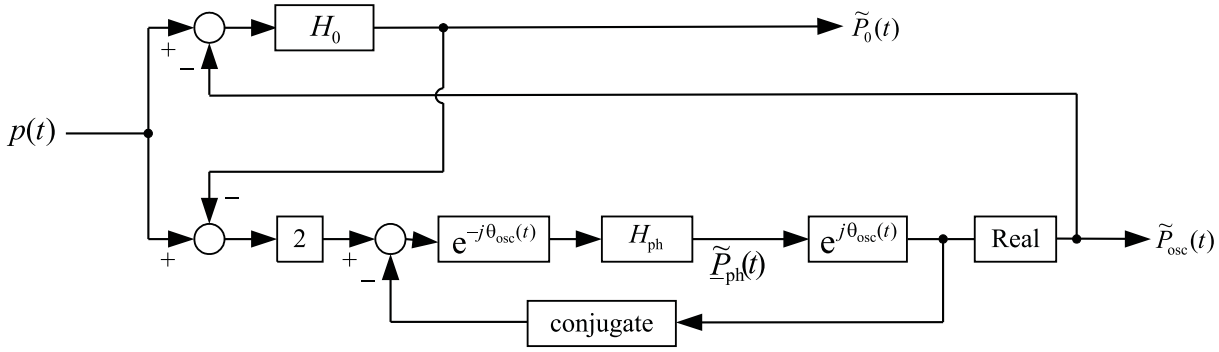

Fig. 4.3 Block diagram of the LPF based estimation algorithm.

In order to evaluate the dynamic performance of the LPF based estimation algorithm, a first order low-pass filter with cut-off frequency α_{LPF} is used for the filters in (4.3) - (4.4) as

$$H_0(s) = H_{\text{ph}}(s) = \frac{\alpha_{\text{LPF}}}{s + \alpha_{\text{LPF}}} \tag{4.6}$$

To separate the average and oscillatory components, it is necessary that the cut-off frequency α_{LPF} is smaller than the oscillation frequency ω_{osc} [5]. The dynamic performance of the LPF based method is a function of the cut-off frequency α_{LPF}. By increasing the magnitude of α_{LPF}, a faster estimation can be obtained at the cost of its frequency selectivity. To observe this, the algorithm in (4.3)-(4.5) is expressed in state space form as [28][27]

$$\frac{d}{dt}\begin{bmatrix}\tilde{P}_0\\ \tilde{P}_{\text{osc}}\\ \tilde{P}_\beta\end{bmatrix} = \begin{bmatrix}-\alpha_{\text{LPF}} & -\alpha_{\text{LPF}} & 0\\ -2\alpha_{\text{LPF}} & -2\alpha_{\text{LPF}} & -\omega_{\text{osc}}\\ 0 & \omega_{\text{osc}} & 0\end{bmatrix}\begin{bmatrix}\tilde{P}_0\\ \tilde{P}_{\text{osc}}\\ \tilde{P}_\beta\end{bmatrix} + \begin{bmatrix}\alpha_{\text{LPF}}\\ 2\alpha_{\text{LPF}}\\ 0\end{bmatrix} p(t) \tag{4.7}$$

where $\tilde{P}_\beta$ is a signal orthogonal to the oscillatory component $\tilde{P}_{\text{osc}}$. From (4.7), the dynamic response of the LPF based method can be investigated. As an example, the signal $p(t)$ is assumed to contain an average and a 1 Hz oscillatory component. The cut-off frequency α_{LPF} is then varied from 0 Hz to 1 Hz in steps of 0.05 Hz to see the estimator's performance. The poles for the transfer function from the input p to the estimate of the oscillatory component $\tilde{P}_{\text{osc}}$ is shown in Fig. 4.4. As clearly seen from the figure, the angular position of the poles from the imaginary axis starts to decrease for $\alpha_{\text{LPF}} > 0.4\omega_{\text{osc}}$ (marked in gray color for clarity) indicating that its dynamic performance starts to deteriorate. The bandwidth of the filter is typically selected to be one decade smaller than the frequency component to be estimated (for the specific case, α_{LPF} = 0.628 rad/s).

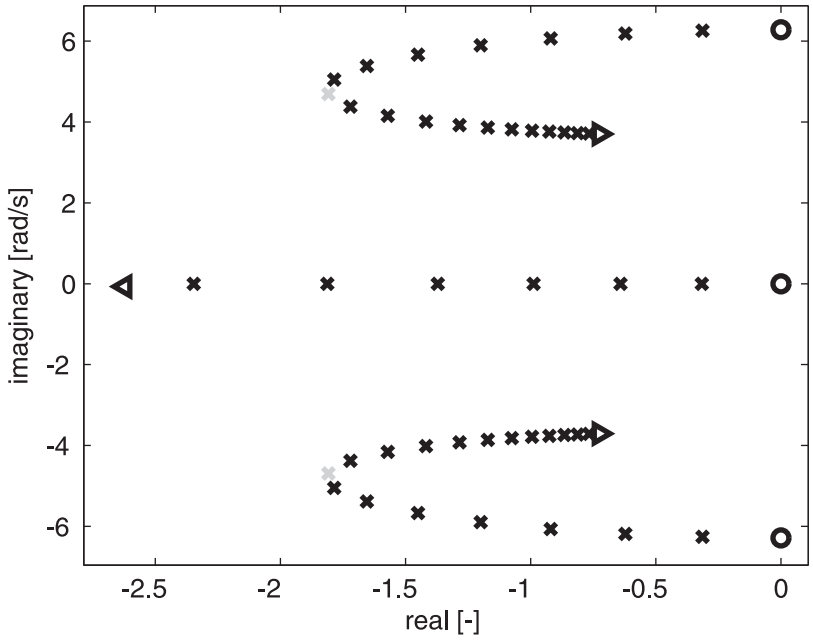

Fig. 4.4 Movement of poles for the transfer function from $p(t)$ to $\tilde{P}_{\text{osc}}(t)$ as α_{LPF} varies from 0 Hz to 1 Hz in steps of 0.05 Hz; Poles start at '$\circ$' and move towards '$\triangleright$'.

4.2.2 Recursive Least Square (RLS) based method

A Recursive Least Square (RLS) algorithm is a time-domain approach (an adaptive filter in frequency domain) used to estimate signals based on a given model of the investigated system. Consider a generic input signal (either real or complex) y, modeled as the sum of its estimate $\tilde{y}$ and the estimation error d as in (4.8)

$$y(k) = \tilde{y}(k) + d(k) = \mathbf{\Phi}(k)\tilde{\mathbf{h}}(k-1) + d(k) \tag{4.8}$$

where $\tilde{\mathbf{h}}$ is the estimated state vector and $\mathbf{\Phi}$ is named the observation matrix that depends on the model of the signal. An update of the estimation state vector $\tilde{\mathbf{h}}$ is developed using the RLS algorithm in discrete time as

$$\tilde{\mathbf{h}}(k) = \tilde{\mathbf{h}}(k-1) + \mathbf{G}(k)\left[y(k) - \mathbf{\Phi}(k)\tilde{\mathbf{h}}(k-1)\right] \tag{4.9}$$

The gain matrix $\mathbf{G}$ is given by

$$\mathbf{G}(k) = \frac{\mathbf{R}(k-1)\mathbf{\Phi}^T(k)}{\lambda + \mathbf{\Phi}(k)\mathbf{R}(k-1)\mathbf{\Phi}^T(k)} \tag{4.10}$$

with the covariance matrix $\mathbf{R}$ expressed as

$$\mathbf{R}(k) = \left[\mathbf{I} - \mathbf{G}(k)\mathbf{\Phi}(k)\right]\mathbf{R}(k-1)/\lambda \tag{4.11}$$

The term λ is named forgetting factor and $\mathbf{I}$ is an identity matrix. As can be seen in (4.9) - (4.11), the algorithm is performed recursively starting from an initial invertible matrix $\mathbf{R}(0)$ and initial state vector $\tilde{\mathbf{h}}(0)$ [30]. The RLS algorithm minimizes the cost function ξ in (4.12).

$$\xi(k) = \sum_{n=0}^{k} |d(n)|^2 \lambda^{k-n} \tag{4.12}$$

In steady state, the estimation speed of the RLS algorithm in rad/s is given by (4.13) [28] where α_{RLS} is the bandwidth of the estimator and T_s is the sampling time.

$$\alpha_{\mathrm{RLS}} = \frac{1-\lambda}{T_\mathrm{s}} \tag{4.13}$$

Depending on the speed of estimation required, the forgetting factor can be chosen accordingly. For a constant forgetting factor, the matrices in (4.10) - (4.11) converge to their steady state values depending on the observation matrix $\mathbf{\Phi}$ and the estimation speed will be decided by the value of the forgetting factor according to (4.13). After the RLS algorithm has converged, it becomes linear and time invariant.

Using the same input signal $p(t)$ as in (4.1), the model of the input signal can be expressed as

$$p(t) = P_0(t) + P_d\cos(\theta_{\text{osc}}(t)) - P_q\sin(\theta_{\text{osc}}(t)) \tag{4.14}$$

where

$$P_d = P_{\mathrm{ph}}(t)\cos(\varphi), \quad P_q = P_{\mathrm{ph}}(t)\sin(\varphi) \tag{4.15}$$

For estimation of low-frequency power oscillation, the RLS algorithm (4.8) - (4.11) can be applied by routine with

$$\tilde{\mathbf{h}}(k) = \begin{bmatrix} \tilde{P}_0(k) & \tilde{P}_\mathrm{d}(k) & \tilde{P}_\mathrm{q}(k) \end{bmatrix}^\mathrm{T} \tag{4.16}$$

$$\mathbf{\Phi}(k) = \begin{bmatrix} 1 & \cos(\theta_\mathrm{osc}(k)) & -\sin(\theta_\mathrm{osc}(k)) \end{bmatrix} \tag{4.17}$$

From the estimated state vector $\tilde{\mathbf{h}}$, the oscillatory component estimate ($\tilde{P}_\mathrm{osc}$) can be obtained as

$$\tilde{P}_\mathrm{osc}(k) = \tilde{P}_\mathrm{ph}(k)\cos(\theta_\mathrm{osc}(k) + \tilde{\varphi}(k)) \tag{4.18}$$

where the amplitude and phase estimates of the oscillatory component expressed as

$$\tilde{P}_\mathrm{ph}(k) = \sqrt{\left[\tilde{P}_\mathrm{d}(k)\right]^2 + \left[\tilde{P}_\mathrm{q}(k)\right]^2}, \qquad \tilde{\varphi}(k) = \tan^{-1}\left[\frac{\tilde{P}_\mathrm{q}(k)}{\tilde{P}_\mathrm{d}(k)}\right] \tag{4.19}$$

As described earlier, the RLS algorithm becomes linear and time invariant in steady state. Thus, the steady state model of the RLS estimator will be derived and its performance will be compared with the LPF based method. For this, the algorithm in (4.8) - (4.18) in steady state can be expressed in state space form as [28][27]

$$\frac{d}{dt}\begin{bmatrix} \tilde{P}_0 \\ \tilde{P}_\mathrm{osc} \\ \tilde{P}_\beta \end{bmatrix} = \begin{bmatrix} -\alpha_0 & -\alpha_0 & 0 \\ -\alpha_\mathrm{a} & -\alpha_\mathrm{a} & -\omega_\mathrm{osc} \\ -\alpha_\mathrm{b} & -\alpha_\mathrm{b}+\omega_\mathrm{osc} & 0 \end{bmatrix}\begin{bmatrix} \tilde{P}_0 \\ \tilde{P}_\mathrm{osc} \\ \tilde{P}_\beta \end{bmatrix} + \begin{bmatrix} \alpha_0 \\ \alpha_\mathrm{a} \\ \alpha_\mathrm{b} \end{bmatrix} p(t) \tag{4.20}$$

With $\alpha_\mathrm{RLS} = (1-\lambda_\mathrm{ss})/T_\mathrm{s}$ and $\xi = \alpha_\mathrm{RLS}/\omega_\mathrm{osc}$, the constants α_0, α_a and α_b are given by

$$\alpha_0 = \alpha_\mathrm{RLS}(1+\xi^2), \qquad \alpha_\mathrm{a} = (2-\xi^2)\alpha_\mathrm{RLS}, \qquad \alpha_\mathrm{b} = -3\xi\alpha_\mathrm{RLS}$$

From (4.20), the dynamic response of the RLS based method can be investigated. Considering the same signal $p(t)$ with an average and a 1 Hz oscillatory component, α_RLS is varied from 0 Hz to 1 Hz in steps of 0.05 Hz to see the estimator's performance. The poles for the transfer function from the input p to the estimate of the oscillatory component $\tilde{P}_\mathrm{osc}$ is shown in Fig. 4.5. As clearly seen from the figure, the angular position of the poles from the imaginary axis increases continuously unlike the LPF method. This indicates that the speed of response of the RLS based method increase with higher value of α_RLS (or correspondingly lower value of λ) unlike the LPF based method.

When low bandwidth in the estimation (i.e. for $\alpha_\mathrm{RLS} = \alpha_\mathrm{LPF} << \omega_\mathrm{osc}$) is acceptable, the two methods present similar dynamic performance [28]. This can be seen from the state space models where (4.20) is reduced to (4.7). If fast estimation is needed, the LPF based method presents poor dynamic performance unlike the RLS-based method. Therefore, the RLS algorithm can be used to obtain faster estimation during rapid changes of the input signal and hence will be the preferred method in this work.

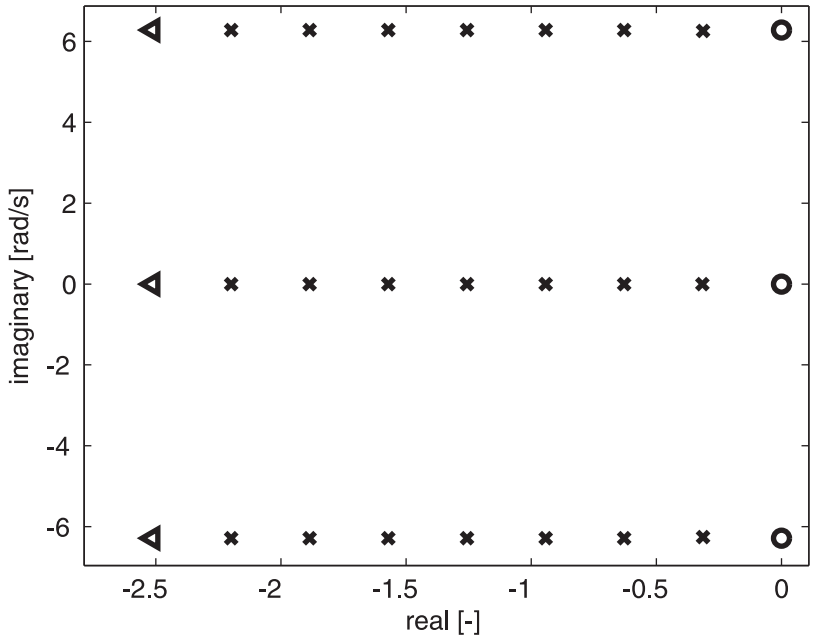

Fig. 4.5 Movement of poles for the transfer function from $p(t)$ to $\tilde{P}_{\text{osc}}(t)$ as α_{RLS} varies from 0 Hz to 1 Hz in steps of 0.05 Hz; Poles start at '$\circ$' and move towards '$\triangleright$'.

Even if faster estimation is obtained using RLS algorithm with lower λ, its frequency selectivity should be investigated. For this purpose, the bode diagram of the transfer function from the input $p(t)$ to the oscillatory estimate $\tilde{P}_{\text{osc}}$ is shown in Fig. 4.6. For all the cases, the bode diagram has a 1 pu gain and 0° phase at required the frequency and a gain of 0 pu at the unwanted oscillation frequency. But, with increasing estimation speed (decreasing λ), the frequency selectivity of the algorithm reduces. This requires for a modification in the conventional RLS algorithm to achieve both fast estimation and good frequency selectivity.

4.3 Improved RLS based method

As already described, the estimation speed of the RLS based method with fixed forgetting factor λ cannot be changed during fast transients. Moreover, its performance in steady state highly depends on knowledge of system parameters expressed in the observation matrix $\mathbf{\Phi}$. This calls for modifications in the conventional RLS algorithm in order to achieve faster estimation during transients without compromising its frequency selectivity in steady state as will be described in this section.

4.3.1 Variable forgetting factor

In the conventional RLS based method, a large forgetting factor results in low estimation speed with high frequency selectivity. Likewise, a small value of the forgetting factor results in the estimator to be fast but less selective [31]. Therefore, to achieve fast estimation when a change

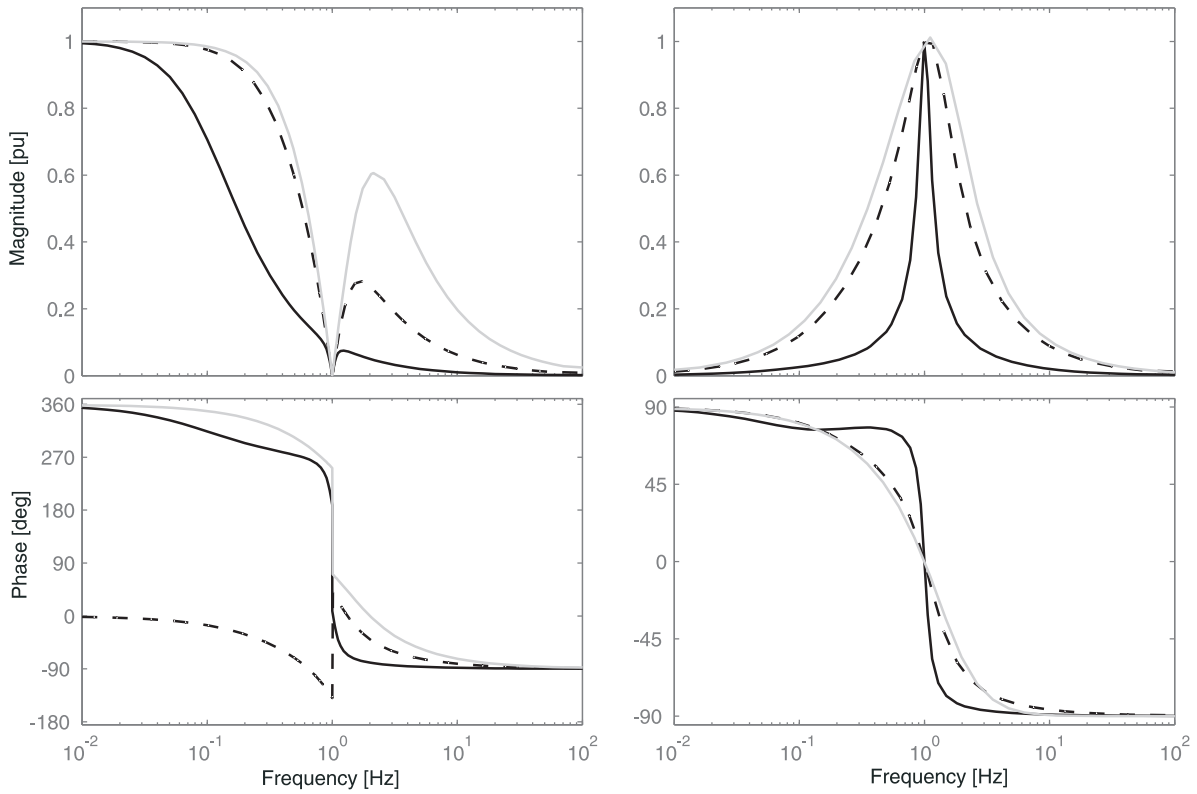

Fig. 4.6 Bode diagram for the transfer function from $p(t)$ to $\tilde{P}_0(t)$ (left) and $p(t)$ to $\tilde{P}_{\text{osc}}(t)$ (right); Forgetting factor $\alpha_{\text{RLS}} = 0.1$ Hz (black solid), $\alpha_{\text{RLS}} = 0.5$ Hz (black dashed) and $\alpha_{\text{RLS}} = 1.0$ Hz (gray solid).

occurs in the input signal, the gain matrix of the RLS algorithm $\mathbf{G}$ in (4.10) must be increased for a short time. This can be done by resetting the covariance matrix $\mathbf{R}$ to a high value [30] [32]. In this method, the covariance matrix to be used for the reset is chosen by trial and error and has to be selected case by case. Moreover, the behavior of the estimator response during transient is difficult to predict. An alternative solution is to use a variable forgetting factor [28]. With this approach, λ is varied in a controlled way depending on the input and this helps to know the behavior of the estimator's response during transient and steady state.

When the RLS algorithm is in steady state, its bandwidth is determined by the steady state forgetting factor (λ_{ss}) according to (4.13). If a fast change is detected in the input (i.e. if the absolute error $|d|$ in (4.8) exceeds a pre-defined threshold d_{th}), λ can be modified to a smaller value, here denoted as "transient forgetting factor (λ_{tr})". Thus, by using the properties of the step response for a high-pass filter, λ will be slowly increased back to its steady state value λ_{ss} in order to guarantee the selectivity of the algorithm. The parameters λ_{ss}, λ_{tr} as well as the time constant for the high-pass filter τ_{hp} determine the performance of the RLS algorithm in the transient conditions. Figure 4.7 shows the resetting method for the forgetting factor and its variation in time when a change is detected in the input signal.

Once the value of λ_{ss} is chosen based on the steady state performance requirement of the algorithm, the value of λ_{tr} and τ_{hp} can be determined based on the required transient estimation

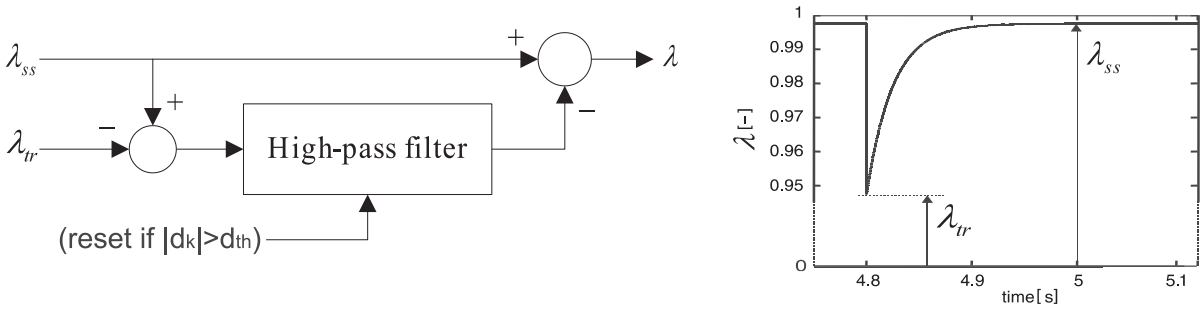

Fig. 4.7 Resetting method to vary the forgetting factor during transient. Left: Block diagram; Right: Variation of λ with τ_{hp} = 0.04 s.

speed. Evaluation of the performance of the algorithm for different choice of the parameters λ_{tr} and τ_{hp} will be made in this section using the example in Section 4.2. In this example, the input signal for the estimation algorithm was the transmitted active power $p(t)$, which consists of an average term (P_0) and a 1 Hz oscillatory components (P_{osc}). The model in (4.9) - (4.11) has been used for the estimation with a variable forgetting factor. The aim of the estimator with variable forgetting factor is to quickly separate these two signal components accurately in the presence of disturbances.

During steady state operations, the bandwidth of the RLS is set to a low value, meaning that the forgetting factor will be close to unity. For an oscillating frequency of 1 Hz, the steady state forgetting factor is set equal to $\lambda = \lambda_{\mathrm{ss}} = 0.9995$, corresponding to a bandwidth of 0.4 Hz for a sampling time T_{s} = 0.2 ms according to (4.13). This gives the performance of the estimator to be selective, less sensitive to noise and at the same time adaptive to slow changes in the input signal. To evaluate the performance of the algorithm for different choice of the parameters λ_{tr} and τ_{hp}, two types of input signals (one noisy free and another one noisy) are considered. For each input, the settling time for the estimator as a function of λ_{tr} and τ_{hp} is shown in Fig. 4.8. With T_{s} = 0.2 ms and λ_{ss} = 0.9995, the transient bandwidth of the estimator, $\alpha_{\mathrm{tr}} = (1-\lambda_{\mathrm{tr}})/T_{\mathrm{s}}$ is varied between 5 Hz and 100 Hz in steps of 5 Hz, while τ_{hp} is varied between 5 ms and 100 ms in steps of 5 ms.

As it can be seen in Fig. 4.8, higher α_{tr} and higher τ_{hp} results in faster response in the case of noise free input signal. when noise is included in the input signal, the estimation speed starts to decrease beyond some values of α_{tr} and higher τ_{hp}. This is due to the estimators tendency to follow the noise, leading to an increase of the settling time. The value that gives a compromised response time for both signals lies in the middle. Depending on the required estimation speed and noise rejection performance, an appropriate value for λ_{tr} and τ_{hp} can be chosen. For this application, a value of $\lambda_{\mathrm{tr}} = 0.8995$ corresponding to $\alpha_{\mathrm{tr}} = 80$ Hz and $\tau_{\mathrm{hp}} = 0.04$ s have been selected.

4.3.2 Frequency adaptation

The RLS algorithm described in Section 4.2.2 uses the information in the observation matrix $\mathbf{\Phi}$ to correctly estimate the signal components. The observation matrix $\mathbf{\Phi}$, which contains informa-

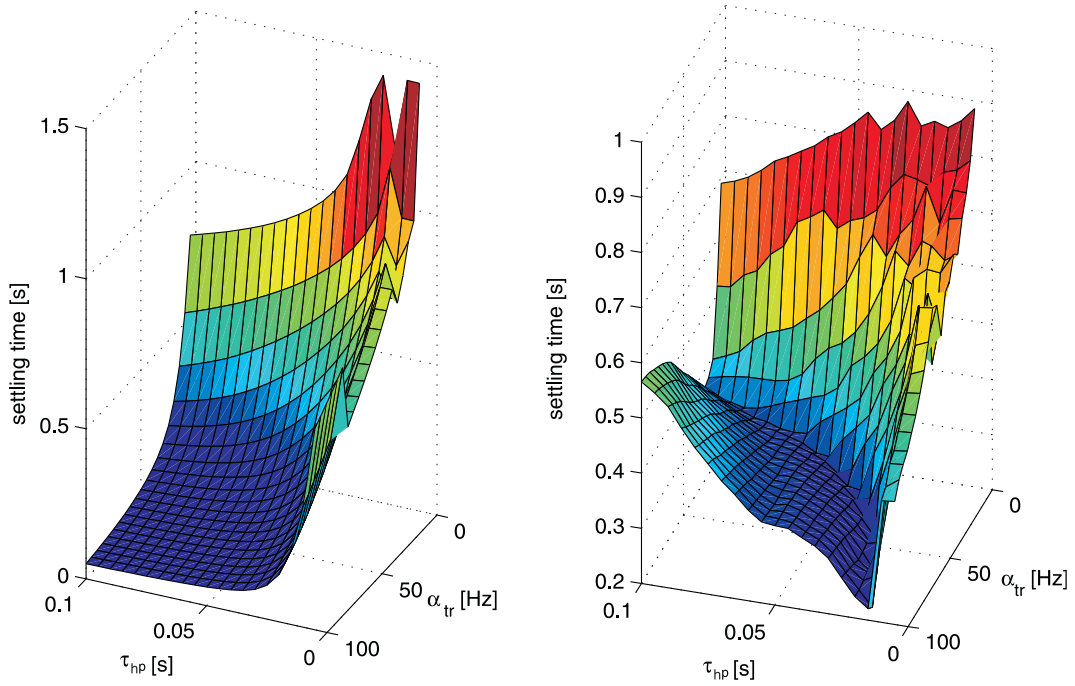

Fig. 4.8 Transient estimation speed for a step change in the input using variable forgetting factor. Left: noise free input; Right: 0.2 pu white noise in the input.

tion about the model of the signal according to (4.8), usually assumes some system parameters [29]. When these parameters change, the performance of the algorithm will be affected and an updating mechanism for the signal model is important. For example, to estimate the oscillatory component P_{osc} from measured input signal p using the RLS algorithm in (4.14) - (4.18), the oscillation frequency ω_{osc} should be known. Any change in the system, which results in a different oscillation frequency, will affect the steady state performance of the RLS algorithm. Therefore, to overcome the problem of oscillation frequency change on estimator's performance, the RLS algorithm is further improved by implementing a frequency adaptation mechanism. Using the same example and parameter selection as in Section 4.3.1, the steady state frequency characteristic of the estimator's transfer function from the input to the average and oscillatory component is shown in Fig. 4.9. The transfer functions have 1 pu gain and 0° phase shift at the estimated frequency component and 0 pu gain at the undesired frequency component. This results in a correct extraction of the average and oscillatory components in steady state for accurate knowledge of the oscillation frequency.

If the frequency content of the input is not accurately known, the estimator will give rise to a phase and amplitude error in the estimated quantities. Using the information in the phase estimate $\tilde{\varphi}$, the true oscillation frequency can be tracked by using a frequency estimator as the one in Fig. 4.10.

The corrective term $\Delta\tilde{\omega}$ is limited and fed back to the RLS algorithm to update the oscillation frequency $\tilde{\omega}_{\text{osc}}$ as

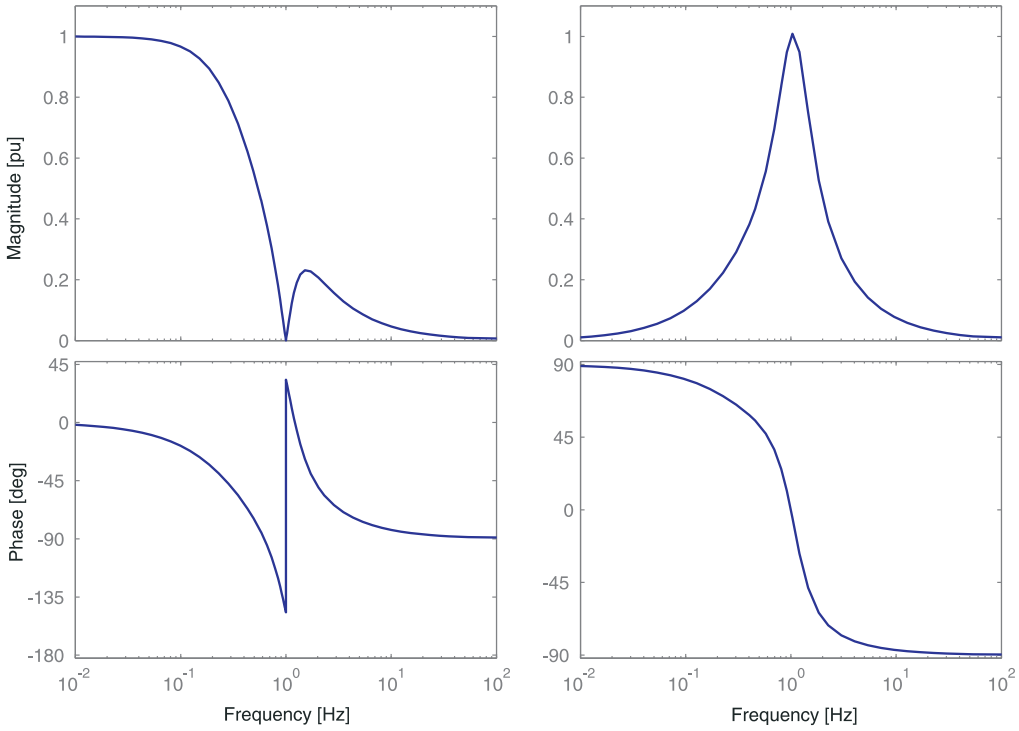

Fig. 4.9 Bode diagram of the steady state RLS based estimator transfer function. Left: from $p(t)$ to $\tilde{P}_0(t)$; Right: from $p(t)$ to $\tilde{P}_{\text{osc}}(t)$.

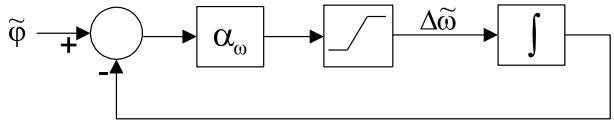

Fig. 4.10 Block diagram for updating the oscillation frequency.

$$\tilde{\omega}_{\text{osc}} = \omega_{\text{osc0}} + \Delta\tilde{\omega} \tag{4.21}$$

The term ω_{osc0} represents the initial assumed oscillation frequency and the transfer function from the estimated phase ($\tilde{\varphi}$) to the estimated change in frequency ($\Delta\tilde{\omega}$) is given by

$$\frac{\Delta\tilde{\omega}}{\tilde{\varphi}} = \frac{\alpha_\omega s}{\alpha_\omega + s} \tag{4.22}$$

If the initial assumed oscillation frequency is correct, the estimated average and phasors $[\tilde{P}_0, \tilde{P}_d, \tilde{P}_q]$ will be constants or slowly varying quantities. Correspondingly, the estimated phase $\tilde{\varphi}$ will be a constant value resulting $\Delta\tilde{\omega} = 0$ in steady state. However, if a change in the true oscillation frequency $\Delta\omega$ occurs, the estimates $[\tilde{P}_0, \tilde{P}_d, \tilde{P}_q]$ will contain a disturbance term at the true oscillatory frequency in addition to a slowly varying quantity. This is due to the fact that the estimator's transfer function can not have zero gain at the true oscillation frequency for the estimates ($[\tilde{P}_0, \tilde{P}_d, \tilde{P}_q]$) due to wrong assumption of the initial oscillation frequency. Similarly, the

estimate $\tilde{P}_{\text{osc}}$ will have an amplitude and phase error as the estimator's transfer function cannot have a 1 pu gain and 0° phase at the true oscillation frequency. If A_ω and φ_ω represent the gain and phase of the estimator's transfer function at the true oscillation frequency respectively, the oscillatory estimate in steady state can be expressed as

$$\tilde{P}_{osc}(t) = A_\omega P_{\text{ph}} \cos(\omega_{osc} t + \varphi_\omega) = \tilde{P}_{\text{ph}}(t) \cos(\omega_{osc0} t + \tilde{\varphi}(t)) \tag{4.23}$$

The terms P_{ph} and ω_{osc} represent the true amplitude and frequency of the oscillatory component, respectively. As can be seen in (4.23), the frequency of the oscillation is preserved in the estimate. The idea here is to estimate the corrective term $\Delta\tilde{\omega}$ from the estimated phasors ($\tilde{P}_d, \tilde{P}_{\text{q}}$). From (4.23) and using the definition in (4.18) - (4.19), the phase estimate $\tilde{\varphi}$ can be expressed as

$$\tilde{\varphi}(t) = \tan^{-1}\left[\frac{\tilde{P}_q(t)}{\tilde{P}_d(t)}\right] \approx (\Delta\omega + d_\omega)t \tag{4.24}$$

Due to wrong assumption of the initial oscillation frequency, the estimates ($\tilde{P}_d, \tilde{P}_q$) will contain a disturbance term at the true oscillation frequency. This in turn results a disturbance d_ω in the phase estimate $\varphi(t)$ at twice the true oscillation frequency. As can be seen from (4.24), the phase estimate is a function the frequency error $\Delta\omega$ and this has to be extracted. If the disturbance term d_ω is neglected, the transfer function from the actual frequency error $\Delta\omega$ to the estimated frequency error $\Delta\tilde{\omega}$ can be expressed as

$$\frac{\Delta\tilde{\omega}}{\Delta\omega} \approx \frac{\alpha_\omega}{s + \alpha_\omega} \tag{4.25}$$

Using (4.25), the bandwidth of the frequency controller can be chosen. To be able to filter the disturbance term, the bandwidth should be set below the oscillation frequency. For an assumed oscillation frequency ω_{osc0}, choosing $\alpha_\omega = 0.2\omega_{\text{osc0}}$ gives the frequency correction controller a cut-off frequency a decade below the frequency of the disturbance term d_ω.

4.4 Application examples on signal estimation

In this section, application examples for signal estimation using the improved RLS based method will be described.

4.4.1 Estimation of low-frequency electromechanical oscillations

To evaluate the performance of the improved RLS based method for estimation of low-frequency electromechanical oscillations, an input signal that contains an average component and a single oscillation frequency of 1 Hz as in Fig. 4.11 is assumed. Figure 4.12 shows the estimated average and oscillatory component of the input signal (in amplitude and phase) when a step is applied to the input at 3.0 s for different choice of the forgetting factor λ with the conventional

RLS algorithm. In this simulation, three λ values that correspond to a steady state bandwidth of 0.4 Hz (black solid), 1.0 Hz (gray solid) and 2.0 Hz (black dashed) are considered.

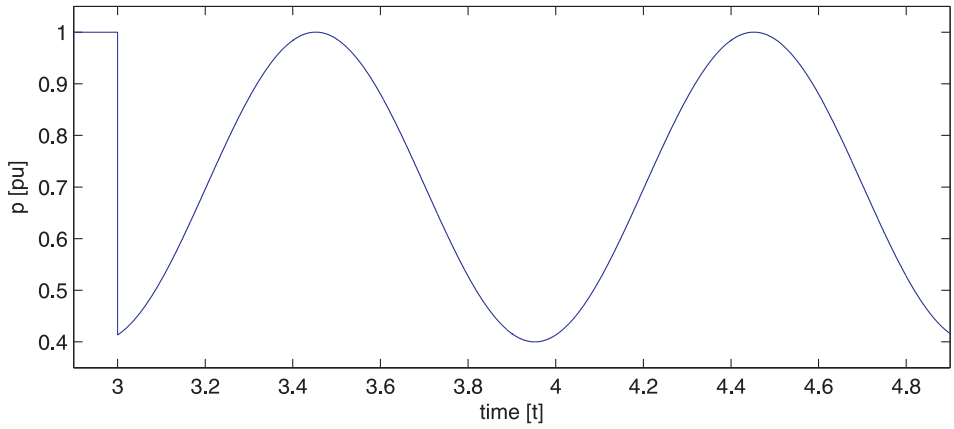

Fig. 4.11 Input signal for simulation.

As the results in Fig. 4.12 show, by using the conventional RLS with a fixed forgetting factor, it is not possible to achieve both estimation speed and frequency selectivity. As the forgetting factor is reduced, estimation speed will be improved whereasthe selectivity is reduced and vise versa. This can be improved by using a variable forgetting factor as described in Section 4.3.1. Figure 4.13 shows the the performance of the improved RLS method with the estimator parameters chosen as ($\lambda_{\text{ss}} = 0.9995, \lambda_{\text{tr}} = 0.8995$ and $\tau_{\text{hp}} = 0.04$ s for T_{s} = 0.2 ms). As can be seen from the results in Fig. 4.12 - 4.13, the improved RLS based method gives a fast estimation with a better frequency selectivity than the conventional RLS (See Fig. 4.12).

The simulation is repeated with the addition of a 0.05 pu white noise in the input signal in Fig. 4.11 and a 30$\%$ error in assumed oscillation frequency. Figure 4.14 shows the estimated average and oscillatory component when the proposed method is used for estimation. The frequency adaptive structure for the RLS estimater as described in the previous section is used and Figure 4.15 (bottom) shows the estimate of the oscillation frequency.

The initial oscillations in the estimates are due to the low forgetting factor during the transient period for faster estimation which makes the estimator to follow the noise. These oscillations quickly decay as the forgetting factor is controlled to the steady state value. The value of α_{tr} and τ_{hp} as described previously is a trade off between selectivity (rejection of unwanted frequency component, eg. noise) and speed of estimation. The overall reduction in the speed of estimation compared with the ideal case in Fig. 4.13 is due to the error introduced in the assumed oscillation frequency. The frequency correction controller tracks the true oscillation frequency with a bandwidth defined in previous section and the phase and amplitude errors in the estimates will be reduced. Without the frequency adaptation, the steady state error in the estimates is shown clearly in Fig. 4.14 (dashed curves).

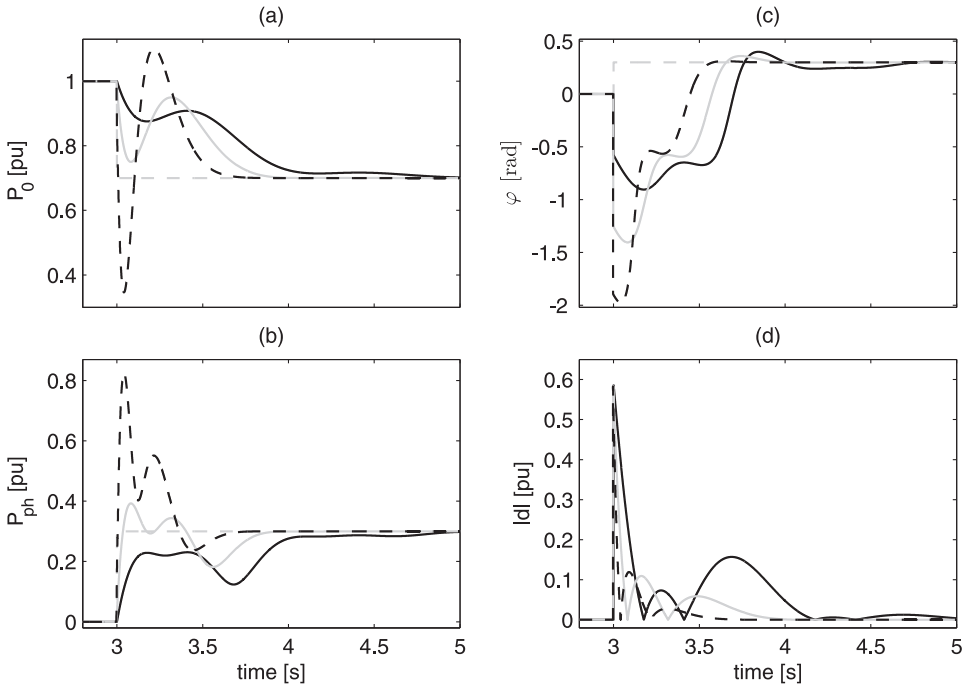

Fig. 4.12 Estimate for the average (plot a), amplitude (plot b), phase (plot c) and estimation error (plot d) by conventional RLS with forgetting factor λ = 0.9995(black solid), λ = 0.9987(gray solid), λ = 0.9975 (black dashed), input signals(gray dashed); the actual oscillation frequency is used in the simulation.

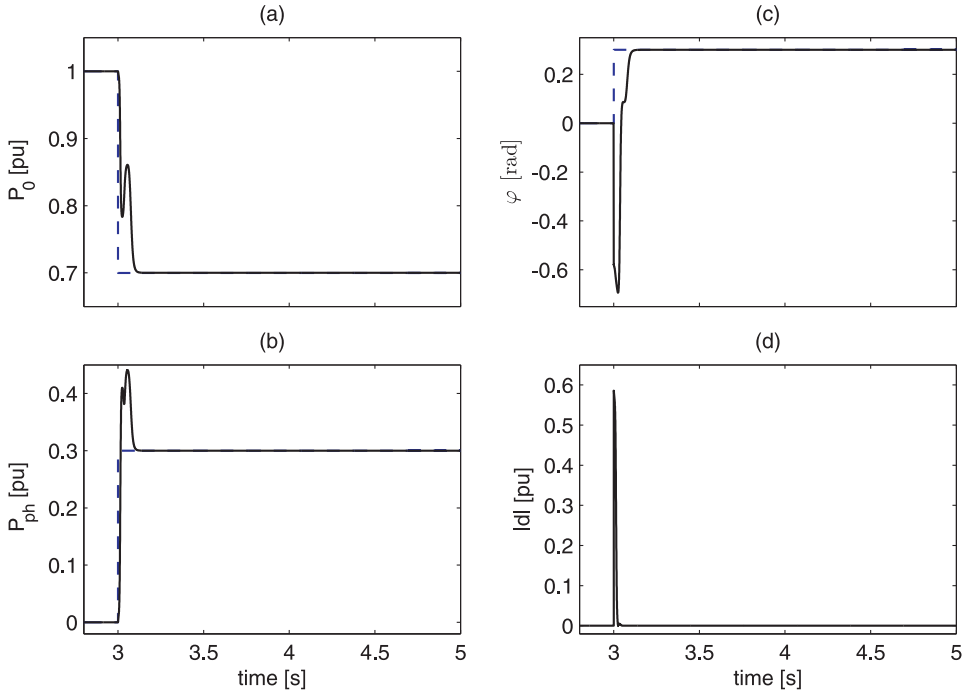

Fig. 4.13 Estimate for the average (plot a), amplitude (plot b), phase (plot c) and estimation error (plot d) using the improved RLS method; dashed: inputs, solid: estimates; the actual oscillation frequency is used in the simulation.

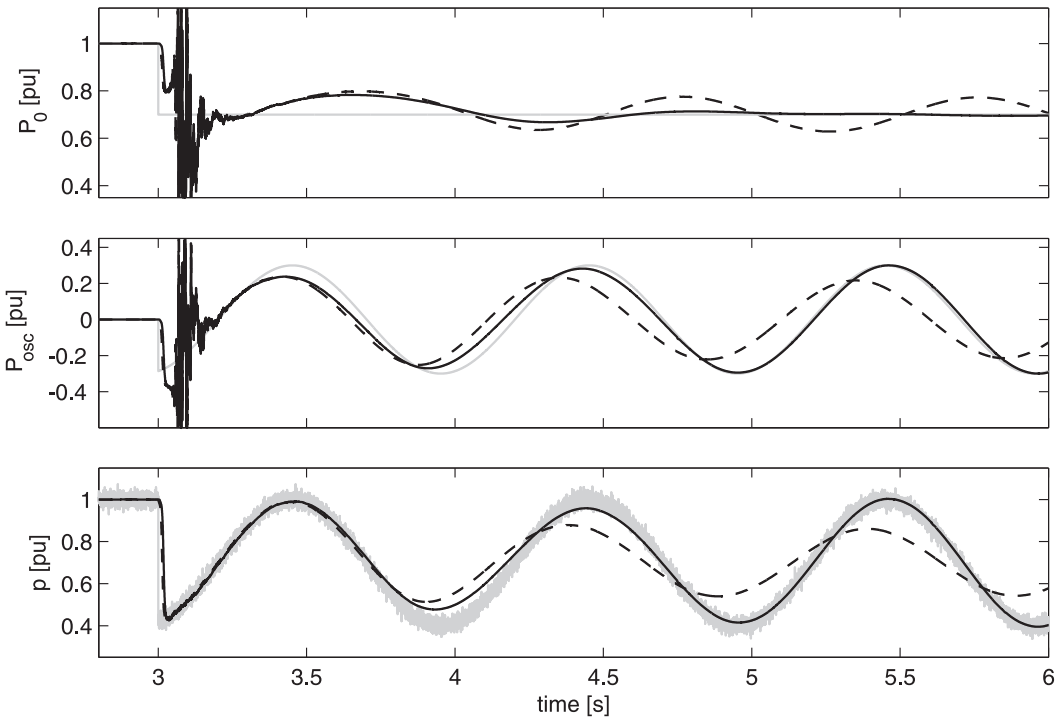

Fig. 4.14 Estimate for the average and oscillatory component in the presence of 0.05 pu white noise in the input and a 30% error in assumed oscillation frequency. Average component (top), oscillatory component (middle) and total signal (bottom); actual signal (solid gray), estimate with frequency update (solid black) and estimates with no frequency update (dashed black);

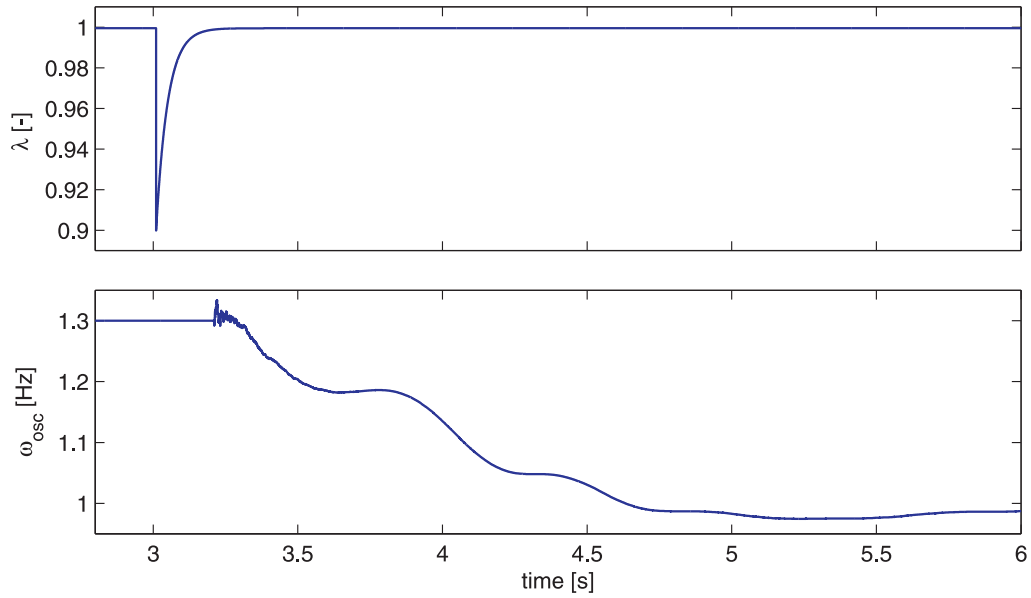

Fig. 4.15 Improved RLS based estimator; Variation of forgetting factor λ (top) and estimate of oscillation frequency $\tilde{\omega}_{\text{osc}}$ (bottom);

4.4.2 Estimation of sequence and harmonic components

In this section, estimation of harmonic and sequence components in three phase system using the improved RLS based algorithm will be described. When the grid voltage is unbalanced due to unbalanced loads or unbalanced faults, a 50 Hz negative sequence component exists in the grid voltage and a fast estimation algorithm is needed to separate the negative sequence component for control or synchronization purposes [33][34][35]. Assuming that the zero sequence component in the measured signal can be neglected, the complex grid voltage $\underline{e}_{\mathrm{g}}^{\alpha\beta}$ in the stationary $\alpha\beta$ coordinate system can be written as the sum of its positive and negative sequence components as [29][36]

$$\underline{e}_{\mathrm{g}}^{\alpha\beta}(t) = \underline{E}_{\mathrm{p}}(t)e^{j\theta_{\mathrm{g}}(t)} + \underline{E}_{\mathrm{n}}(t)e^{-j\theta_{\mathrm{g}}(t)} \tag{4.26}$$

Calling the grid frequency ω_{g} with $\theta_{\mathrm{g}}(t) = \omega_{\mathrm{g}}t$, $\underline{E}_{\mathrm{p}}$ and $\underline{E}_{\mathrm{n}}$ are the positive and negative sequence component phasors, respectively. Therefore, the model in (4.27) can be used to set up an RLS algorithm as described in Section 4.2.2 (including the modifications in Section 4.3) to estimate the positive and negative sequence components. For this particular case, the state vector to be estimated and the observation matrix are given as in (4.28) - (4.29) and the updates are performed recursively as in (4.9) - (4.11).

$$\underline{e}_{\mathrm{g}}^{\alpha\beta}(k) = \underline{\tilde{E}}_{\mathrm{p}}(k)e^{j\tilde{\theta}_{\mathrm{g}}(k)} + \underline{\tilde{E}}_{\mathrm{n}}(k)e^{-j\tilde{\theta}_{\mathrm{g}}(k)} + \underline{d}(k) = \mathbf{\Phi}(k)\tilde{\mathbf{h}}(k-1) + \underline{d}(k) \tag{4.27}$$

$$\tilde{\mathbf{h}}(k) = \begin{bmatrix} \underline{\tilde{E}}_{\mathrm{p}}(k) & \underline{\tilde{E}}_{\mathrm{n}}(k) \end{bmatrix}^{\mathrm{T}} \tag{4.28}$$

$$\mathbf{\Phi}(k) = \begin{bmatrix} e^{j\tilde{\theta}_{\mathrm{g}}(k)} & e^{-j\tilde{\theta}_{\mathrm{g}}(k)} \end{bmatrix} \tag{4.29}$$

For a constant grid frequency, the estimator's steady state frequency response is shown in Fig. 4.16 (left) for the positive sequence component, where a gain of 1 pu and a phase of 0° is achieved at the estimated frequency component ω_{g}. Similarly, for negative sequence component a gain of 1 pu and a phase of 0° is achieved at the desired frequency $-\omega_{\mathrm{g}}$. A typical example where the sequence estimation can be used is in a phase locked loop (PLL). The PLL estimates the phase of the positive sequence grid voltage θ_{g} [35][37]. The block diagram for this application is shown in Fig. 4.16 (plot b) where the frequency output of the PLL can be fed back to the sequence estimator to make the sequence estimator frequency adaptive.

Consider now the case of a distorted gird voltage. Each harmonic component appears at a frequency $n\omega_{\mathrm{g}}$ where n represents the harmonic order, and its sign depends on whether the harmonic is a positive or negative sequence component. In general, the model of the grid voltage $\underline{e}_{\mathrm{g}}^{\alpha\beta}$ is given by [36]

$$\underline{e}_{\mathrm{g}}^{\alpha\beta}(t) = \underline{E}_{1}(t)e^{j\theta_{\mathrm{g}}(t)} + \sum_{i=1}^{N} \underline{E}_{n_i}(t)e^{jn_i\theta_{\mathrm{g}}(t)} \tag{4.30}$$

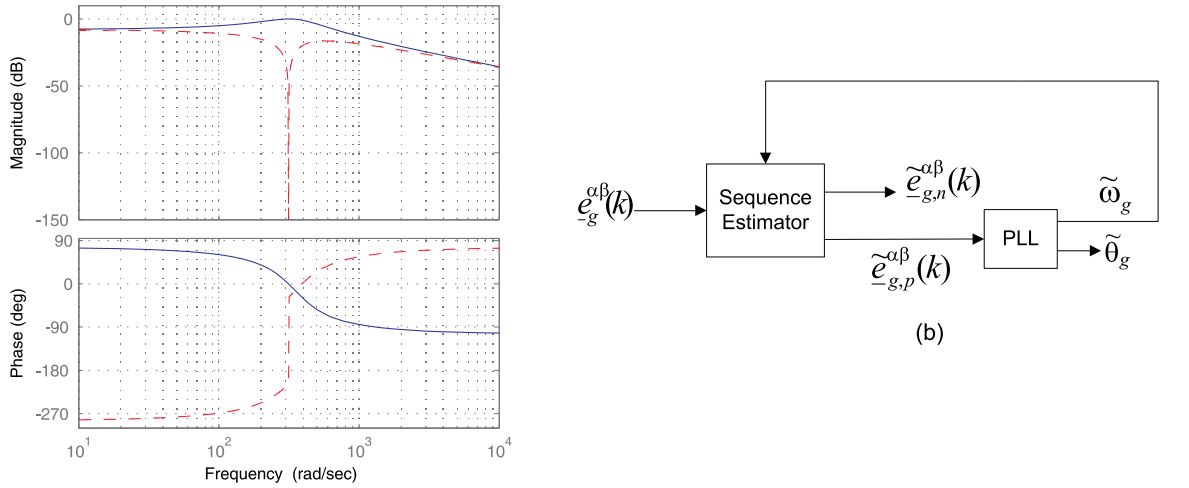

Fig. 4.16 Sequence estimation (a) Bode diagram for positive sequence component estimation; response for the positive frequency (solid), response for the negative frequency (dashed); (b) Block diagram of RLS-based sequence estimator with a PLL for synchronization and frequency adaptation of the sequence estimator.

where $\underline{E}_{n_i}$ represents the $n_{\mathrm{i}}^{\mathrm{th}}$ harmonic phasor and $\underline{E}_1$ is the fundamental frequency phasor. The RLS algorithm as described in Section 4.2.2 can be set up from the model in (4.31) where the state vector and observation matrix are given by (4.32) - (4.33).

$$\underline{e}_{\mathrm{g}}^{\alpha\beta}(k) = \underline{\tilde{E}}_1(k)e^{j\tilde{\theta}_{\mathrm{g}}(k)} + \sum_{i=1}^{N} \underline{\tilde{E}}_{n_i}(k)e^{jn_i\tilde{\theta}_{\mathrm{g}}(k)} + \underline{d}(k) = \mathbf{\Phi}(k)\mathbf{h}(k-1) + \underline{d}(k) \tag{4.31}$$

$$\tilde{\mathbf{h}}(k) = [\ \underline{\tilde{E}}_1(k) \quad \underline{\tilde{E}}_{n_1}(k) \quad \ldots \quad \underline{\tilde{E}}_{n_N}(k)\ ]^{\mathrm{T}} \tag{4.32}$$

$$\mathbf{\Phi}(k) = [\ \ e^{j\tilde{\theta}_{\mathrm{g}}(k)} \quad e^{jn_1\tilde{\theta}_{\mathrm{g}}(k)} \quad \ldots \quad e^{jn_N\tilde{\theta}_{\mathrm{g}}(k)}\ ] \tag{4.33}$$

For balanced three phase system, each harmonic component will appear as either positive or negative sequence component in (4.30). For unbalanced case, both positive and negative sequence component could exist for each harmonic order (including harmonic orders at multiple of three) and the model in (4.30) should account for that [36]. When needed, the dc component which is typically present in the measured signals can also be estimated by including a zero-frequency component in the model.

As the same grid angle is used in both the sequence and harmonic estimation algorithms, the PLL structure used in Fig. 4.16 (right) can be used to realize a frequency adaptive estimator. The model in (4.26) - (4.29) can be obtained from (4.30) - (4.33) by setting n_i to -1 and 0 for $i = 1$ and $i \neq 1$, respectively. To find the parameters of the estimator, the frequency content of the input signal and the required estimation speed should be considered. For this particular application, with a sampling time $T_s = 0.2$ ms, the steady state forgetting factor $\lambda_{\mathrm{ss}} = 0.9686$

corresponding to a bandwidth of 25 Hz is chosen. For fast transient performance, the transient forgetting factor $\lambda_{\text{tr}} = 0.6859$ corresponding to $\alpha_{\text{tr}} = 250$ Hz and $\tau_{\text{hp}} = 0.01$ s have been selected.

To evaluate the performance of the improved RLS based method for estimation of sequence components, an unbalanced fault with a phase jump is applied to a three phase grid voltage and the estimator's performance is shown in Fig. 4.17. As the results indicate, the sequence components are estimated very quickly following the fault which verifies the validity of the estimator. The simulation is repeated to estimate harmonic components. In this case, a step in harmonic content (5^{th} and 7^{th} order harmonics) of a three phase voltage is applied and the estimators performance is shown in Fig. 4.18.

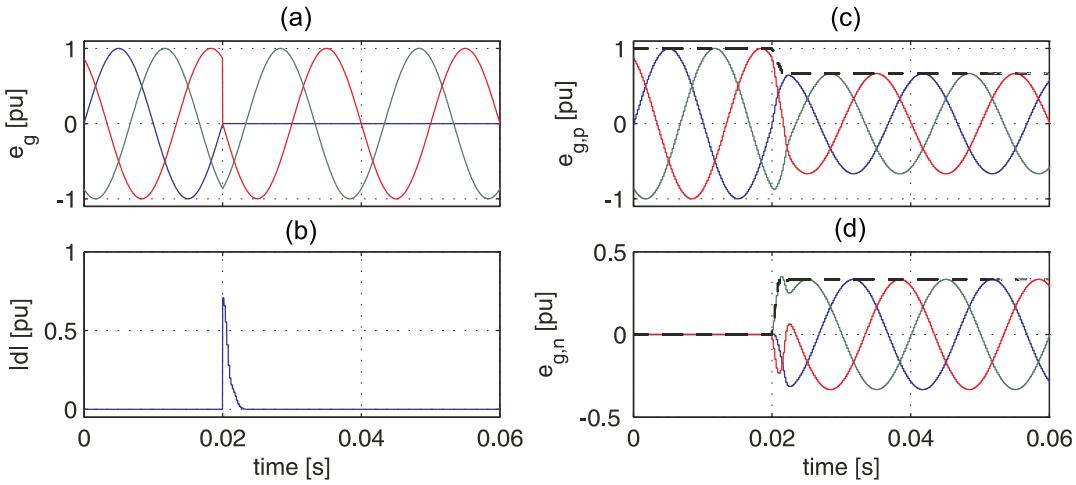

Fig. 4.17 Sequence estimation for unbalanced fault with phase jump; (a) grid voltage, (b) estimation error, (c) positive sequence component and (d) negative sequence component. Dashed: Magnitude of sequence component phasor.

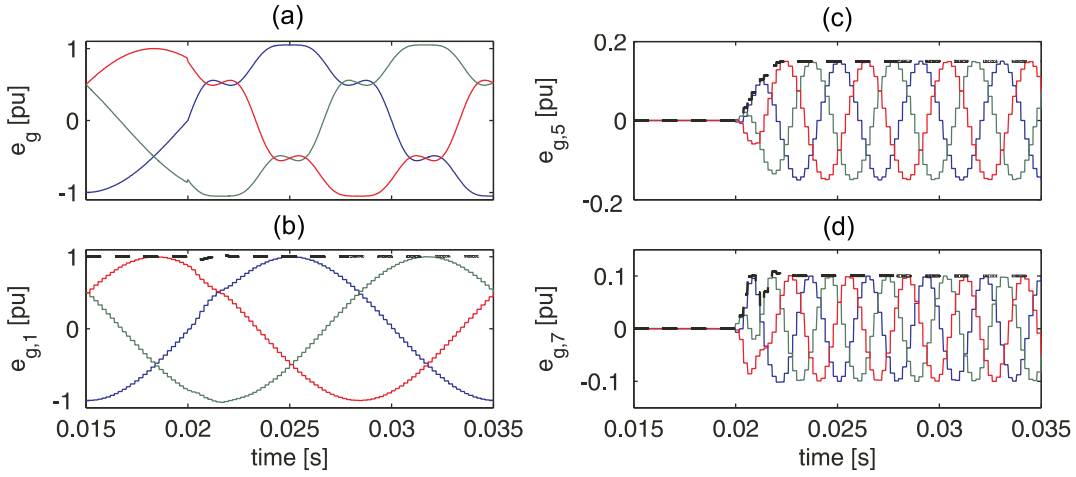

Fig. 4.18 Harmonic estimation in distorted three phase voltage; (a) grid voltage, (b) fundamental component, (c) 5^{th} order harmonic component and (d) 7^{th} order harmonic component. Dashed: Magnitude of harmonic component phasor.

The fast estimation of the sequence or harmonic harmonic components can be used to achieve a fast control of these components such as in active filter applications [29].

4.5 Conclusions

In this chapter, an estimation algorithm based on improved RLS algorithm has been described in detail. First, a LPF based estimation algorithm has been described and compared with a conventional RLS based estimator. The problem of the LPF based method when high speed of response is required has been highlighted. To obtain a fast estimator with good frequency selectivity, the RLS algorithm has been modified using variable forgetting factor and frequency adaptation. With this method, a fast and selective estimation performance of the algorithm has been obtained. The application of the algorithm has been shown for estimation of low-frequency electromechanical oscillations and estimation of harmonic and sequence components. The results in this chapter will be applied for controller design in the coming chapters. Estimation of harmonics and sequence components will be used to design a current controller in distorted grids in Chapter 5 whereas the estimation of low-frequency power oscillations will be used for design of a POD controller in Chapter 6.

Chapter 5

Control of shunt-connected E-STATCOM

5.1 Introduction

In this section, the control of E-STATCOM connected to a three-phase grid will be described. First, the inner current controller loop will be derived. Improvements to the controller to deal with disturbances from harmonic and unbalanced grid conditions will be discussed. The performance of the inner current controller loop will be verified through simulation. The different outer controller loops will also be described.

5.2 System layout

The main circuit scheme of a two-level Voltage Source Converter (VSC) with energy storage connected to a grid through an L-filter having inductance L_{f} and resistance R_{f} is shown in Fig. 5.1. The grid is represented by its Thevenin equivalent with voltages at the connection point $e_{\mathrm{ga}}(t)$, $e_{\mathrm{gb}}(t)$ and $e_{\mathrm{gc}}(t)$. The grid inductance and resistance are denoted by L_{g} and L_{g}, respectively. The VSC injects three-phase currents denoted by $i_{\mathrm{fa}}(t)$, $i_{\mathrm{fb}}(t)$, $i_{\mathrm{fc}}(t)$ to the grid.

The valves in the phase-legs of the VSC (usually insulated gate bipolar transistors, IGBTs) are controlled by the switching signals $sw_{\mathrm{a}}(t)$, $sw_{\mathrm{b}}(t)$ and $sw_{\mathrm{c}}(t)$. The DC-link voltage is denoted by $u_{\mathrm{dc}}(t)$. When $sw_{\mathrm{a}}(t)$ is equal to 1, the upper valve in the phase a is turned on while the lower valve in the same leg is off. Therefore, the potential $u_{\mathrm{ca}}(t)$ is equal to half of the DC-link voltage, $u_{\mathrm{dc}}(t)/2$. Similarly, when the switching signal is equal to -1, the upper valve is off and the lower one is on and, thus, $u_{\mathrm{ca}}(t)$ is equal to $-u_{\mathrm{dc}}(t)/2$. To obtain the switching signals for the VSC, Pulse Width Modulation technique (PWM) has been adopted [38].

An energy storage is connected on the DC side of the converter. This gives the VSC the capability of injecting active power.

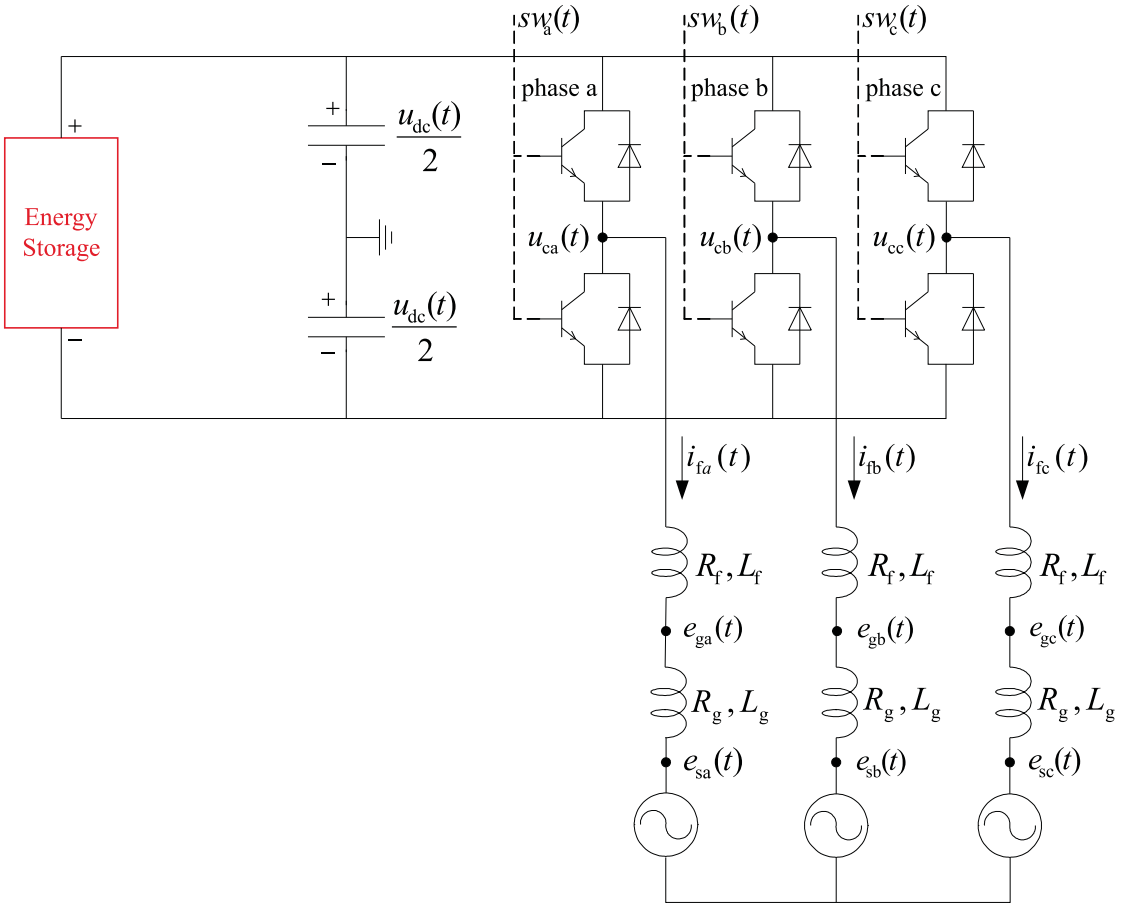

Fig. 5.1 Main circuit of three-phase two-level E-STATCOM connected to the grid.

The different control blocks for the VSC system are shown in Fig.5.2. The control system consists of an inner current controller loop and different outer controller loops which include the AC voltage controller, the DC voltage controller, the POD and TSE controllers. A Phase-Locked Loop (PLL) is used to track the grid voltage angle θ_g for coordinate the transformation. See Appendix A for the adopted transformation from three-phase to $\alpha\beta$ and $\alpha\beta$ to dq reference-frames and vise versa.

Outputs from the control system are the PWM signals sw_a, sw_b and sw_c. To generate these signals, the following will be performed.

1. Various signals such as the grid voltages, filter currents, DC-link voltage and active power flow in the transmission system P_g are measured and sampled at a rate $1/T_s$ where T_s is the sampling time.

2. After coordinate transformation, the reference currents input to the current controller are calculated in the different outer control blocks. The converter voltage reference, which is the output of the current controller, will then be converted from the rotating dq-coordinate system to the stationary $\alpha\beta$-coordinate using transformation angle $\theta_g(k) + \Delta\theta$, where $\Delta\theta = 1.5\omega T_s$ is a compensation angle to take into account the half sample delay intro-

duced by the discretization of the measured quantities and one sample delay introduced by the computation time delay [39].

3. From the three-phase converter voltage references (u^*_{ca}, u^*_{cb}, u^*_{cc}), the duty-cycles are calculated in the PWM block and the switching pulses are sent to the VSC valves.

The algorithm for the different control blocks will be described in detail in the following sections.

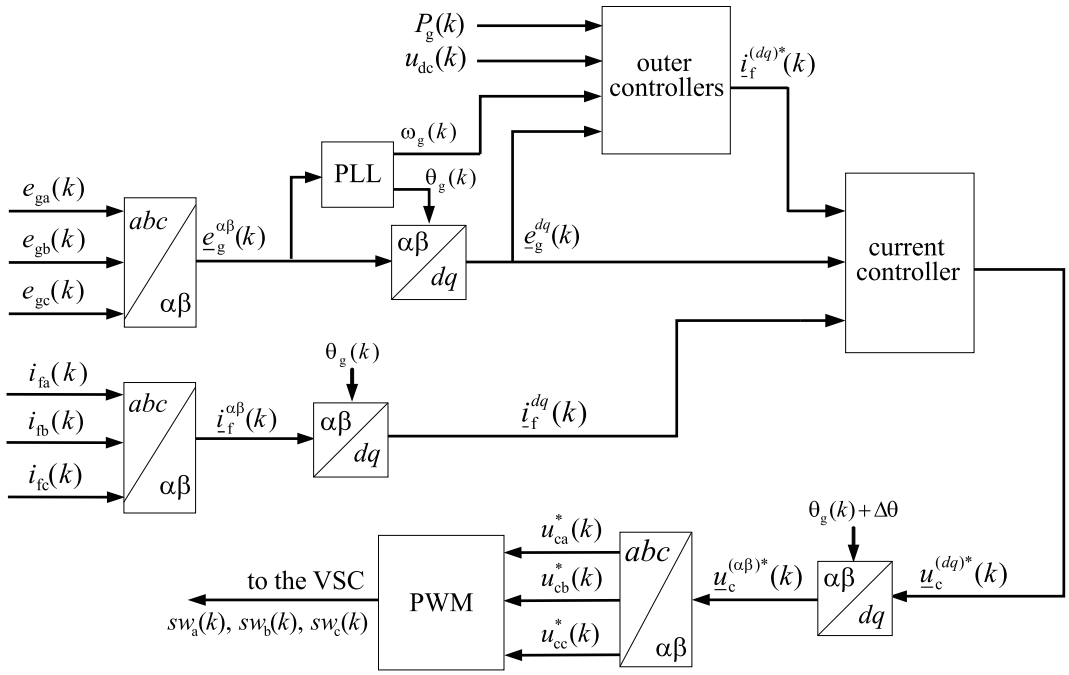

Fig. 5.2 Overall block diagram of the control system of an E-STATCOM.

5.3 Inner current controller loop

A number of control strategies for grid-connected Voltage Source Converter (VSC) are available in the literature [40][41][42][43]. Among the different methods, a synchronous-frame Proportional-Integral (PI) current control, designed using the internal model control approach, has the advantage of simple implementation and robust performance in ideal-grid conditions [44]. This method is used in this work to design the current controller for the E-STATCOM.

5.3.1 Basic current controller

For a VSC connected to a grid with voltage e_g at connection point though a filter with inductance L_f and resistance R_f as in Fig. 5.3, the filter current i_f dynamics are expressed in the stationary $\alpha\beta$ reference-frame as in (5.1) where u_c is the converter output voltage.

$$L_{\mathrm{f}}\frac{d}{dt}\underline{i}_{\mathrm{f}}^{\alpha\beta}(t) = \underline{u}_{\mathrm{c}}^{\alpha\beta}(t) - \underline{e}_{\mathrm{g}}^{\alpha\beta}(t) - R_{\mathrm{f}}\underline{i}_{\mathrm{f}}^{\alpha\beta}(t) \tag{5.1}$$

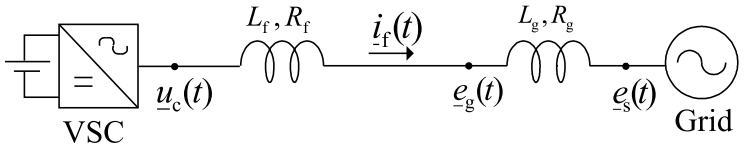

Fig. 5.3 Single line diagram of a VSC connected to a grid through a filter.

By using a PLL which tracks the grid voltage angle θ_{g} [37], the expression in (5.1) can be rewritten in the synchronous dq reference-frame as in (5.2). Assuming ideal waveforms, the dq quantities are constant in steady state. For all signals, the dq and $\alpha\beta$ reference-frames are related according to (5.3) where $\omega_{\mathrm{g}} = d\theta_{\mathrm{g}}(t)/dt$ represents the fundamental grid frequency.

$$L_{\mathrm{f}}\frac{d}{dt}\underline{i}_{\mathrm{f}}^{dq}(t) = \underline{u}_{\mathrm{c}}^{dq}(t) - \underline{e}_{\mathrm{g}}^{dq}(t) - j\omega_{\mathrm{g}}L_{\mathrm{f}}\underline{i}_{\mathrm{f}}^{dq}(t) - R_{\mathrm{f}}\underline{i}_{\mathrm{f}}^{dq}(t) \tag{5.2}$$

$$\underline{e}_{\mathrm{g}}^{dq}(t) = \underline{e}_{\mathrm{g}}^{\alpha\beta}(t)e^{-j\theta_{\mathrm{g}}(t)} \tag{5.3}$$

If the PLL is synchronized with the grid voltage vector, the d and q component of the current represents the active and reactive currents injected to the grid, respectively. The purpose of the current controller is to independently control these currents. For the dynamical model in (5.2), using internal model control approach [43][44], the PI current controller in continuous time is given by (5.4) where γ_{cc} represents the desired closed loop bandwidth of the current controller. Using the estimate of the filter inductance and resistance, the proportional and integral gains of the PI controller are given by $\gamma_{\mathrm{cc}}\hat{L}_{\mathrm{f}}$ and $\gamma_{\mathrm{cc}}\hat{R}_{\mathrm{f}}$, respectively. The cross-coupling between the d and q filter currents is easily compensated in steady state. A feed-forward of the grid voltage is also included for a good dynamic performance of the controller. In the notations, the superscript "*" denotes a reference signal.

$$\begin{aligned}\underline{u}_{\mathrm{c}}^{dq*}(t) = \underline{e}_{\mathrm{g}}^{dq}(t) + j\hat{\omega}_{\mathrm{g}}\hat{L}_{\mathrm{f}}\underline{i}_{\mathrm{f}}^{dq}(t) + \gamma_{\mathrm{cc}}\hat{L}_{\mathrm{f}}\left(\underline{i}_{\mathrm{f}}^{dq*}(t) - \underline{i}_{\mathrm{f}}^{dq}(t)\right) \quad + \\ \gamma_{\mathrm{cc}}\hat{R}_{\mathrm{f}}\int_0^t\left(\underline{i}_{\mathrm{f}}^{dq*}(\tau) - \underline{i}_{\mathrm{f}}^{dq}(\tau)\right)d\tau\end{aligned} \tag{5.4}$$

In ideal grid conditions and assuming perfect cancellation of the cross-coupling term, the closed-loop transfer function from reference to actual signal results in a first order low-pass filter with cut-off frequency γ_{cc} as

$$\begin{bmatrix} \underline{i}_{\mathrm{f}}^{d}(s) \\ \underline{i}_{\mathrm{f}}^{q}(s) \end{bmatrix} = \begin{bmatrix} \frac{\gamma_{\mathrm{cc}}}{s+\gamma_{\mathrm{cc}}} & 0 \\ 0 & \frac{\gamma_{\mathrm{cc}}}{s+\gamma_{\mathrm{cc}}} \end{bmatrix} \begin{bmatrix} \underline{i}_{\mathrm{f}}^{d*}(s) \\ \underline{i}_{\mathrm{f}}^{q*}(s) \end{bmatrix} \tag{5.5}$$

Although effective to derive the controller parameters, the desired closed-loop transfer function in (5.5) is difficult to obtain in an actual system due to inaccurate knowledge of filter parameters and the unavoidable non-linearities such as time delays and converter voltage saturation

[39]. In particular, delays due to discretization and computational time have a major impact on the system dynamic performance, especially in case of connection to distorted grid. For real time implementation, the controller in (5.4) is expressed in discrete time using Euler's forward approximation as

$$\begin{aligned}\underline{u}_{\mathrm{c}}^{dq*}(k) = \underline{e}_{\mathrm{g}}^{dq}(k) + j\hat{\omega}_{\mathrm{g}}\hat{L}_{\mathrm{f}}\underline{i}_{\mathrm{f}}^{dq}(k) + \gamma_{\mathrm{cc}}\hat{L}_{\mathrm{f}}\left(\underline{i}_{\mathrm{f}}^{dq*}(k) - \underline{i}_{\mathrm{f}}^{dq}(k)\right) \quad + \\ \gamma_{\mathrm{cc}}\hat{R}_{\mathrm{f}}T_{\mathrm{s}}\sum_{n=0}^{k}\left(\underline{i}_{\mathrm{f}}^{dq*}(n) - \underline{i}_{\mathrm{f}}^{dq}(n)\right)\end{aligned} \tag{5.6}$$

To deal with system parameter variations and disturbances, active damping can be included to the controller in (5.6) [43]. This involves calculating the controller parameters assuming a fictitious resistance (or active damping term, R_{a}) in the system. This will impact the value of the total system resistance which is equal to $R_{\mathrm{f}} + R_{\mathrm{a}}$. The effect of additional resistance R_{a} will then be compensated in the feed-forward term as

$$\begin{aligned}\underline{u}_{\mathrm{c}}^{dq*}(k) = \underline{e}_{\mathrm{g}}^{dq}(k) + \left(j\hat{\omega}_{\mathrm{g}}\hat{L}_{\mathrm{f}} - R_{\mathrm{a}}\right)\underline{i}_{\mathrm{f}}^{dq}(k) + \gamma_{\mathrm{cc}}\hat{L}_{\mathrm{f}}\left(\underline{i}_{\mathrm{f}}^{dq*}(k) - \underline{i}_{\mathrm{f}}^{dq}(k)\right) \quad + \\ \gamma_{\mathrm{cc}}\left(\hat{R}_{\mathrm{f}} + R_{\mathrm{a}}\right)T_{\mathrm{s}}\sum_{n=0}^{k}\left(\underline{i}_{\mathrm{f}}^{dq*}(n) - \underline{i}_{\mathrm{f}}^{dq}(n)\right)\end{aligned} \tag{5.7}$$

The value of the active damping term should be selected carefully. Even if a higher value would provide larger damping to system disturbances, the increase of the integral gain might lead to instabilities when used in discrete controllers with non negligible delays. Guidelines on the selection of the active damping term is given in [43].

The magnitude of the reference voltage for the converter should be limited based on the available DC-link voltage magnitude. When the magnitude of calculated reference voltage in (5.7) $|\underline{u}_{\mathrm{c}}^{dq*}|$ is higher than the maximum converter voltage ($U_{\mathrm{c,max}}$), the converter can not provide the required reference voltage. When this happens, the integrator in the controller will not be able to force the error to zero and this leads to integration windup. To avoid this, the integral action should be stopped during saturation or an anti-windup function should be added [26][44]. In this work, back calculation of the error input of the integral term is used. When back calculation is used, the control system law is modified as

$$\begin{aligned}\underline{u}_{\mathrm{c}}^{dq*}(k) = \underline{e}_{\mathrm{g}}^{dq}(k) + \left(j\hat{\omega}_{\mathrm{g}}\hat{L}_{\mathrm{f}} - R_{\mathrm{a}}\right)\underline{i}_{\mathrm{f}}^{dq}(k) + \gamma_{\mathrm{cc}}\hat{L}_{\mathrm{f}}\left(\underline{i}_{\mathrm{f}}^{dq*}(k) - \underline{i}_{\mathrm{f}}^{dq}(k)\right) \quad + \\ \gamma_{\mathrm{cc}}\left(\hat{R}_{\mathrm{f}} + R_{\mathrm{a}}\right)T_{\mathrm{s}}\sum_{n=0}^{k}\left(\underline{i}_{\mathrm{f}}^{dq*}(n) - \underline{i}_{\mathrm{f}}^{dq}(n) + \underline{i}_{\mathrm{err}(n)}^{dq}\right)\end{aligned} \tag{5.8}$$

with the additional error to the integral input $\underline{i}_{\mathrm{err}}^{dq}$ given by

$$\underline{i}_{\mathrm{err}}^{dq}(k) = \frac{1}{\gamma_{\mathrm{cc}}\hat{L}_{\mathrm{f}}}\left(\underline{u}_{\mathrm{c}}^{dq*}(k) - \underline{u}_{\mathrm{c,lim}}^{dq*}(k)\right) \tag{5.9}$$

Observe that here only the magnitude of the reference voltage is limited to $U_{\mathrm{c,max}}$ as

$$\underline{u}_{\mathrm{c,lim}}^{dq*}(k) = \frac{\underline{u}_{\mathrm{c}}^{dq*}(k)}{|\underline{u}_{\mathrm{c}}^{dq*}(k)|} \min\left\{|\underline{u}_{\mathrm{c}}^{dq*}(k)|\ ,\ U_{\mathrm{c,max}}\right\} \tag{5.10}$$

where $\underline{u}_{\mathrm{c,lim}}^{dq*}$ is the limited converter reference voltage. The final controller structure in (5.8) is here named ”basic current controller”.

5.3.2 Improved current controller

The basic current controller in (5.8) works as designed in ideal grid conditions where the feed-forward term provides a perfect voltage compensation. However, problems arise in the presence of unbalanced or distorted voltages. Due to the delays in the discretization and computational time in the control system, a phase shift exists between the actual and feed-forwarded grid voltage. This phase shift is properly compensated only for the fundamental voltage component using the transformation angle $\theta_{\mathrm{g}} + \Delta\theta$ in Fig. 5.2. In the presence of harmonics in the measured voltage $\underline{e}_{\mathrm{g}}$, this leads to a harmonic current flow between the VSC and the grid. Using the estimation method for sequence and harmonic components in Section 4.4.2, the basic current controller can be modified to deal with disturbances from harmonics or unbalanced grid conditions [45].

Direct feed-forwarding of the grid voltage as in (5.8) and providing an angle compensation of $\Delta\theta = 1.5\omega_{\mathrm{g}}T_{\mathrm{s}}$ for transforming the converter reference voltage to the stationary $\alpha\beta$ coordinate will not compensate for harmonics. This is due to the fact that the harmonics rotate with a frequency different from the fundamental. Therefore, the harmonics should be estimated and the angle compensation should be applied accordingly. For example, if the grid voltage e_{g} contains harmonic orders 5^{th}, 7^{th}, 11^{th}, 13^{th} and a negative sequence component at fundamental frequency due to unbalanced voltages, the grid voltage vector can be expressed as

$$\begin{aligned}\underline{e}_{\mathrm{g}}^{\alpha\beta}(k) = \underline{E}_{1}(k)e^{j\theta_{\mathrm{g}}(k)} + \underline{E}_{-1}(k)e^{-j\theta_{\mathrm{g}}(k)} + \underline{E}_{5}(k)e^{-j5\theta_{\mathrm{g}}(k)} + \underline{E}_{7}(k)e^{j7\theta_{\mathrm{g}}(k)} \quad + \\ \underline{E}_{11}(k)e^{-j11\theta_{\mathrm{g}}(k)} + \underline{E}_{13}(k)e^{j13\theta_{\mathrm{g}}(k)}\end{aligned} \tag{5.11}$$

Using the grid angle estimated from the PLL $\tilde{\theta}_{\mathrm{g}}$, (5.11) can be expressed in dq coordinate as

$$\begin{aligned}\underline{e}_{\mathrm{g}}^{dq}(k) = \underline{E}_{1}(k) + \underline{E}_{-1}(k)e^{-j2\theta_{\mathrm{g}}(k)} + \underline{E}_{5}(k)e^{-j6\theta_{\mathrm{g}}(k)} + \underline{E}_{7}(k)e^{j6\theta_{\mathrm{g}}(k)} \quad + \\ \underline{E}_{11}(k)e^{-j12\theta_{\mathrm{g}}(k)} + \underline{E}_{13}(k)e^{j12\theta_{\mathrm{g}}(k)}\end{aligned} \tag{5.12}$$

where $\underline{E}_{5}$, $\underline{E}_{7}$, $\underline{E}_{11}$ and $\underline{E}_{13}$ represent slowly varying harmonic voltage phasors. $\underline{E}_{1}$ and $\underline{E}_{-1}$ are the positive and negative sequence component voltage phasors at fundamental frequency respectively. The fundamental positive sequence component in dq coordinate $\underline{E}_{1}$ can be used as an input to the PLL for grid synchronization without the influence of harmonics or the negative sequence component. Similarly, the filter current in dq coordinate can be written as

$$\underline{i}_{\mathrm{f}}^{dq}(k) = \underline{I}_1(k) + \underline{I}_{-1}(k)e^{-j2\theta_{\mathrm{g}}(k)} + \underline{I}_5(k)e^{-j6\theta_{\mathrm{g}}(k)} + \underline{I}_7(k)e^{j6\theta_{\mathrm{g}}(k)} + \underline{I}_{11}(k)e^{-j12\theta_{\mathrm{g}}(k)} + \underline{I}_{13}(k)e^{j12\theta_{\mathrm{g}}(k)} \tag{5.13}$$

where $\underline{I}_5$, $\underline{I}_7$, $\underline{I}_{11}$ and $\underline{I}_{13}$ represent slowly varying harmonic current phasors. The terms $\underline{I}_1$ and $\underline{I}_{-1}$ are the positive and negative sequence component current phasors at fundamental frequency respectively. With the voltage phasors ($\underline{E}_i$) or current phasors ($\underline{I}_i$) representing the state vector $\mathbf{h}$ and the observation matrix $\mathbf{\Phi}$ as given by (5.14), the RLS based estimator in Section 4.4.2 can be used to estimate the voltage or current phasors.

$$\mathbf{\Phi}(k) = \begin{bmatrix} 1 & e^{-j2\tilde{\theta}_{\mathrm{g}}(k)} & e^{-j6\tilde{\theta}_{\mathrm{g}}(k)} & e^{j6\tilde{\theta}_{\mathrm{g}}(k)} & e^{-j12\tilde{\theta}_{\mathrm{g}}(k)} & e^{j12\tilde{\theta}_{\mathrm{g}}(k)} \end{bmatrix} \tag{5.14}$$

When the harmonic compensation is included in the controller in (5.8), the harmonic components in the grid voltage are estimated and correctly compensated before feed-forwarding them. When the grid voltage $\underline{e}_{\mathrm{g}}$ is stiff ($L_{\mathrm{g}} << L_{\mathrm{f}}$ in Fig. 5.3), a feed-forward of the grid voltage as in (5.15) will remove the harmonic disturbances where $\mathbf{\Phi}_{\mathrm{c}}$ is the observation matrix with the correct angle compensation for each harmonics. On the other hand, for a weak connection point where the grid voltage dynamics are affected by the current injection from the VSC, a closed-loop control of the current may be required. For this, the harmonic current phasors are estimated and a PI controller can be used to control the disturbances to zero. In this case, (5.15) will be modified to (5.16) to control the same harmonics.

$$\tilde{\underline{e}}_{\mathrm{g}}^{dq}(k) = \mathbf{\Phi}_{\mathrm{c}}(k)\tilde{\underline{\mathbf{E}}}(k) \tag{5.15}$$

with

$$\mathbf{\Phi}_{\mathrm{c}}(k) = \begin{bmatrix} 1 & e^{-j2(\tilde{\theta}_{\mathrm{g}}(k)+\Delta\theta)} & e^{-j6(\tilde{\theta}_{\mathrm{g}}(k)+\Delta\theta)} & e^{j6(\tilde{\theta}_{\mathrm{g}}(k)+\Delta\theta)} & e^{-j12(\tilde{\theta}_{\mathrm{g}}(k)+\Delta\theta)} & e^{j12(\tilde{\theta}_{\mathrm{g}}(k)+\Delta\theta)} \end{bmatrix}$$

$$\tilde{\underline{\mathbf{E}}}(k) = \begin{bmatrix} \tilde{\underline{E}}_1(k) & \tilde{\underline{E}}_{-1}(k) & \tilde{\underline{E}}_5(k) & \tilde{\underline{E}}_7(k) & \tilde{\underline{E}}_{11}(k) & \tilde{\underline{E}}_{13}(k) \end{bmatrix}^{\mathrm{T}}$$

$$\tilde{\underline{e}}_{\mathrm{g}}^{dq}(k) = \mathbf{\Phi}_{\mathrm{c}}(k)\left[\tilde{\underline{\mathbf{E}}}(k) - \left(\gamma_{\mathrm{hc}} + R_{\mathrm{ha}}\right)\hat{L}_{\mathrm{f}}\tilde{\underline{\mathbf{I}}}_{\mathrm{h}}(k) - \gamma_{\mathrm{hc}}\left(\hat{R}_{\mathrm{f}} + R_{\mathrm{ha}}\right)T_{\mathrm{s}}\sum_{n=0}^{k}\tilde{\underline{\mathbf{I}}}_{\mathrm{h}}(n)\right] \tag{5.16}$$

with

$$\tilde{\underline{\mathbf{I}}}_{\mathrm{h}}(k) = \begin{bmatrix} 0 & \tilde{\underline{I}}_{-1}(k) & \tilde{\underline{I}}_5(k) & \tilde{\underline{I}}_7(k) & \tilde{\underline{I}}_{11}(k) & \tilde{\underline{I}}_{13}(k) \end{bmatrix}^{\mathrm{T}}$$

where $\tilde{\underline{\mathbf{I}}}_{\mathrm{h}}(k)$ is the estimated harmonic current phasor, γ_{hc} is the bandwidth of the closed-loop harmonic compensator and R_{ha} is a small active damping term. As the harmonics are steady

state quantities, the harmonic compensator bandwidth γ_{hc} is chosen much lower than the fundamental current controller bandwidth γ_{cc}. This choice of bandwidth also helps in the sense that the harmonic compensator will not affect the current controller performance at fundamental frequency. The harmonic current components can be estimated much faster than the closed loop bandwidth γ_{hc}. Including the harmonic compensation, the controller in (5.8) is expressed as in (5.17) where $\underline{\tilde{e}}_{\mathrm{g}}^{dq}(k)$ is given by (5.16). The controller in (5.17) is here named "improved current controller".

$$\begin{aligned}\underline{u}_{\mathrm{c}}^{dq*}(k) = \underline{\tilde{e}}_{\mathrm{g}}^{dq}(k) + \left(j\hat{\omega}_{\mathrm{g}}\hat{L}_{\mathrm{f}} - R_{\mathrm{a}}\right)\underline{i}_{\mathrm{f}}^{dq}(k) + \gamma_{\mathrm{cc}}\hat{L}_{\mathrm{f}}\left(\underline{i}_{\mathrm{f}}^{dq*}(k) - \underline{i}_{\mathrm{f}}^{dq}(k)\right) \quad + \\ \gamma_{\mathrm{cc}}\left(\hat{R}_{\mathrm{f}} + R_{\mathrm{a}}\right)T_{\mathrm{s}}\sum_{n=0}^{k}\left(\underline{i}_{\mathrm{f}}^{dq*}(n) - \underline{i}_{\mathrm{f}}^{dq}(n) + \underline{i}_{\mathrm{err}}^{dq}(n)\right)\end{aligned} \tag{5.17}$$

The modification to the basic controller will enable the harmonic or negative sequence current injection from the converter to be zero in steady state. If the purpose is to control the harmonic or negative sequence currents as in active filters or supplying unbalanced load, the same control structure can be used. A similar controller is found in the literatures where resonant filters are used in [40][46][47] and multiple reference-frames are used in [48][49].

5.4 Phase-Locked Loop (PLL)

For synchronization purpose in grid-connected VSCs, a PLL that tracks the phase of the positive sequence voltage vector is typically employed. The PLL should be robust against harmonics, grid voltage unbalances and faults [33][35]. When fast synchronization is not needed, good harmonic rejection from the PLL can be achieved by choosing a low bandwidth. For accurate synchronization against grid voltage unbalances, the sequence estimation method described in Section 4.4.2 and implemented in dq reference frame can be used. The block diagram of the PLL with the sequence estimation in dq coordinate system is shown in Fig. 5.4.

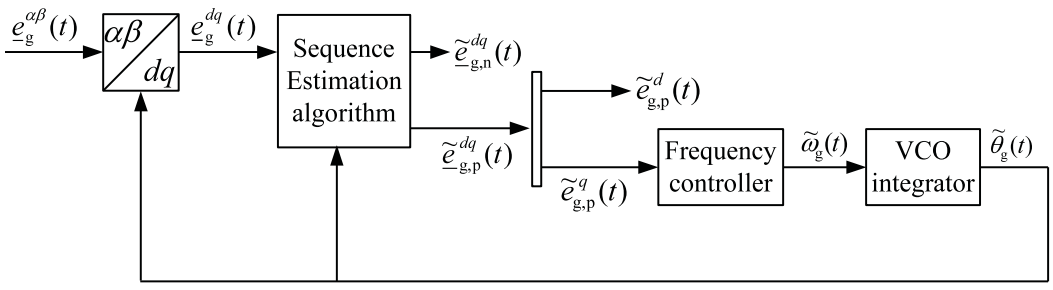

Fig. 5.4 Block diagram of PLL.

For a voltage-oriented coordinate system, the PLL controller tries to force the imaginary part of the positive sequence voltage $\underline{\tilde{e}}_{\mathrm{g,p}}^{dq}$ to zero. Therefore, the imaginary part ($\tilde{e}_{\mathrm{g,p}}^{q}$) normalized to the grid voltage is used as an angle error (ε_{θ}) to setup the PLL algorithm as

$$\begin{aligned}\tilde{\omega}_{\mathrm{g}}(k+1) &= \tilde{\omega}_{\mathrm{g}}(k) + K_{\mathrm{i}} T_{\mathrm{s}} \varepsilon_{\theta}(k) \\ \tilde{\theta}_{\mathrm{g}}(k+1) &= \tilde{\theta}_{\mathrm{g}}(k) + T_{\mathrm{s}} \tilde{\omega}_{\mathrm{g}}(k) + K_{\mathrm{p}} T_{\mathrm{s}} \varepsilon_{\theta}(k)\end{aligned} \tag{5.18}$$

With α_{PLL} representing the PLL bandwidth, the controller parameters are calculated as [37]

$$\varepsilon_{\theta}(k) = \tilde{e}^{q}_{\mathrm{g,p}}(k) \big/ \left| \underline{\tilde{e}}^{dq}_{\mathrm{g,p}}(k) \right| \quad , \qquad K_{\mathrm{p}} = 2\alpha_{\mathrm{PLL}} \quad , \qquad K_{\mathrm{i}} = \alpha^{2}_{PLL}$$

Choosing the bandwidth of the PLL is a trade of between harmonic rejection and speed of response. When the sequence estimation is included in the PLL, it provides a 0 pu gain at the negative sequence component and a smaller gain at harmonic frequencies. Hence, the bandwidth of the PLL can be chosen higher. For this application, the parameters of the PLL are chosen to get a bandwidth of 31.4 rad/s. Figure 5.5 shows a simulation of the PLL response to a sudden phase angle jump and single phase fault.

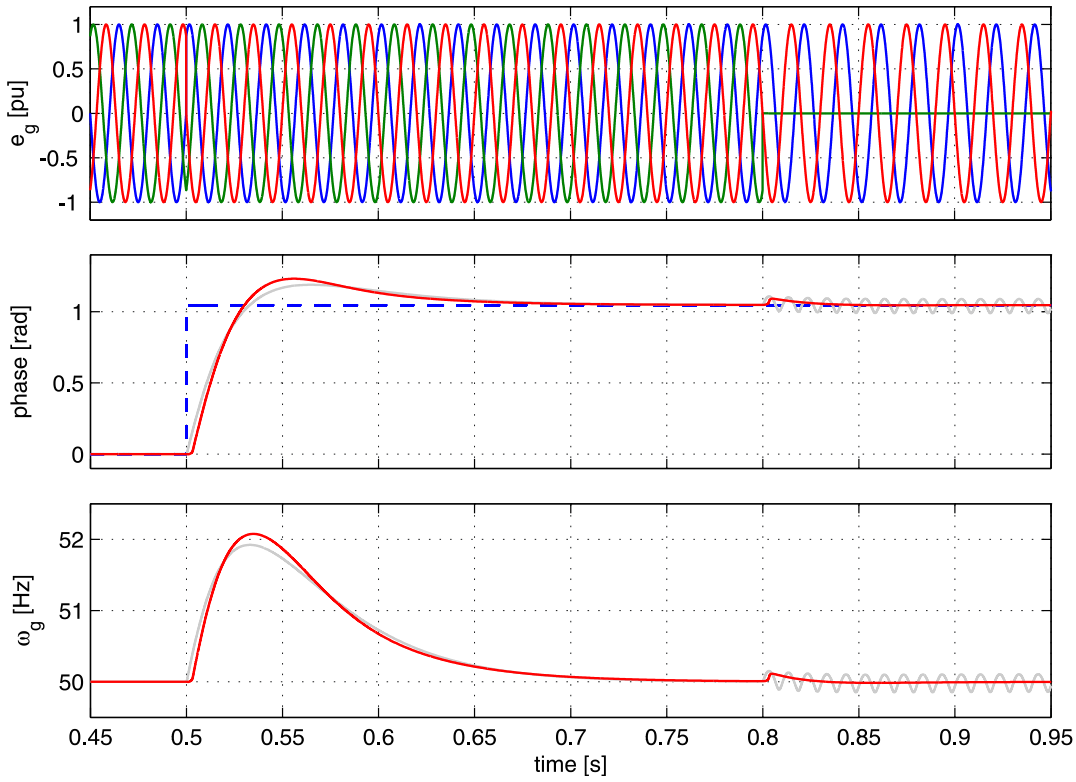

Fig. 5.5 Phase and frequency response of PLL for a sudden phase angle jump at 0.5 s and single phase fault at 0.8 s; Top: three phase grid voltage; Middle: Phase angle jump (dashed), PLL phase estimate with no sequence estimation (gray) and with sequence estimation (red); Bottom: PLL grid frequency estimate with no sequence estimation (gray) and with sequence estimation (red).

5.5 Outer controller loops

In this section, the different outer controller loops will be described. As shown in Fig. 5.2, the current reference input to the current controller is calculated through these outer controller loops. The speed of these controllers is typically selected to be much slower than the inner current controller loop to guarantee stability. For this reason, the current controller can be considered infinitely fast when designing the parameters of the outer controller loops.

5.5.1 AC voltage controller

To control the magnitude of the voltage at the connection point, an AC voltage controller using reactive power injection is used. Injection of reactive current at PCC results in a change of the voltage magnitude E_{g} due to the variation of the voltage drop over the impedance of the system at the connection point X_{pcc} [1][50]. To derive the controller parameters, a simplified block diagram of an AC voltage controller with droop control as in Fig. 5.6 is used. The signal E_{g0} represents the steady state voltage at PCC. If capacitive current corresponding to positive reactive current is injected, the change in voltage magnitude would be negative and hence the system is represented by a gain of $-X_{\mathrm{pcc}}$. The negative gain is due to the selected orientation for the rotating dq system (voltage oriented system is here selected) and the reference filter current direction.

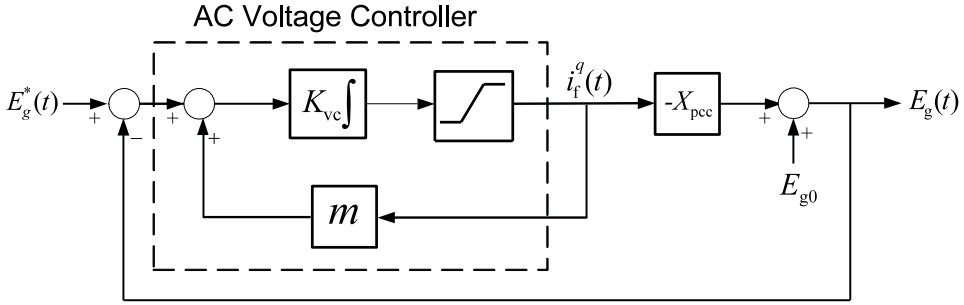

Fig. 5.6 Simplified Block diagram of an AC voltage controller.

Using small signal variations, the transfer function (G_{vc}) from the change in voltage reference (ΔE_{g}^*) to the change in PCC voltage magnitude (ΔE_{g}) is given by (5.19) where K_{vc} is the integral gain and m is a droop constant. For perfect voltage control, the droop is set to zero. To obtain a voltage controller bandwidth of γ_{vc}, assuming perfect knowledge of the system impedance X_{pcc} and no droop, the integral gain is calculated as in (5.20). The actual bandwidth of the voltage controller depends on the system impedance and the parameter K_{vc} is usually calculated assuming the largest value of X_{pcc} corresponding to the smallest short circuit power at the PCC [1]. The reactive current reference for AC voltage control is given by (5.21).

$$G_{\mathrm{vc}}(s) = \frac{\Delta E_{\mathrm{g}}(s)}{\Delta E_{\mathrm{g}}^*(s)} = \frac{-K_{\mathrm{vc}} X_{\mathrm{pcc}}}{s - K_{\mathrm{vc}}\left(X_{\mathrm{pcc}} + m\right)} \tag{5.19}$$

$$K_{\mathrm{vc}} = -\gamma_{\mathrm{vc}} \Big/ \hat{X}_{\mathrm{th}} \tag{5.20}$$

$$i_{\mathrm{f}}^{q*}(k+1) = i_{\mathrm{f}}^{q*}(k) + K_{\mathrm{vc}} T_{\mathrm{s}} \left(E_{\mathrm{g}}^{*}(k) - E_{\mathrm{g}}(k) + m i_{\mathrm{f}}^{q}(k) \right) \tag{5.21}$$

5.5.2 DC-link voltage controller

When operating the VSC, the DC-link voltage should be controlled within allowable limits of the nominal value. If only reactive power injection is used, the DC-link voltage control can be achieved by controlling the active current reference and drawing a small active power from the AC grid [1][50]. If an energy storage is mounted on the DC side of the VSC, the control of the DC-link voltage also depends on control of the energy source [19]. Among the energy storage devices that can be integrated to the VSC include capacitors, batteries, superconducting magnetic coil and supercapacitors [11][12][13][23][51]. The modeling of the energy storage is outside the focus of this work and will not be considered here. For the performed simulations, an infinite voltage source will be connected to the DC-link of the VSC, while for the experimental setup a DC generator with controlled output voltage will be used as an energy storage. For this reason, a DC-link voltage controller is not implemented.

5.5.3 POD and TSE controllers

To achieve Power Oscillation Damping (POD) and Transient Stability Enhancement (TSE) functions, the active and reactive power from the VSC should be controlled in response to power system disturbances. The derivation of the required active and reactive current references to provide these auxiliary functions, $i_{\mathrm{f,aux}}^{d*}$ and $i_{\mathrm{f,aux}}^{q*}$ respectively, will be carried out in the next chapter. These current references can be directly used as an input to the current controller to achieve the required stability enhancement function. However, reactive current injection is also used to control the voltage at PCC. If the stability enhancement function is to be included together with the AC voltage controller, (5.21) can be modified as in (5.22) where the PCC voltage is modulated based on ($i_{\mathrm{f,aux}}^{q*}$). In this case, the speed of stability enhancement function which depends on the power system dynamics should be slower than the AC voltage controller which is usually the case. Similarly, active current injection is used to control the DC-link voltage. If the stability enhancement function is to be used together with the DC-link voltage controller, the active current reference is described as in (5.23) where $i_{\mathrm{f,dc}}^{d*}$ is the output of the DC-link voltage controller. Finally, the current references will be limited as in (5.24) and passed to the current controller where I_{max}^{d} is the maximum active current limit which depends on the rating of energy source and I_{max} is the maximum current limit of the converter.

$$i_{\mathrm{f}}^{q*}(k+1) = i_{\mathrm{f}}^{q*}(k) + K_{\mathrm{vc}} T_{\mathrm{s}} \left(E_{\mathrm{g}}^{*}(k) - E_{\mathrm{g}}(k) + m i_{\mathrm{f}}^{q*}(k) + \hat{X}_{\mathrm{pcc}} i_{\mathrm{f,aux}}^{q*}(k) \right) \tag{5.22}$$

$$i_{\mathrm{f}}^{d*}(k) = i_{\mathrm{f,dc}}^{d*}(k) + i_{\mathrm{f,aux}}^{d*}(k) \tag{5.23}$$

$$\underline{i}_{\mathrm{f,lim}}^{dq*}(k) = \frac{i_{\mathrm{f,lim}}^{d*}(k) + j i_{\mathrm{f,lim}}^{q*}(k)}{|i_{\mathrm{f,lim}}^{d*}(k) + j i_{\mathrm{f,lim}}^{q*}(k)|} \min\left\{|i_{\mathrm{f,lim}}^{d*}(k) + j i_{\mathrm{f,lim}}^{q*}(k)|\ ,\ I_{\max}\right\} \tag{5.24}$$

where,

$$\underline{i}_{\mathrm{f,lim}}^{d*}(k) = \frac{i_{\mathrm{f}}^{d*}(k)}{|i_{\mathrm{f}}^{d*}(k)|} \min\left\{|i_{\mathrm{f}}^{d*}(k)|\ ,\ I_{\max}^{d}\right\} \quad , \quad \underline{i}_{\mathrm{f,lim}}^{q*}(k) = \frac{i_{\mathrm{f}}^{q*}(k)}{|i_{\mathrm{f}}^{q*}(k)|} \min\left\{|i_{\mathrm{f}}^{q*}(k)|\ ,\ I_{\max}\right\}$$

5.6 Simulation verification

The performance of the inner current controller loop will be verified in this section through simulation. Considering a distorted grid, the performance of the basic current controller and improved current controllers will be compared.

The basic controller in (5.8) is simulated using a constant DC-link voltage. the sampling frequency is equal to 5 kHz. PWM is used to generate the switching pattern for the VSC valves. The switching frequency f_s is equal to the sampling frequency and set to 5 kHz. Figure 5.7 shows the current response to a step reference change for an ideal grid (no harmonic distortion) and a distorted grid. For the distorted grid, a harmonic magnitude in pu of 0.015, 0.01, 0.002 and 0.002 for the 5^{th}, 7^{th}, 11^{th} and 13^{th} order harmonics, respectively, is assumed. For the ideal grid, the discrete controller works as expected (Fig. 5.7 plots a, c) for a current controller bandwidth of γ_{cc} = 3141.6 rad/s and active damping R_{a} = 0.063 Ω. In case of distorted grid, the injected currents will be affected by low-order harmonics (Fig. 5.7 plots b, d).

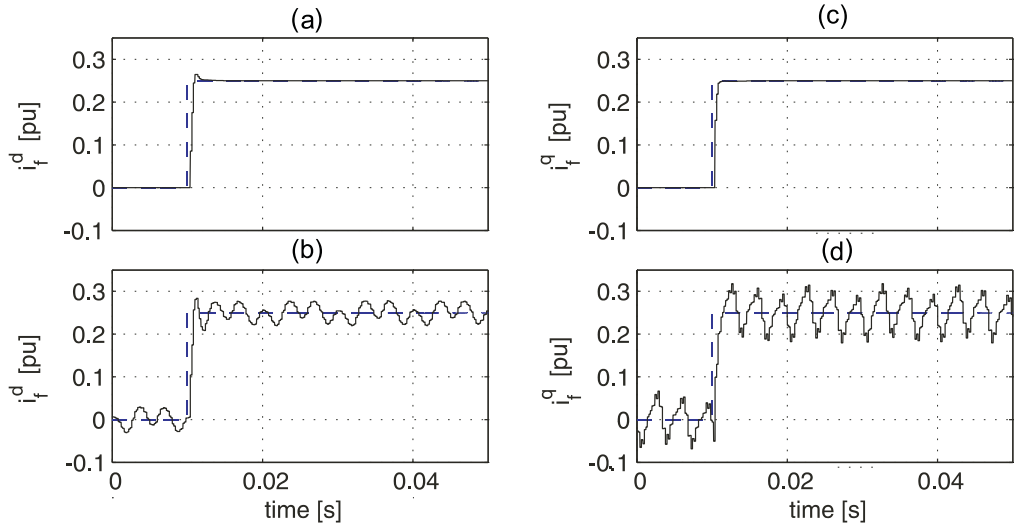

Fig. 5.7 Simulated basic and improved current controller response for *d*-component (left) and *q*-component (right); (a, c) ideal grid and discrete controller, (b, d) distorted grid and discrete controller; reference current (dashed) and actual current (solid).

To show that this problem exists only in the discrete controller, the controller in (5.8) has been implemented in continuous time using the same distorted grid and the results are shown in

Fig. 5.8.

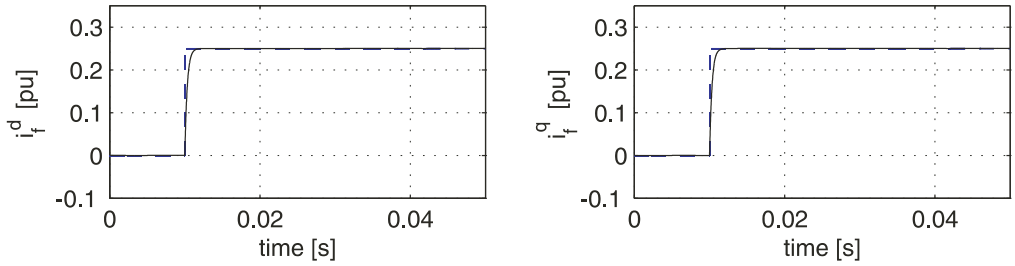

Fig. 5.8 Simulated basic current controller response for d-component (left) and q-component (right) with distorted grid and continuous controller; reference current (dashed) and actual current (solid).

To evaluate the performance of the improved controller in (5.17), a grid distorted by 5^{th}, 7^{th}, $11^{\text{th}}$and 13^{th} order harmonics and a negative sequence component at fundamental frequency has been considered. The parameters γ_{hc} = 628.3 rad/s and R_{ha} = 0.0625 Ω are used for the simulation. Figure 5.9 shows the performance of the basic and improved controllers. The improved controller significantly reduces the disturbances from harmonics and grid voltage unbalances.

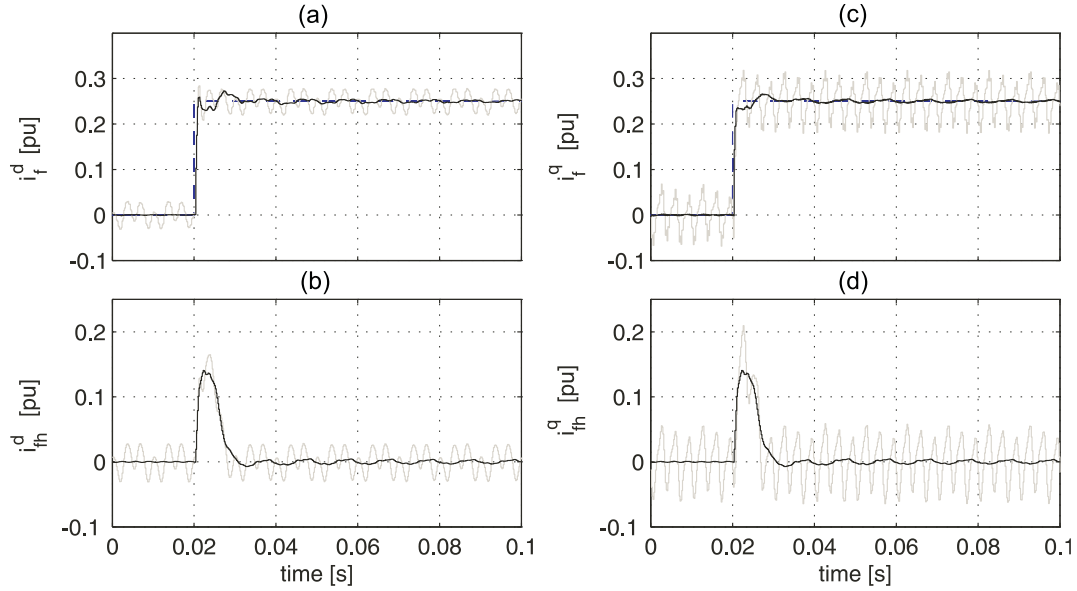

Fig. 5.9 Simulated current controller response with basic controller (gray) and improved controller (black). (a) d-component current, (b) d-component harmonic current, (c) q-component current and (d) q-component harmonic current; reference current (dashed) and actual current (solid).

5.7 Conclusions

Starting with the classical PI current controller, an improved current controller for E-STACOM in the presence of grid harmonics has been derived using the estimation algorithm in Chapter 4.

The performance of the current controller has been verified through simulation. For synchronization purpose in the control of E-STATCOM, a PLL that is robust against harmonics and grid voltage unbalances has been derived using the sequence estimation method described in the previous chapter. The outer controller loops such as AC voltage controller, DC-link voltage controller, POD and TSE controllers have been described.

Chapter 6

Use of E-STATCOM for power system stability enhancement

6.1 Introduction

In this chapter, the control strategy for stability enhancement using E-STATCOM will be described. Starting with a simple two machine model of a power system, the effect of active and reactive power injection on the generator output power will be studied and a control strategy for system stability enhancement will be derived. Stability analysis of the system model will be made and the dynamic performance of the control strategy will be verified by simulation.

6.2 System modeling for controller design

A simplified power system model, as the one depicted in Fig. 6.1, is used to study the performance of the E-STATCOM on the power system dynamics. The investigated system approximates an aggregate model of a two area power system, where each area is represented by a synchronous generator [6][24]. The E-STATCOM is assumed to be connected at arbitrary points along the transmission line for analysis purpose. Even if the E-STATCOM can be connected at one point in the transmission line, a different connection point can be seen as a change in system configuration between the two areas, for instance, following a fault and a subsequent disconnection of one of the parallel transmission lines.

As discussed in Section 2.6, the synchronous generators are modeled as voltage sources of constant magnitude ($V_{\mathrm{g1}}, V_{\mathrm{g2}}$) and dynamic rotor angles ($\delta_{\mathrm{g1}}, \delta_{\mathrm{g2}}$) behind a transient impedance ($X'_{\mathrm{d1}}, X'_{\mathrm{d2}}$). The generators are connected through a transformer and a transmission line. Since the frequency of the generators does not change significantly and the electrical transients extinguish quickly for the investigated transient stability studies, it can be assumed that the system is in steady state from an electrical point of view, meaning that the transformers and transmission lines can be represented by their reactance values (X_{t1}, X_{t2}, X_{L1} and X_{L2}) [24], where the resistance values are ignored for simpler analytical expressions. As shown in Section 2.6, if

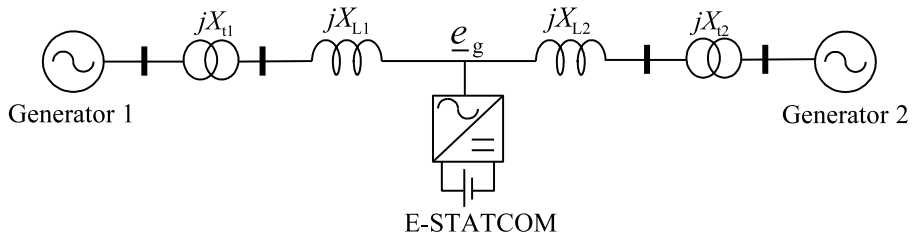

Fig. 6.1 Simplified two machine system with E-STATCOM.

the mechanical damping in the generators is neglected, the overall damping for the investigated system is equal to zero. Therefore, the model is appropriate to allow a conservative approach of the impact of the E-STATCOM when used for stability studies [52]. As the current controller of the E-STATCOM is much faster than the low-frequency electromechanical dynamics, the E-STATCOM will be modeled as an ideal controlled current source. The controlled injected active and reactive current components are indicated as i_{f}^{d} and i_{f}^{q} respectively, where the PLL is synchronized with the phase θ_{g} of the grid voltage at PCC, $\underline{e}_{\mathrm{g}}$. The electrical connection point of the converter along the transmission line is expressed as a function of the parameter a as

$$a = \frac{X_1}{X_1 + X_2} \tag{6.1}$$

where,

$$X_1 = X_{\mathrm{d1}}^{'} + X_{\mathrm{t1}} + X_{\mathrm{L1}} \quad , \quad X_2 = X_{\mathrm{d2}}^{'} + X_{\mathrm{t2}} + X_{\mathrm{L2}}$$

An equivalent circuit representation of the investigated system in Fig. 6.1 for stability studies is shown in Fig. 6.2.

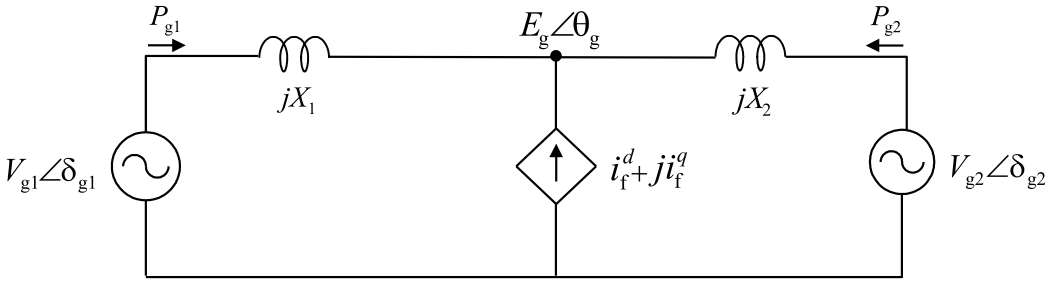

Fig. 6.2 Equivalent circuit for two machine system with E-STATCOM.

The level of stability enhancement provided by the converter depends on how much the active power output from the generators is changed by the injected currents. For the system in Fig. 6.2, the change in active power output from the generators due to injected active and reactive power from the E-STATCOM is calculated as in (6.2) - (6.5) where ($\Delta P_{\mathrm{g1,P}}, \Delta P_{\mathrm{g2,P}}$) and ($\Delta P_{\mathrm{g1,Q}}, \Delta P_{\mathrm{g2,Q}}$) represent the change in active power from the corresponding generators due to injected active and reactive power, respectively [52]. The injected active power P_{inj} and injected reactive power Q_{inj} from the converter are given by (6.6) - (6.7). The initial steady state PCC voltage magnitude (E_{g0}) and generator rotor angles ($\delta_{\mathrm{g10}}, \delta_{\mathrm{g20}}$) correspond to the operating point where the converter is not injecting a current.

$$\Delta P_{\mathrm{g1,Q}} \approx \left[\frac{V_{\mathrm{g1}} V_{\mathrm{g2}} \sin(\delta_{\mathrm{g10}} - \delta_{\mathrm{g20}}) a(1-a)}{E_{\mathrm{g0}}^2}\right] Q_{\mathrm{inj}} \tag{6.2}$$

$$\Delta P_{\mathrm{g2,Q}} \approx -\left[\frac{V_{\mathrm{g1}} V_{\mathrm{g2}} \sin(\delta_{\mathrm{g10}} - \delta_{\mathrm{g20}}) a(1-a)}{E_{\mathrm{g0}}^2}\right] Q_{\mathrm{inj}} \tag{6.3}$$

$$\Delta P_{\mathrm{g1,P}} \approx -\left[\frac{V_{\mathrm{g1}}^2 (1-a)^2 + V_{\mathrm{g1}} V_{\mathrm{g2}} \cos(\delta_{\mathrm{g10}} - \delta_{\mathrm{g20}}) a(1-a)}{E_{\mathrm{g0}}^2}\right] P_{\mathrm{inj}} \tag{6.4}$$

$$\Delta P_{\mathrm{g2,P}} \approx -\left[1 - \frac{V_{\mathrm{g1}}^2 (1-a)^2 + V_{\mathrm{g1}} V_{\mathrm{g2}} \cos(\delta_{\mathrm{g10}} - \delta_{\mathrm{g20}}) a(1-a)}{E_{\mathrm{g0}}^2}\right] P_{\mathrm{inj}} \tag{6.5}$$

$$P_{\mathrm{inj}} \approx E_{\mathrm{g0}} i_{\mathrm{f}}^d \tag{6.6}$$

$$Q_{\mathrm{inj}} \approx -E_{\mathrm{g0}} i_{\mathrm{f}}^q \tag{6.7}$$

It can be seen from (6.2) - (6.7) that the change in active power output from the generators for a given active and reactive power injection from the E-STATCOM depends on the location of the converter a as well as on the amount of injected power (P_{inj}, Q_{inj}). As indicated from (6.2) - (6.3), the effect of reactive power injection depends on the magnitude and direction of transmitted power from the generators. From observation of the influence of active and reactive power injection on the power output of the generators, control input signals for the E-STATCOM to provide stability enhancement will be derived in the next section.

6.3 Controller design

In this section, the derivation of POD and TSE controllers from local measurement signals such as PCC voltage magnitude (E_{g}), PCC voltage phase (θ_{g}) and active power transfer between two areas (P_{g12}) will be derived. For this, the simplified two machine system described in the previous section will be used.

6.3.1 Power Oscillation Damping (POD)

Considering the simplified two machine system in Fig. 6.1 and the equation of motion in Section 2.3, the active power output from each generator should change in proportion to the change in its speed to provide damping [6][24]. From (6.2) - (6.5), it can be observed that the effect of injected active and reactive power on the generator active power output highly depends on the parameter a, i.e. on the location of the E-STATCOM. Using the system in Fig. 6.2, a control input signal that contains information on the speed variation of the generators can be derived. When the E-STATCOM is not injecting any current, the variation of various local signals at

different E-STATCOM connection points using the dynamic generator rotor angles (δ_{g1}, δ_{g2}) is given by (6.8) - (6.10). From small signal point of view, and under the assumption that the PCC voltage magnitude along the line (E_{g}) does not change much, the required control input signals can be derived from the change in PCC voltage magnitude (ΔE_{g}), phase ($\Delta\theta_{\mathrm{g}}$) or transmitted active power (ΔP_{g12}) as in (6.11) - (6.13) [52].

$$E_{\mathrm{g}} = \sqrt{\left[(1-a)V_{\mathrm{g1}}\right]^2 + \left[aV_{\mathrm{g2}}\right]^2 + 2a(1-a)V_{\mathrm{g1}}V_{\mathrm{g2}}\cos(\delta_{\mathrm{g1}} - \delta_{\mathrm{g2}})} \tag{6.8}$$

$$\theta_{\mathrm{g}} = \delta_{\mathrm{g2}} + \tan^{-1}\left[\frac{(1-a)V_{\mathrm{g1}}\sin(\delta_{\mathrm{g1}} - \delta_{\mathrm{g2}})}{(1-a)V_{\mathrm{g1}}\cos(\delta_{\mathrm{g1}} - \delta_{\mathrm{g2}}) + aV_{\mathrm{g2}}}\right] \tag{6.9}$$

$$P_{\mathrm{g12}} = \frac{V_{\mathrm{g1}}V_{\mathrm{g2}}\sin(\delta_{\mathrm{g1}} - \delta_{\mathrm{g2}})}{X_1 + X_2} \tag{6.10}$$

$$\frac{d\Delta E_{\mathrm{g}}}{dt} \approx -\left\{\frac{a(1-a)V_{\mathrm{g1}}V_{\mathrm{g2}}\sin(\delta_{\mathrm{g10}} - \delta_{\mathrm{g20}})}{E_{\mathrm{g0}}}\right\}\omega_{\mathrm{g0}}\left[\Delta\omega_{\mathrm{g1}} - \Delta\omega_{\mathrm{g2}}\right] \tag{6.11}$$

$$\begin{aligned}\frac{d\Delta\theta_{\mathrm{g}}}{dt} \approx &\left\{\frac{\left[(1-a)V_{\mathrm{g1}}\right]^2 + a(1-a)V_{\mathrm{g1}}V_{\mathrm{g2}}\cos(\delta_{\mathrm{g10}} - \delta_{\mathrm{g20}})}{E_{\mathrm{g0}}^2}\right\}\omega_{\mathrm{g0}}\Delta\omega_{\mathrm{g1}} \quad + \\ &\left\{1 - \frac{\left[(1-a)V_{\mathrm{g1}}\right]^2 + a(1-a)V_{\mathrm{g1}}V_{\mathrm{g2}}\cos(\delta_{\mathrm{g10}} - \delta_{\mathrm{g20}})}{E_{\mathrm{g0}}^2}\right\}\omega_{\mathrm{g0}}\Delta\omega_{\mathrm{g2}}\end{aligned} \tag{6.12}$$

$$\frac{d\Delta P_{\mathrm{g12}}}{dt} \approx \left\{\frac{V_{\mathrm{g1}}V_{\mathrm{g2}}\cos(\delta_{\mathrm{g10}} - \delta_{\mathrm{g20}})}{X_1 + X_2}\right\}\omega_{\mathrm{g0}}\left[\Delta\omega_{\mathrm{g1}} - \Delta\omega_{\mathrm{g2}}\right] \tag{6.13}$$

The nominal system frequency is represented by ω_{g0} and ($\Delta\omega_{\mathrm{g1}}, \Delta\omega_{\mathrm{g2}}$) is the speed variation of the generators in pu. The derivative of the change in PCC voltage magnitude, phase and transmitted active power are all dependent on the speed variation of the generators. Moreover, the derivative of the change in PCC voltage magnitude and phase contain information on the location of E-STATCOM as shown in (6.11) - (6.12).

For the two machine system in Fig. 6.1, damping is related to the variation of the speed difference between the two generators, $\Delta\omega_{\mathrm{g12}} = \Delta\omega_{\mathrm{g1}} - \Delta\omega_{\mathrm{g2}}$. For a given speed variation $\Delta\omega_{\mathrm{g12}}$ and initial transmitted power P_{g120}, the derivative of the change in PCC voltage magnitude is maximum at $a = 0.5$ (midpoint of the line) where injection of reactive power results in the maximum change in the generators active power output according to (6.2) - (6.3). On the other hand, the change in the output power from the generators due to injected active power according to (6.4) - (6.5) is maximum at the corresponding generator terminals (i.e. $a = 0$ and $a = 1$) where (6.12) is maximum. No damping is provided by injection of active power at the location where the effect on the change in active power output from each generator is the same, taking into account the inertia constant of the generators. Assuming equal inertia constant for the two generators, this location is at the middle of the line (i.e. $a = 0.5$). At this location the derivative of PCC voltage phase, $d\Delta\theta_{\mathrm{g}}/dt = 0$. This means that $d\Delta\theta_{\mathrm{g}}/dt$ scales the speed variation of the two generators depending on the location and its magnitude changes in proportion to the

level of damping by active power injection. Therefore, $d\Delta\theta_{\mathrm{g}}/dt$ is an appropriate input signal for controlling the active power injection. Similarly, $d\Delta E_{\mathrm{g}}/dt$ varies in proportion to the level of damping by reactive power injection, and hence can minimize injection of reactive power at the generator terminals. Therefore, $d\Delta E_{\mathrm{g}}/dt$ could be a convenient input signal for controlling the reactive power injection. On the other hand, $d\Delta P_{\mathrm{g12}}/dt$ varies linearly with the speed variation of the two generators $d\Delta\omega_{\mathrm{g12}}$ and can be used to control reactive power injection. But, unlike $d\Delta E_{\mathrm{g}}/dt$, it does not depend on the parameter a and its magnitude will be the same at all locations in the investigated system. This means that if $d\Delta P_{\mathrm{g12}}/dt$ is used to control the reactive power, the E-STATCOM may unnecessarily inject reactive power to provide damping at location where its effect is negligible, for instance at the generator terminals. However, the advantage of using $d\Delta P_{\mathrm{g12}}/dt$ for controlling reactive power is that it contains better information about the speed variation of the generators. This is not always the case for $d\Delta E_{\mathrm{g}}/dt$. Consider for example that the PCC voltage E_{g} is controlled and kept to a constant value. This is possible as the AC voltage controller is much faster than low-frequency electromechanical oscillations. In this case, even if the generators are oscillating, the PCC voltage will be constant providing no information about the generator speed variation. Moreover, damping by reactive power injection is achieved by directly controlling the PCC voltage magnitude E_{g} and this creates difficulty to extract the required signal for damping from the voltage signal and at the same time control it. When it comes to transmitted power, the speed variation of the generators can be extracted until all the oscillations are damped. For this reason, derivative of the transmitted power $d\Delta P_{\mathrm{g12}}/dt$ will be used for controlling the reactive power injection in this work.

Even if the analysis so far has been made for two machine system, the result can be easily reduced to single machine infinite bus system by setting $\Delta\omega_{\mathrm{g2}} = \Delta\delta_{\mathrm{g2}} = 0$. In this case, injection of active or reactive power will have no effect on the generator power output if the E-STATCOM is connected at the infinite bus ($a = 1$). Maximum damping by active and reactive power will be provided respectively at the generator terminal ($a = 0$) and midpoint of the line ($a = 0.5$).

To setup the POD controller, the control input signals $d\Delta\theta_{\mathrm{g}}/dt$ and $d\Delta P_{\mathrm{g12}}/dt$ need to be estimated. From the estimates, the active and reactive current references ($i^{d*}_{\mathrm{f,pod}}, i^{q*}_{\mathrm{f,pod}}$) can be calculated using proportional controllers with gains G_{P} and G_{Q} as shown in Fig. 6.3. The components, consisting of only the low-frequency electromechanical oscillation, will be extracted by the RLS estimator described in Section 4.4.1. To estimate the derivative of transmitted power, a phase shift of $\pi/2$ is applied to each oscillation frequency component. Because the derivative of the PCC voltage phase is the same as the frequency estimate of the PLL, the low frequency electromechanical oscillation component is extracted from the frequency estimate of the PLL.

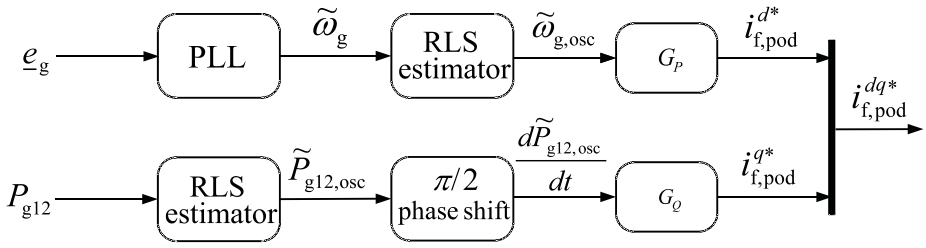

Fig. 6.3 Block diagram of the POD controller.

6.3.2 Transient Stability Enhancement (TSE)

Transient stability enhancement function is necessary to ensure robust operation of the power system following large disturbances, such as transmission line faults. As an example, Fig. 6.4 (left) shows a power angle curve for the two machine system in Fig. 6.1. In this example, the power angle curve before, during and after the fault is shown in black, gray and green dashed line, respectively. The fault is cleared at angle δ_1. As described in Section 2.7, for a given transmitted power and fault clearing time, the stability of the system following fault clearing depends on the available deceleration area of the post-fault system such as area DEFH in Fig. 6.4 (left). During fault, the machines will be accelerating away from each other increasing the angle between them. When the fault is removed, the machines will start to decelerate. But the angle between them increases until the second swing is started, where the relative speed between the generators is zero. This is where the acceleration area during fault ABCD is equal to the deceleration area DEFH at angle δ_3. If the angle between the generators during the first swing has increased beyond the maximum angle δ_4, the system becomes unstable [25].

By using active or reactive power injection, the deceleration area can be increased in the first swing of the generators to have larger stability margin [1]. Figure 6.4 (right) shows the post-fault system with and without transient stability enhancement function. The power angle curve with reactive power and active power injection for TSE are generated at one connection point of the E-STATCOM and using the expressions in (6.2) and (6.4), respectively. By using the enhancement function, the power output between the two areas after fault clearing can be increased during the first swing, where the power angle between the machines is increasing. This increases the deceleration area and hence decrease the angle δ_3 where the second swing starts. As soon as the second swing starts, the machines will continue to decelerate decreasing the angle between them with deceleration area DEFG, $\mathrm{DE_1F_1G}$ or $\mathrm{DE_2F_2G}$ depending on the post-fault system. This deceleration area will result in more swings below the initial power angle δ_0 in the second cycle. Therefore, the power output should be reduced by the end of the first swing to keep the enhancement function for next swing. This means that the increased transmitted power indicated in the power angle curves in Fig. 6.4 (right) should be only used when the machine during the angle difference advancement; opposite countermeasure must be taken otherwise.

To implement a stability enhancement function, the output power from generators should be increased or decreased if the power angle between the generators is increasing or decreasing, respectively. The nature of the angle between the two generators can be observed from measurement of relative speed between the two generators. But to implement this using local signals,

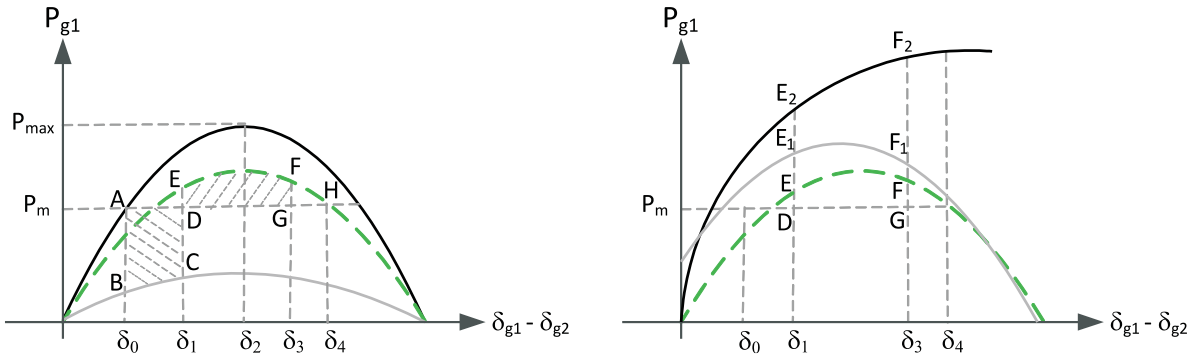

Fig. 6.4 Left: Power angle curve before fault (black), during fault (gray) and after fault (green dashed) without transient stability enhancement; Right: Power angle curve for post-fault system with no enhancement (green dashed), enhancement by reactive power injection (black) and enhancement by active power injection (gray).

the measured power flow between the generators can be used. The derivative of power between the two areas provides this information [1]. A positive or negative power derivative implies an increasing or decreasing relative power angle between the generators, respectively. When the acceleration of the machines is below a given value, the enhancement function is removed and the power oscillation damping function will be started. Observe that for cases where the fault is cleared after the maximum power transfer angle of the post-fault system δ_2 in Fig. 6.4 (left) for example, the generator angle increases while the derivative of power is negative implying that remote measurements might be necessary to provide the required enhancement function.

To provide the transient stability enhancement function as described using reactive power injection, the PCC voltage magnitude can be increased or decreased temporarily beyond the nominal value to increase or decrease the power transfer between the two areas respectively, as in (6.14). This is typically done by using a “bang-bang” control action, meaning that the compensator is controlled either fully capacitive or fully inductive, depending on the sign of the power transfer derivative. However, absorption of active power will increase the power transfer from generator 1 and decrease the power transfer to generator 2 according to (6.4) - (6.5). This means that the location of the E-STATCOM has a big impact on the TSE performance. To get the enhancement function, active current will be absorbed when the generator angle is increasing and the E-STATCOM is closer to generator 1 (this means that $|\Delta P_{\mathrm{g1,P}}| > |\Delta P_{\mathrm{g2,P}}|$ in (6.4) - (6.5)) $i^{d*}_{\mathrm{f,tse}}$. Likewise, active current $i^{d*}_{\mathrm{f,tse}}$ will be injected when the generator angle is decreasing. On the other hand, when E-STATCOM is closer to generator 2 (this means that $|\Delta P_{\mathrm{g2,P}}| > |\Delta P_{\mathrm{g1,P}}|$ in (6.4) - (6.5)), active current $i^{d*}_{\mathrm{f,tse}}$ is injected when the generator angle is increasing. Likewise, active current $i^{d*}_{\mathrm{f,tse}}$ is absorbed when the generator angle is decreasing.

$$E^*_{\mathrm{g}} = \begin{cases} 1.1\mathrm{pu} & , \quad \frac{dP_{\mathrm{g12}}}{dt} > 0 \\ 0.9\mathrm{pu} & , \quad \frac{dP_{\mathrm{g12}}}{dt} < 0 \end{cases} \tag{6.14}$$

The algorithm is described in (6.15) where $I^{\max}_{d,\mathrm{tse}}$ represents the maximum active current for transient stability enhancement. The problem with active power injection for transient stability

enhancement is the difficulty to know the location of the E-STATCOM after a system disturbance. It is of importance to notice that the algorithm described in (6.15) might lead to a quick discharge of the energy storage. However, the algorithm can be applied for the absorption mode only ($dP_{\mathrm{g12}}/dt > 0$); in this case, a dc-chopper must be installed in the dc side of the converter in order to burn the exceeding energy from the grid.

$$i_{\mathrm{f,tse}}^{d*} = \begin{cases} -I_{d,\mathrm{tse}}^{\max}\mathrm{sign}(|\Delta P_{\mathrm{g1,P}}| - |\Delta P_{\mathrm{g2,P}}|) & , \quad \frac{dP_{\mathrm{g12}}}{dt} > 0 \\ \\ I_{d,\mathrm{tse}}^{\max}\mathrm{sign}(|\Delta P_{\mathrm{g1,P}}| - |\Delta P_{\mathrm{g2,P}}|) & , \quad \frac{dP_{\mathrm{g12}}}{dt} < 0 \end{cases} \tag{6.15}$$

6.4 Stability analysis of system model

The mathematical model of the two machine system with the E-STATCOM in Fig. 6.2 is developed in this section to study the impact of active and reactive power injection on power oscillation damping. Each generator will be represented by the classical model as described in Section 6.2. The E-STATCOM is modeled as a controlled ideal current source with injected currents controlled as in (6.16) - (6.17) according to the design in Section 6.3.1. The constant K_{P} is given by (6.18).

$$i_{\mathrm{f}}^{\mathrm{q}} = G_{\mathrm{Q}}\frac{d\Delta P_{\mathrm{g12}}}{dt} \approx G_{\mathrm{Q}}\left\{\frac{V_{\mathrm{g1}}V_{\mathrm{g2}}\cos(\delta_{\mathrm{g10}} - \delta_{\mathrm{g20}})}{X_1 + X_2}\right\}\omega_{\mathrm{g0}}\left[\Delta\omega_{\mathrm{g1}} - \Delta\omega_{\mathrm{g2}}\right] \tag{6.16}$$

$$i_{\mathrm{f}}^{\mathrm{d}} = G_{\mathrm{P}}\frac{d\Delta\theta_{\mathrm{g}}}{dt} \approx G_{\mathrm{P}}\omega_{\mathrm{g0}}\left\{K_{\mathrm{P}}\Delta\omega_{\mathrm{g1}} + (1 - K_{\mathrm{P}})\Delta\omega_{\mathrm{g2}}\right\} \tag{6.17}$$

$$K_{\mathrm{P}} = \left\{\frac{\left[(1-a)V_{\mathrm{g1}}\right]^2 + a(1-a)V_{\mathrm{g1}}V_{\mathrm{g2}}\cos(\delta_{\mathrm{g10}} - \delta_{\mathrm{g20}})}{E_{\mathrm{g0}}^2}\right\} \tag{6.18}$$

Linearizing around an initial operating point and using the speed variation of each generator ($\Delta\omega_{\mathrm{g1}}$, $\Delta\omega_{\mathrm{g2}}$) and the rotor angle difference between the generators ($\Delta\delta_{\mathrm{g12}} = \Delta\delta_{\mathrm{g1}} - \Delta\delta_{\mathrm{g2}}$) as state variables, the small signal dynamic model of the two machine system with the E-STATCOM in per unit is developed as in (6.19). No infinite bus is included in this model and this results in the absence of absolute speed reference for the generator speed variations. Therefore, the resulting 3^{rd} order system always contains one common mode pole in the response of the generator's speed and rotor angle variation [24]. ΔT_{g1} and ΔT_{g2} represent the change in mechanical torque inputs of the first and second generator, respectively, while $H_{\mathrm{g1}}/H_{\mathrm{g2}}$ is the inertia constant of the corresponding generators in second. Assuming no mechanical damping and that the system is initially in steady state with the generator speeds equal to $\omega_{\mathrm{g10}} = \omega_{\mathrm{g20}} = \omega_{\mathrm{g0}}$, the constants are derived as in (6.20) where K_{Q} is given by (6.21).

$$\frac{d}{dt}\begin{bmatrix} \Delta\omega_{\mathrm{g1}} \\ \Delta\delta_{\mathrm{g12}} \\ \Delta\omega_{\mathrm{g2}} \end{bmatrix} = \begin{bmatrix} a_{11} & a_{12} & a_{13} \\ \omega_{\mathrm{g0}} & 0 & -\omega_{\mathrm{g0}} \\ a_{31} & a_{32} & a_{33} \end{bmatrix}\begin{bmatrix} \Delta\omega_{\mathrm{g1}} \\ \Delta\delta_{\mathrm{g12}} \\ \Delta\omega_{\mathrm{g2}} \end{bmatrix} + \begin{bmatrix} 1/2H_{\mathrm{g1}} & 0 \\ 0 & 0 \\ 0 & 1/2H_{\mathrm{g2}} \end{bmatrix}\begin{bmatrix} \Delta T_{\mathrm{g1}} \\ \Delta T_{\mathrm{g2}} \end{bmatrix} \tag{6.19}$$

$$\begin{bmatrix} a_{11} & a_{31} \\ a_{12} & a_{32} \\ a_{13} & a_{33} \end{bmatrix} = \begin{bmatrix} \frac{\omega_{g0}(G_P E_{g0} K_P^2 + G_Q K_Q)}{2H_{g1}} & \frac{\omega_{g0}(G_P E_{g0} K_P (1-K_P) - G_Q K_Q)}{2H_{g2}} \\ -\frac{V_{g1} V_{g2} \cos(\delta_{g10} - \delta_{g20})}{2H_{g1}(X_1+X_2)} & \frac{V_{g1} V_{g2} \cos(\delta_{g10} - \delta_{g20})}{2H_{g2}(X_1+X_2)} \\ \frac{\omega_{g0}(G_P E_{g0} K_P (1-K_P) - G_Q K_Q)}{2H_{g1}} & \frac{\omega_{g0}(G_P E_{g0} (1-K_P)^2 + G_Q K_Q)}{2H_{g2}} \end{bmatrix} \tag{6.20}$$

$$K_Q = \frac{[V_{g1} V_{g2}]^2 \sin\left(2(\delta_{g10} - \delta_{g20})\right) a(1-a)}{2E_{g0}(X_1 + X_2)} \tag{6.21}$$

The terms a_{12} and a_{32} represent the synchronizing torque coefficients resulting from the selected operating point and the contribution of the E-STATCOM is zero. The terms a_{11} and a_{33} determine the damping torque coefficient provided by the E-STATCOM with respect to the change in speed of the respective generator. The contribution from the active and reactive power injection is shown separately with the gains G_P and G_Q. To provide positive damping for the two generators a_{11} and a_{33} should be negative. For this, the sign of G_P should be negative and the sign of G_Q should be chosen based on the sign of K_Q, which depends on the direction of transmitted power. For a transmitted power from the first to the second generator as the case in this analysis, K_Q will be positive and the sign of G_Q should be negative. For a transmitted power in the other direction, the sign of G_Q should be reversed. The terms a_{13} and a_{31} are the cross coupling terms between the two generator speed variations. With active power injection only ($G_Q = 0$), the cross coupling terms reduce the damping as the speed variation of the two generators will be opposite for a power transfer between them. At the point where damping by active power injection is zero, injected active power is also zero. At either end of the generators, K_P is maximum and at the same time minimize the cross coupling terms. This increases the damping provided by active power injection as the E-STATCOM is closer to the generators. In the case of reactive power injection only ($G_P = 0$), positive damping is provided by the cross coupling terms and maximum damping is provided at the middle of the line ($a = 0.5$) where K_Q magnitude is maximum. Observe that, as it can be understood from (6.20), this is valid under the assumption of a perfectly symmetrical system around the midpoint of the line.

For the analysis in this section, a hypothetical simplified two area power system model as shown in Fig. 6.5 similar to the one in Fig. 6.1 is used. The system represents a 20/230 kV transmission line with base apparent power $S_b = 900$ MVA. The reactance of line sections is shown in pu. The leakage reactance of the transformers and transient impedance of the generators is 0.15 pu and 0.3 pu respectively. The inertia constant of the first generator $H_{g1} = 6.5$ s. The E-STATCOM is connected along the transmission line and its location is shown by the value of a.

6.4.1 Example case for a two machine system

The inertia constant of the second generator is chosen as $H_{g2} = H_{g1}$ for analysis in this section. Figure 6.6 shows the movement of poles of the system in Fig. 6.5 as the position of E-STATCOM is changed. To make the analysis more realistic, it is here assumed that the internal

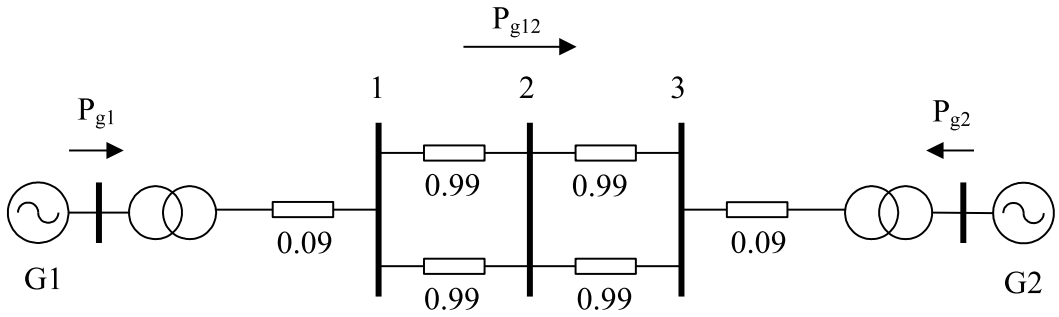

Fig. 6.5 Simplified two area power system model for simulation.

bus voltage of the two generators G1 and G2 are not equal. In this case, the electrical midpoint of the line will not coincide with the physical midpoint ($a = 0.5$). With the described control strategy, injected active power is zero at the point where the effect of active power injection on damping is zero. This is close to the electrical midpoint of the line. On the other hand, damping by reactive power injection is maximum. The reverse happens at either end of the generators. It is also possible to see from Fig. 6.6 that a more uniform damping along the line is obtained by using injection of both active and reactive power. Observe that, due to the asymmetry in the simulated system, the obtained damping profile is not symmetrical around $a = 0.5$.

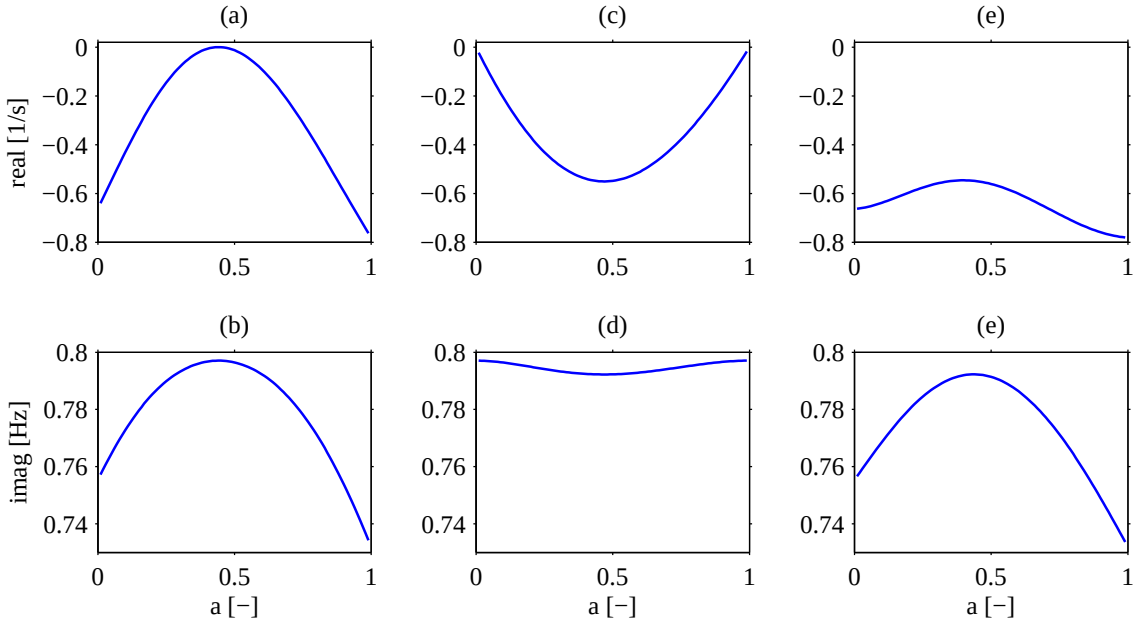

Fig. 6.6 Real and imaginary part of the complex conjugate poles vs. position; (a, b) active power injection, (c, d) reactive power injection and (e, f) active and reactive power injection. [$G_{\mathrm{P}} = 0.1$, $G_{\mathrm{Q}} = 0.2$, $P_{\mathrm{g12}} = 0.444$ pu].

Similarly, the movement of poles with a change in gain of the POD controller is shown in Fig. 6.7. G_{P} and G_{Q} are both varied between 0 and 1 in steps of 0.01. The E-STATCOM is

connected at bus 1 and bus 2 in Fig. 6.5 for active and reactive power injection respectively. There is a maximum gain in case of active power injection where maximum damping is provided for the oscillatory mode poles. When the gain is increased further, the effect is more on the common mode pole. For reactive power injection, damping increases linearly with the gain. For reactive power injection, the damping provided to the common mode poles is zero as the speed variation of the generators is used in (6.16). The choice of G_{P} and G_{Q} depends on the level of damping required and rating of the converter. With respect to G_{P}, the maximum value is a function of the available energy storage size whereas the maximum value of G_{Q} is a function of the maximum PCC voltage variation allowed.

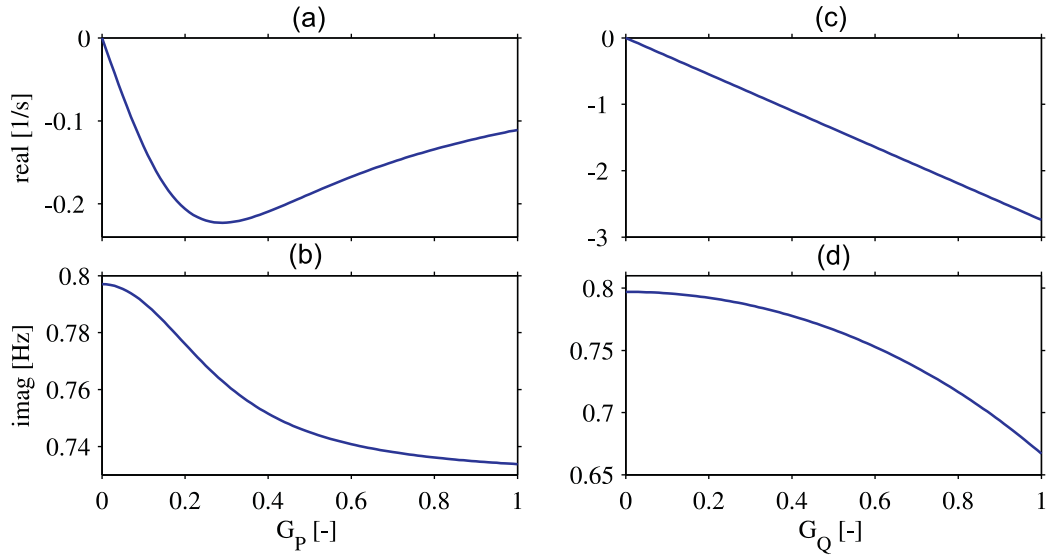

Fig. 6.7 Movement of poles vs. gains; (a, b) active power injection and (c, d) reactive power injection; [$P_{\mathrm{g12}} = 0.444$ pu].

6.4.2 Single machine infinite bus system

A single machine infinite bus system is a special case of two machine system with $H_{\mathrm{g2}} = \infty$ ($\Delta\omega_{\mathrm{g2}} = 0$). Figure 6.8 shows the effect of E-STATCOM on damping at different locations for different transmitted active powers.

As the results show, damping by reactive power is effective at the middle of the line and damping by active power is effective at the generator 1 terminal. No damping can of course be provided by active or reactive power injection at the infinite bus (generator 2 terminal). Moreover, the amount of transmitted power highly affects damping by reactive power injection. But, it has more or less no impact on damping by active power injection.

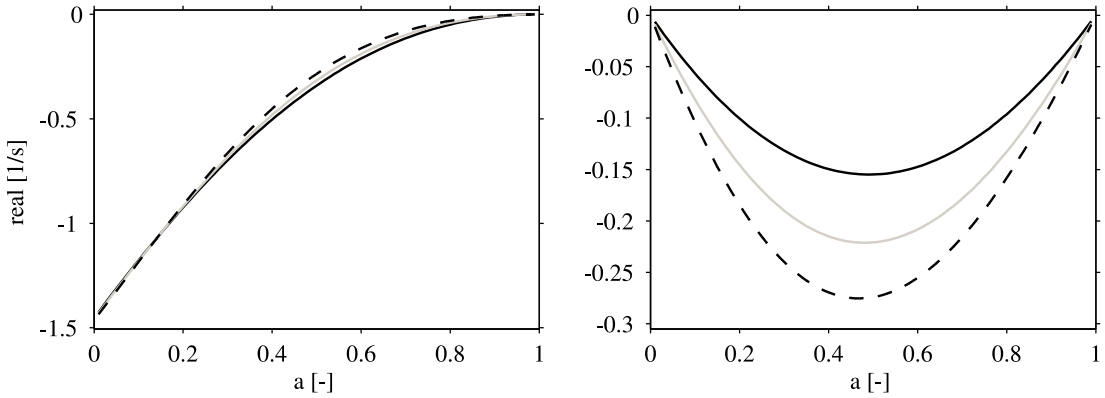

Fig. 6.8 Movement of real part of the poles for a one machine infinite bus system with position of E-STATCOM for three transmitted power P_{g12} values. Dashed: $P_{\mathrm{g12}} = 0.444$ pu, Gray: $P_{\mathrm{g12}} = 0.333$ pu, Black solid: $P_{\mathrm{g12}} = 0.222$ pu. Left: active power injection for POD with $G_{\mathrm{P}} = 0.1$, Right: reactive power injection with $G_{\mathrm{Q}} = 0.2$.

6.5 Simulation verification

In this section the POD and TSE controllers described in Section 6.3 will be verified though simulation. For this, the two machine system in Fig. 6.5 will be considered.

A simplified aggregate model of a power system transferring power from one area to the other has been used to describe the principle of power oscillation damping and transient stability enhancement by active and reactive power injection. This simplified model helps to evaluate the performance of the E-STATCOM without the influence of other power system components such as loads. Therefore, the two area power system model in Fig. 6.5 is simulated in PSCAD/EMTDC with the described control strategy in Section 6.3. For analysis purposes, a three-phase fault is applied to the system at bus 3 at t = 1 s and the fault is cleared after 80 ms. The two generators are assumed to have the same inertia constant $H_{\mathrm{g1}} = H_{\mathrm{g2}} = 6.5\ s$. The initial steady state transmitted power P_{g12} is set to 0.444 pu. Due to the applied disturbance, a poorly damped stable oscillation is obtained after the fault clearing.

Figure 6.9 shows the estimate of the control input signals for POD, while the performance of the E-STATCOM following the fault at three different locations is shown in Fig. 6.10. As described in the small signal analysis in Section 6.4, the injected active power is minimum at the electrical midpoint of the line ($H_{\mathrm{g1}} = H_{\mathrm{g2}}$). This is the minimum point to provide POD action by active power injection. The control algorithm therefore minimizes injection of active power at this location (bus 2 in this case) as shown in Fig. 6.11. When moving away from the electrical midpoint, active power injection increases and so does its effect to provide damping. In such a way, the use of active power can be optimized. With respect to reactive power injection, the level of damping decreases when moving away from the electrical midpoint. As the transmitted power P_{g12} is used to control reactive power, the same amount of injected reactive power is used at the three locations and maximum damping action is provided at the electrical midpoint of the line unlike the active power injection. With both active and reactive power injection, effective power oscillation damping is provided by the E-STATCOM irrespective of its location in the

line. The gain for active power injection G_{P} is selected to achieve maximum damping at bus 1 according to the small signal analysis in Section 6.4.1 and shown in Fig.6.7 (left). The gain for reactive power injection G_{Q} is then set the same for all the tests in Fig. 6.10 and 6.11. Due to the unlimited PCC voltage modulation, both active and reactive power injection provide similar damping at bus 1 and bus 3.

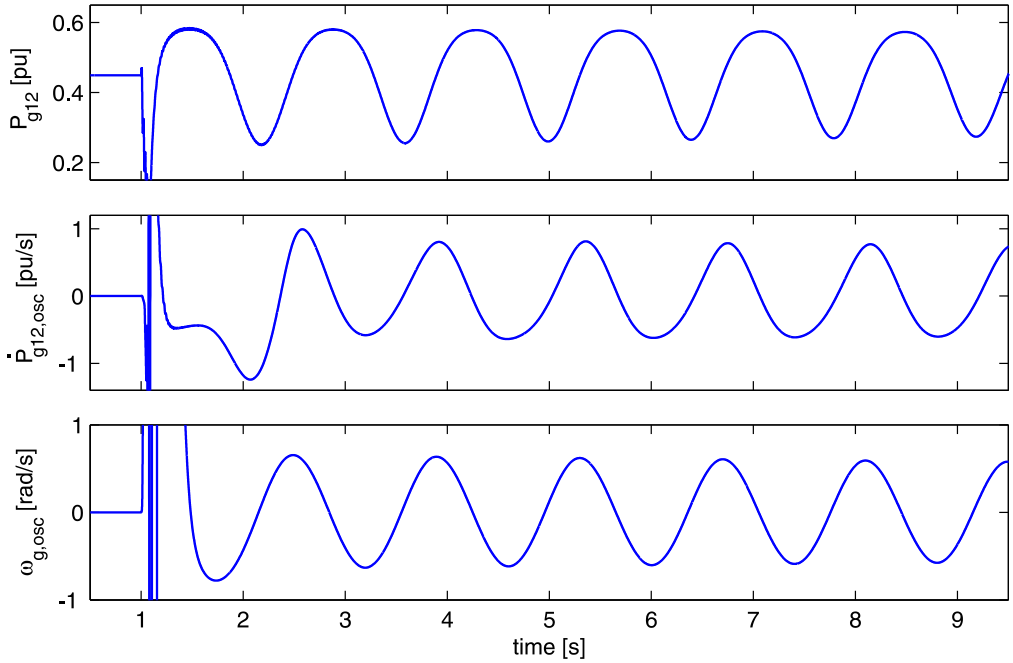

Fig. 6.9 Transmitted power (top) and estimated control input signal for POD at bus 1 with Q_{inj} (middle) and with P_{inj}) (bottom).

Depending on the steady state transmitted power, level of fault and location of the E-STATCOM, the amount of active power injection required to provide a certain amount of damping varies greatly. Figure 6.12 shows power oscillation damping with two active power injection levels at bus 1. With more active power injection, the level of damping increases. Of course, the effect would have been negligible with the E-STATCOM connected at bus 2.

Even if reactive power injection is effective closer to the electrical midpoint of the line, the PCC voltage E_{g} is highly affected as shown in Fig. 6.13. The possibility of having active power injection both reduce the maximum PCC voltage swing and provide more damping action except when the E-STATCOM is close to mass-scaled electrical midpoint of the line.

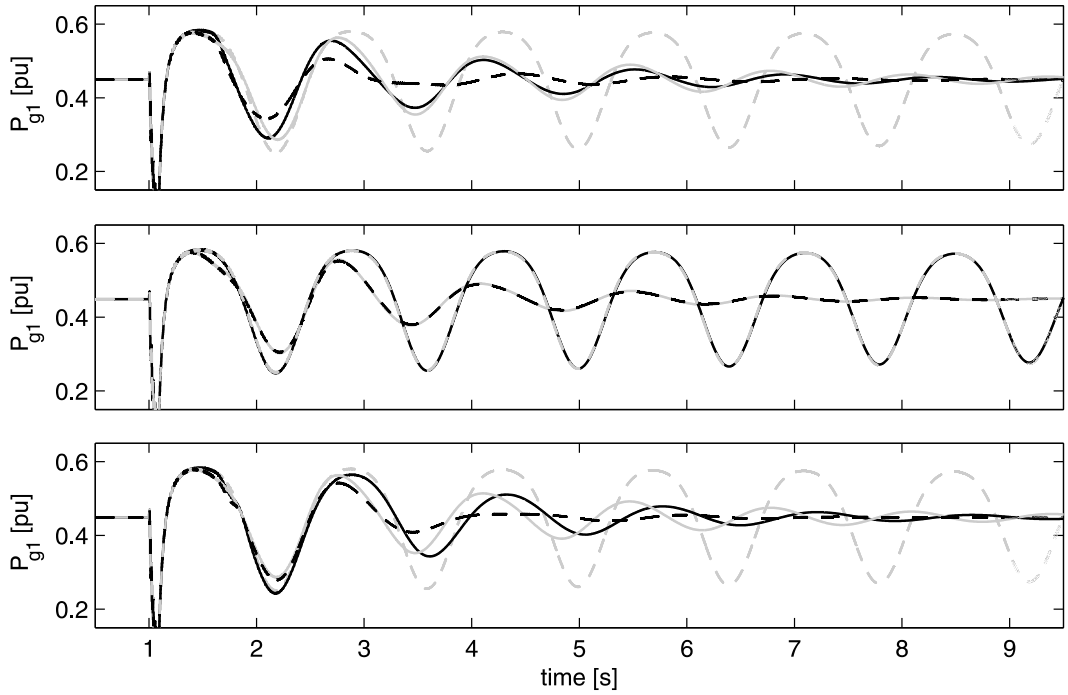

Fig. 6.10 Generator 1 active power output following a three phase fault with E-STATCOM connected at bus 1 (top), bus 2 (middle) and bus 3 (bottom). POD by $P_{\rm inj}$ only (black solid), $Q_{\rm inj}$ only (gray solid), both $P_{\rm inj}$ and $Q_{\rm inj}$ (black dashed) and no POD (gray dashed); [$G_{\rm P} = G_{\rm Q} = 0.3$].

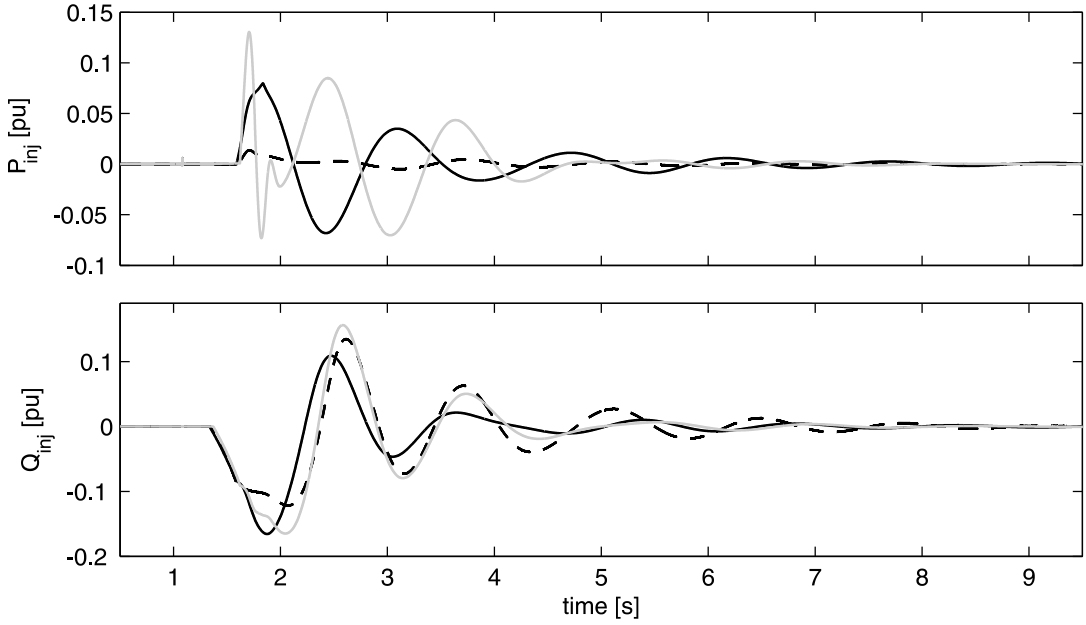

Fig. 6.11 Injected active and reactive power with E-STATCOM connected at bus 1 (black solid), bus 2 (black dashed) and bus 3 (gray solid). Active power injection (top); reactive power injection (bottom); both $P_{\rm inj}$ and $Q_{\rm inj}$ used for POD ; [$G_{\rm P} = G_{\rm Q} = 0.3$].

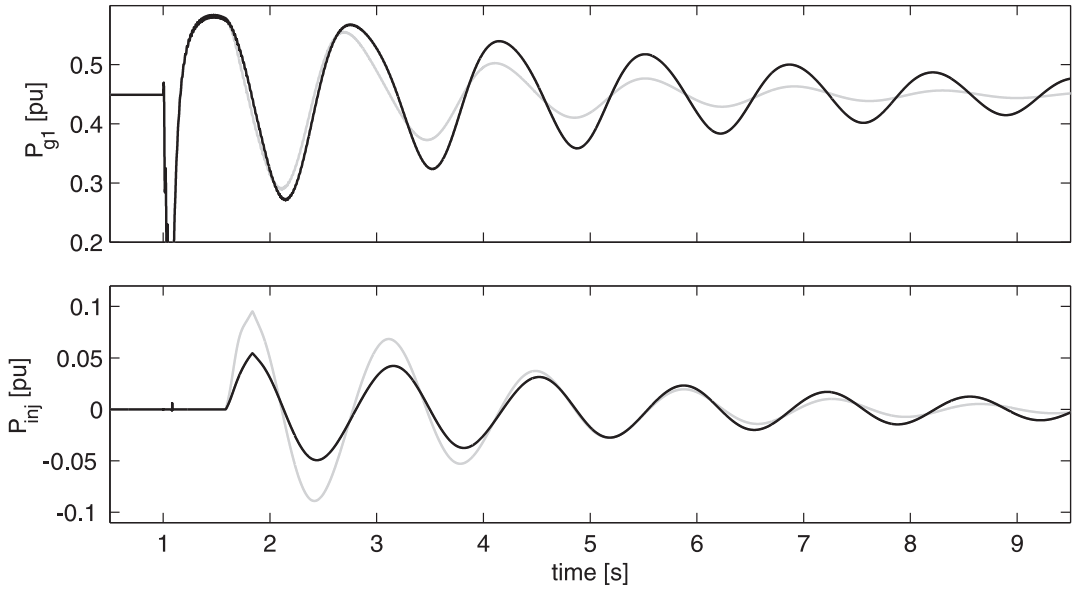

Fig. 6.12 POD by P_{inj} at bus 1; top: generator 1 active power, bottom: injected active power; G_{P} = 0.15 (black), 0.3 (gray).

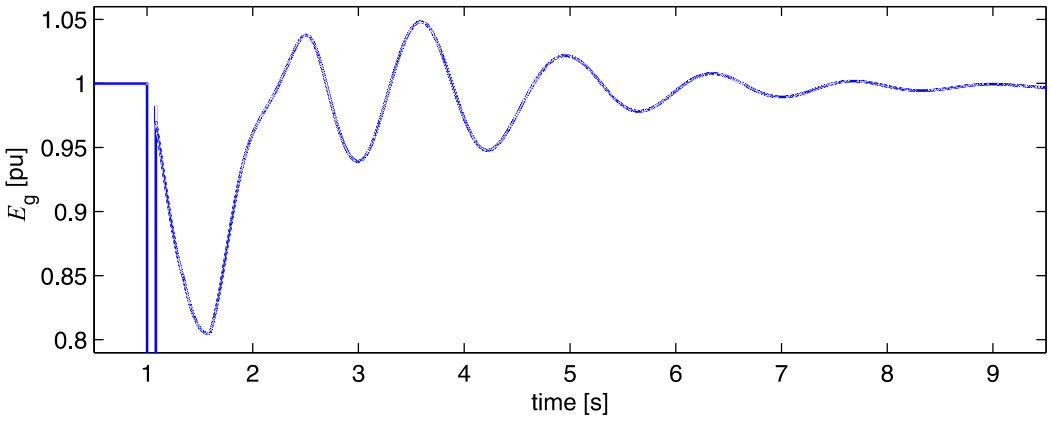

Fig. 6.13 PCC voltage at bus 2 when only Q_{inj} used for POD.

The simulation results shown so far, have been carried out under the assumption of accurate knowledge of the oscillatory frequency in the transmitted active power. As mentioned in Section 4.3.2, the improved RLS algorithm used in this work is frequency adaptive. To test the dynamic performance of the implemented controller with uncertainties in system parameters, a simulation is performed assuming inaccurate knowledge of the electromechanical oscillation frequency. Figure 6.14 shows the obtained simulation results when an error of 25% in the estimated oscillatory frequency is considered. The compensator is connected at bus 2 (see Fig. 6.5), thus POD will be achieved mainly by reactive power injection. The figure shows the dynamic performance of the system with the frequency adaptation algorithm (black curve). To highlight the effectiveness of the implemented adaptation algorithm, the active power waveform that would be obtained with accurate knowledge of the frequency is also shown in the figure (solid gray curve). Observe that for the two cases, the dynamic performance of the system when damping a power oscillation is almost identical.

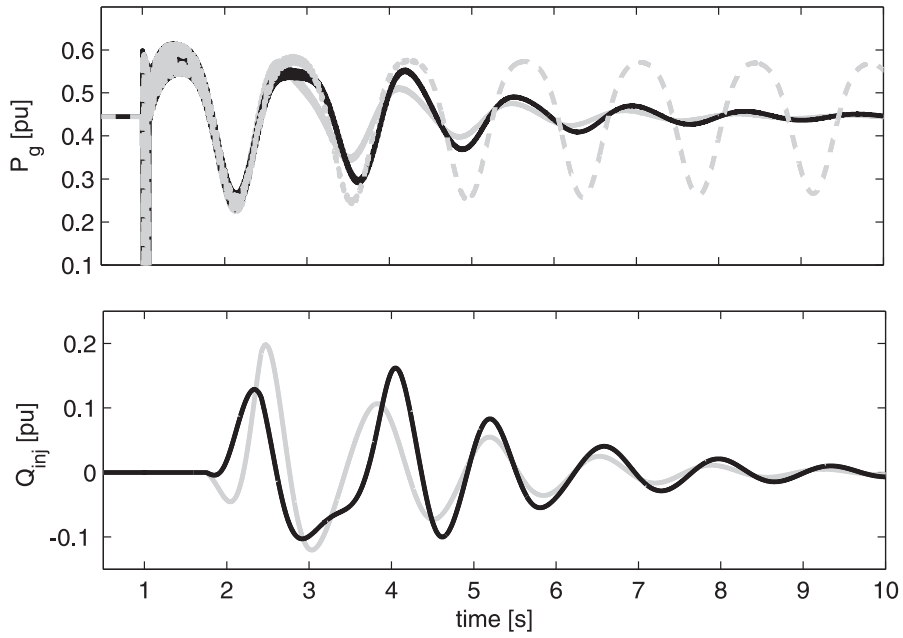

Fig. 6.14 Power oscillation damping with E-STATCOM connected at bus 2. Top: generator active power; bottom: injected reactive power. Gray dashed curve: no POD controller; gray solid curve: POD controller activated with accurate knowledge of the oscillation frequency; black solid curve: POD controller activated and 25% error in the assumed oscillation frequency.

The simulation is repeated for a longer fault clearing time of 150 ms to test the transient stability enhancement function. The longer fault clearing time results in loss of synchronism and a subsequent collapse of the system as shown in Fig. 6.15 (top). In this case, the E-STATCOM is connected at bus 1 and a transient stability enhancement function is achieved by absorbing a constant active power or controlling the PCC voltage to 1 pu. As shown in the the figure, the the stability of the system is maintained.

Even if the TSE function keeps the stability of the system, the POD function should also be used to provide damping to the system. Figure 6.16 shows the performance of TSE and POD controllers together. Immediately after fault clearing, the TSE function starts followed by the

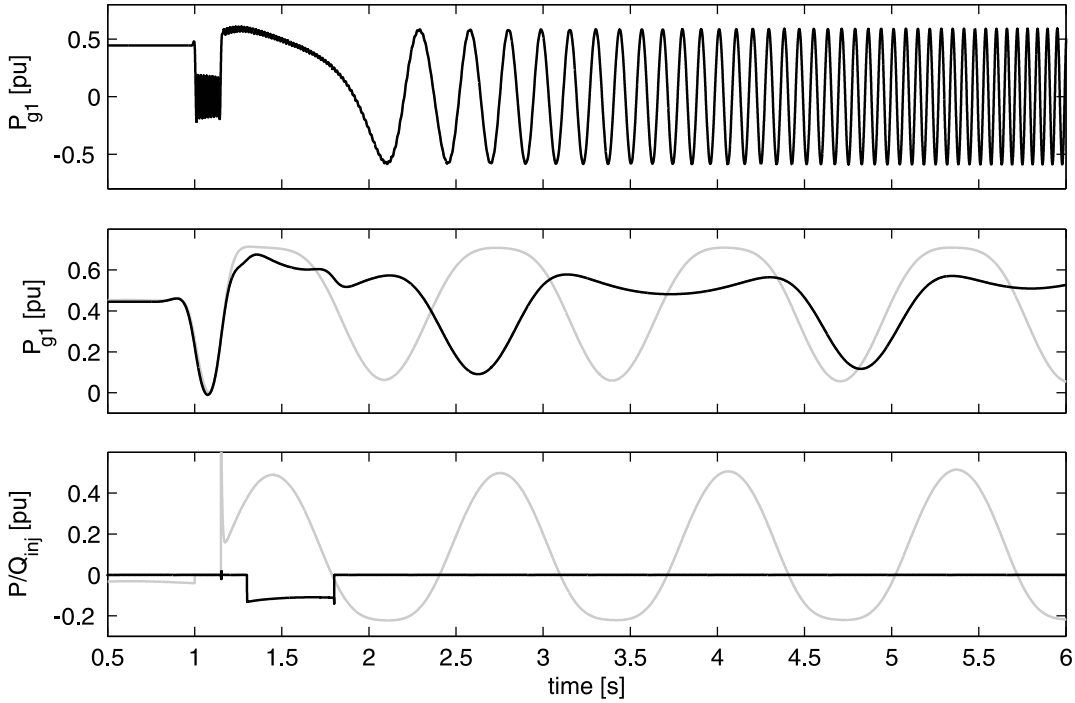

Fig. 6.15 Transient stability enhancement with E-STATCOM connected at bus 1. Top: no TSE, Middle: TSE by P_{inj} (black) and TSE by Q_{inj} (gray); Bottom: P_{inj} for TSE (black) and Q_{inj} for TSE (gray).

POD function after the first swing of the generator angles. In this example, the TSE function is provided by keeping the PCC voltage E_{g} to 1 pu all the time. Two cases are compared in this simulation. In one case, the reactive power is used for controlling the PCC voltage and to provide damping. When damping is provided by reactive power injection, the PCC voltage is shown to oscillate around the nominal voltage. In the second case, the PCC voltage is kept constant and POD is provided by active power injection. The advantage with active power injection for POD is that the PCC voltage is not affected as shown in Fig. 6.16 (bottom black curve).

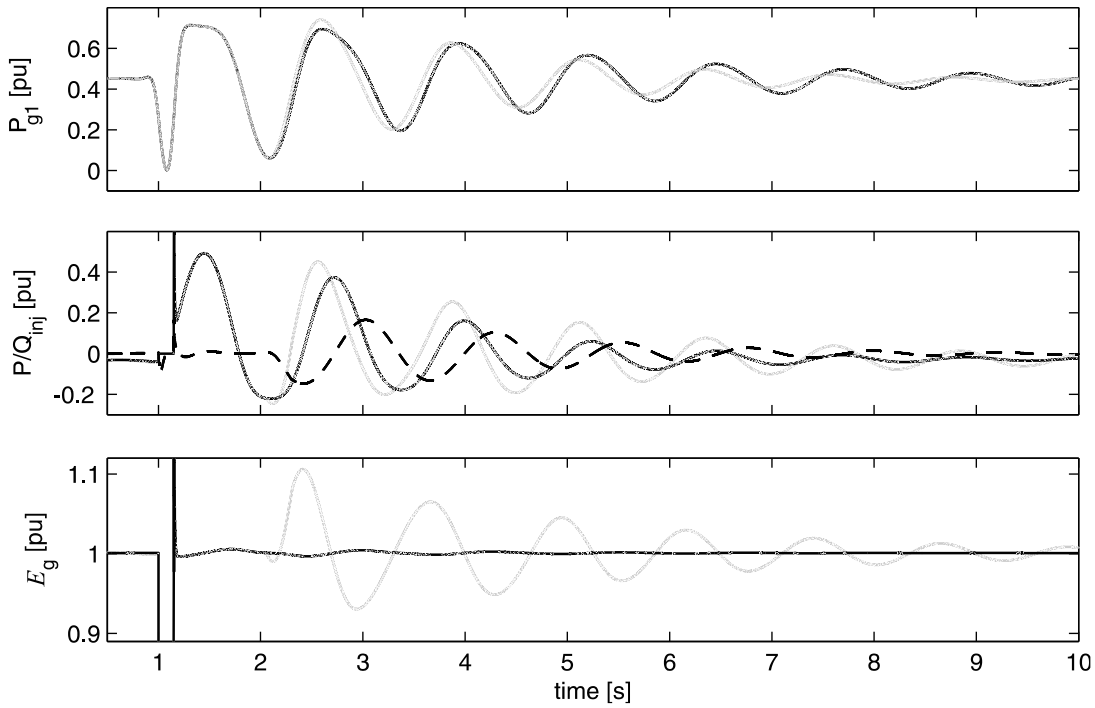

Fig. 6.16 Transient stability enhancement and power oscillation damping with E-STATCOM connected at bus 1. Top: generator 1 power with Q_{inj} for TSE and POD (gray), Q_{inj} for TSE and P_{inj} for POD (black); Middle: Q_{inj} for TSE and POD (gray), Q_{inj} for TSE (black) and P_{inj} for POD (dashed); Bottom: PCC voltage magnitude with Q_{inj} for TSE and POD (gray), Q_{inj} for TSE and P_{inj} for POD (black).

6.6 Conclusions

In this chapter, control of E-STATCOM for power system stability enhancement is shown using a simplified two machine power system model. The control input signals for active and reactive power injection are derived using the signal estimation technique described in Chapter 4. The robustness of the control algorithm against system parameter uncertainties has been investigated through simulation. By using the frequency estimate of the Phase Locked Loop (PLL) to control injection of active power for POD, injection of active power is minimized at locations in the power system where its effect is negligible. When both active and reactive power injection for POD and TSE is used with the control strategy as described, it is shown that stability enhancement can be achieved at different connection points of the E-STATCOM in the transmission line.

Chapter 7

Experimental Verification

7.1 Introduction

To validate the results obtained via simulation for improved RLS based estimator, control of shunt-connected E-STATCOM and power system stability enhancement by E-STATCOM, experimental tests have been performed in the Power System Laboratory at the Department of Energy and Environment at Chalmers University of Technology. In this chapter, a description of the laboratory setup will be shown and experimental results will be presented.

7.2 Laboratory setup

To perform the various tests, the laboratory setup in Fig. 7.1, which represents a single line diagram of the actual setup has been used. A photo of the actual laboratory setup is shown in Fig. 7.2. The setup consists of a synchronous generator connected to a stiff AC grid through a transmission line model and a VSC system connected at various location in the transmission line. These components will be described in this section.

7.2.1 VSC system

The VSC system consists of a two-level converter connected to the transmission line model though an L-filter. The parameters of the VSC system are given in Table 7.1. The VSC is controlled from a computer with a dSpace 1103 board [53] which can be programmed using C-code or Matlab/Simulink. Using the dSpace software ”Control Desk”, a real-time management of the inputs and outputs during the experiment is possible. The DC-link of the VSC is connected to a DC machine rated 700 V and 60 A. The DC machine is equipped with field control and the terminal DC voltage is controlled to 650 V for all experiments. The DC machine will act as the energy storage (infinite storage is here assumed) providing active power injection capability to the VSC. Therefore, the VSC with the DC machine can be considered as an E-STATCOM.

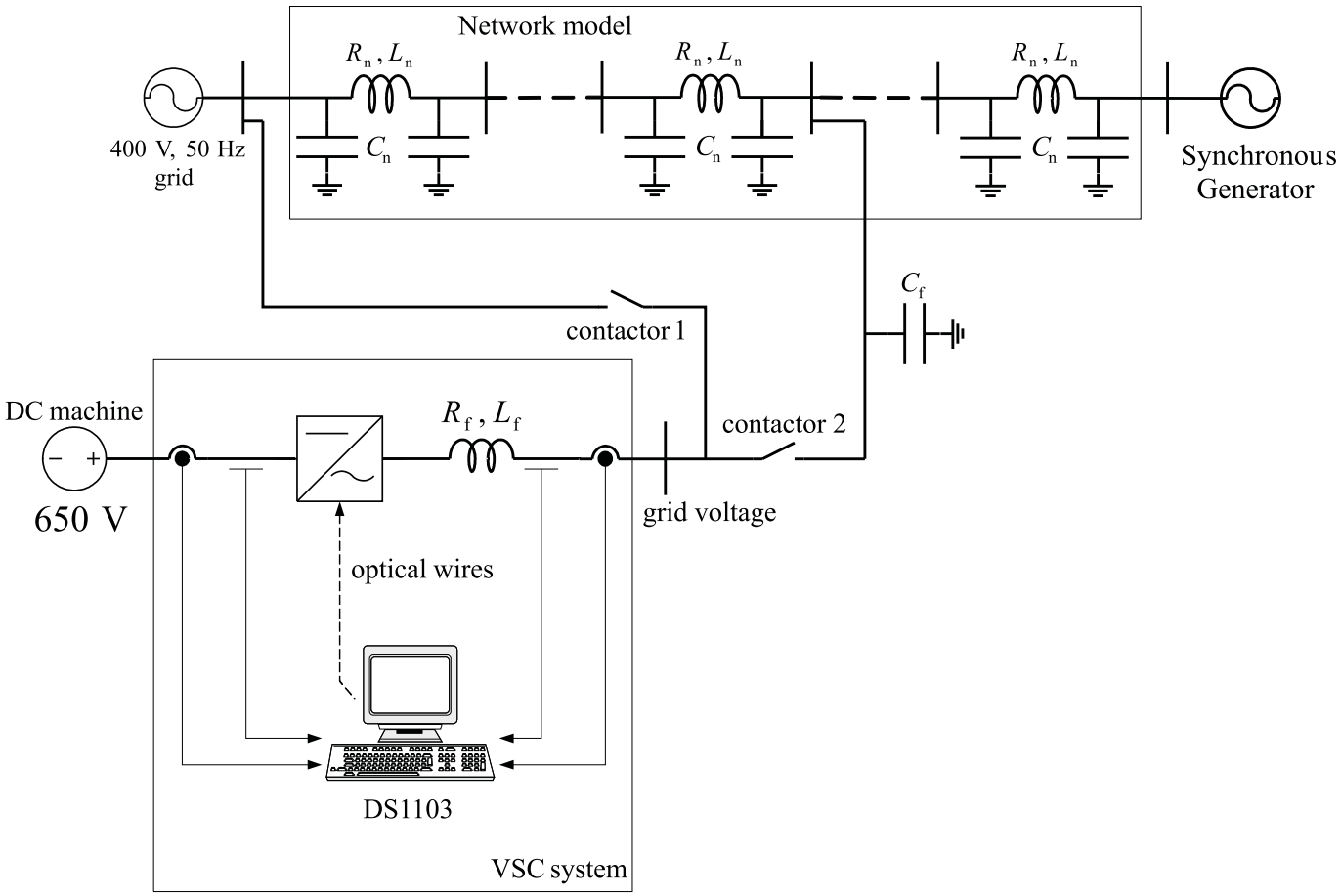

Fig. 7.1 Single line diagram of the laboratory setup.

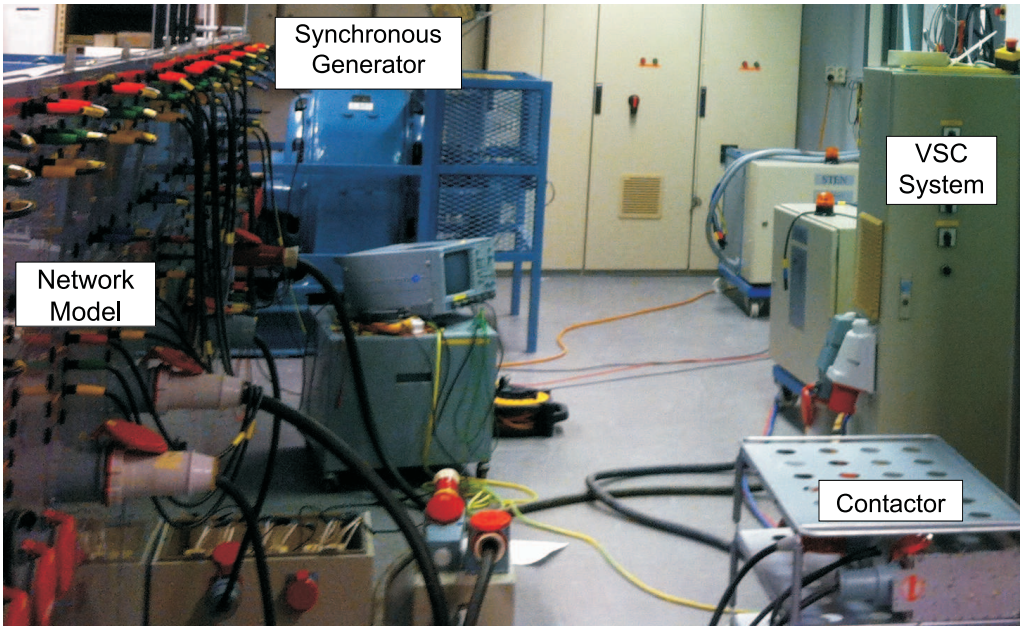

Fig. 7.2 Photo of the laboratory setup.

TABLE 7.1. PARAMETERS OF THE VSC SYSTEM

Rated power	202.1 kVA
Rated voltage	550 V
Rated current	212 A
DC-link capacitor	2.2 mF
Filter inductance, L_{f}	2 mH
Filter resistance, R_{f}	6.2 mΩ
Filter capacitance, C_{f}	152 mF

7.2.2 Network model

The network model is a scaled version of a Swedish 400 kV transmission system with the entire model working at 400 V. The transmission line model consists of six identical Π sections (with parameters L_{n} = 2.05 mH, R_{n} = 0.05 Ω and C_{n} = 46 uF), each corresponding to a portion of 150 km of the actual line (with parameters L_{n} = 0.160 H, R_{n} = 4.17 Ω and C_{n} = 0.065767 uF) at 400 kV [54]. Each Π section can be connected in series or parallel. All the six Π sections (without the shunt capacitors, C_{n}) connected in series have been used for all the experiments.

7.2.3 Synchronous generator

A picture of the generator system, which represents an accurate model of the large Harsprånget hydro power plant, situated by the Lule river in northern Sweden, is shown in Fig. 7.3. Parameters of the synchronous generator are given in Table 7.2. The synchronous generator is driven by an 85 kW DC motor. The DC motor is fed from a Thyristor converter and can be controlled by either speed or armature current, corresponding to frequency or active power control of the generator. The large flywheel on the shaft between the DC motor and the generator gives the model similar mechanical behavior as the real power plant. The generator is equipped with a modern microprocessor-based voltage regulator that can control the generator terminal voltage, field current, reactive power or power factor. To enhance angular stability, a power system stabilizer (PSS) is also included in the voltage controller [54]. The PSS together with the speed controller from the DC motor gives the generator system a damped stable system following faults during transient stability studies. For the purpose of this experiment, the speed controller of the DC motor is detuned and the PSS is disabled. This results in a poorly damped low-frequency electromechanical oscillation following short circuit faults so that the performance of the E-STATCOM can be better evaluated. For all the test performed, the ratings of the synchronous generator (75 kVA, 400 V) are used as base values.

7.3 Experimental results on improved RLS based estimator

To verify the improved RLS based estimator experimentally, the the network model without the E-STATCOM connected (contractor 1 and 2 open in Fig. 7.1) has been used. A three-phase

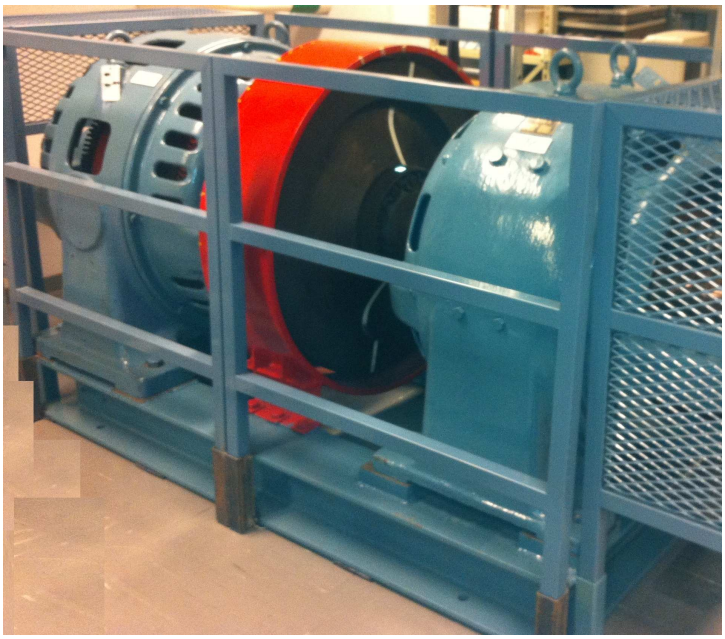

Fig. 7.3 Photo of the generator system comprising of the synchronous generator to the left end, the DC motor to the right end and the flywheel in between.

TABLE 7.2. PARAMETERS OF THE SYNCHRONOUS GENERATOR

Rated power	75 kVA
Rated voltage	400 V
Rated current	108.3 A
Synchronous reactance, X_{d}	2.93 Ω
Unsaturated transient reactance, X'_{d}	0.437 Ω
Unsaturated sub transient reactance, X''_{d}	0.332 Ω
Armature resistance, R_{s}	0.081 Ω
Inertia constant (generator-turbine set), H_{g}	5.56 s

fault has been applied in the middle of the transmission line with a fault clearing time of 250 ms. The measured active power out from the generator $p(t)$ is then used as an input to estimate the low-frequency electromechanical oscillation component that occurs in the transmitted power following the fault. The estimator is started with an initial assumed oscillation frequency of 0.60 Hz while the true value in the measured signal is close to 0.42 Hz. This low oscillation frequency highlights the importance of the adopted method, since the classical approaches (using low-pass filters or lead-lag filter links, see Fig. 4.3 and Fig. 3.6) would require low bandwidth, resulting in a reduction in the estimation speed.

Figure 7.4 shows the dynamic performance of the estimator. The parameters used for the improved RLS are those discussed in Chapter 4. As the result in Fig. 7.4 (bottom) shows, the estimation is instantaneous immediately after fault clearing. The fast transient estimation is followed by the steady state estimation where the oscillation frequency is updated using the controller described in Section 4.3.2. This corrects the oscillation in the estimate of the average component and any phase error in the estimate of the oscillatory component that could have

existed due to wrong assumption of the oscillation frequency. Figure 7.5 shows the variation of the forgetting factor λ following the rapid change in the input with the frequency adaptation to track the true oscillation frequency ω_{osc}.

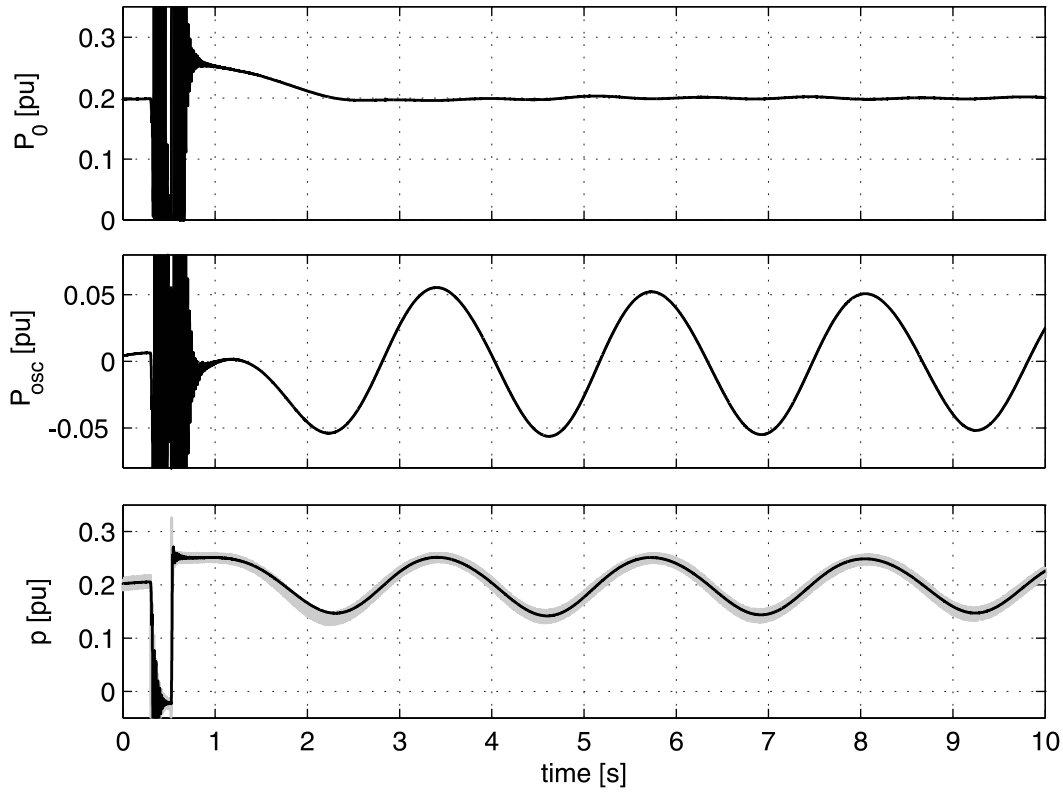

Fig. 7.4 Estimate for the average and oscillatory component. Top: Estimated average component; Middle: Estimated oscillatory component; Bottom: Measured power signal (gray), estimated signal (black). 50% error in initial assumed oscillation frequency.

Similarly, to verify the improved RLS based estimator for estimation of sequence and harmonic components, a three phase voltage that contains around 0.02 pu slowly varying 5^{th} and 7^{th} order harmonics is measured at the middle of the transmission line. From the measured grid voltage, an unbalanced voltage dip is applied inside the control computer and the performance of the estimator to extract the sequence and harmonic components is shown in Fig. 7.6. In the same figure, the fast and accurate estimation of the sequence and harmonic components can be easily seen from the estimates of the phasors, which converge to constant values in steady state.

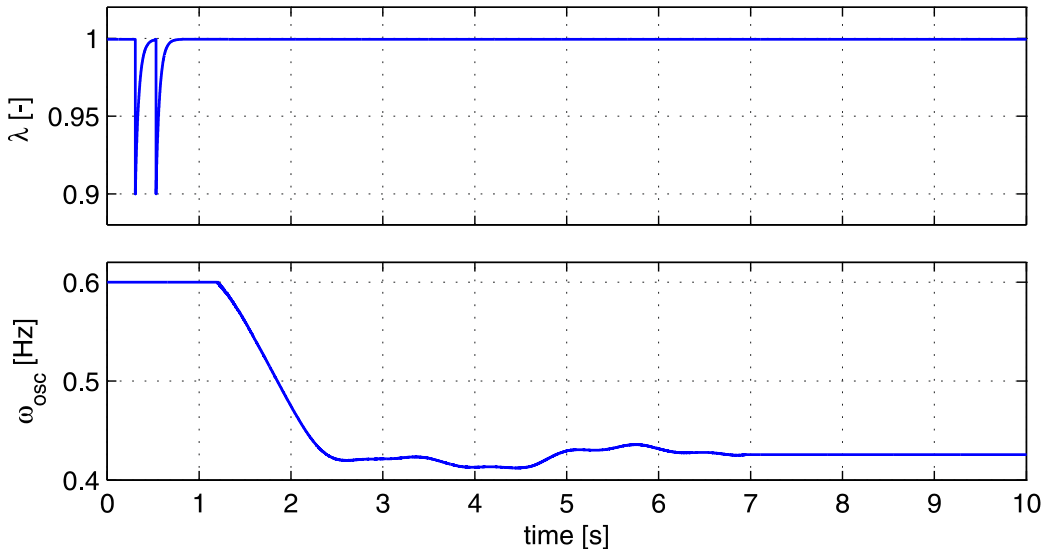

Fig. 7.5 Improved RLS based estimator; Variation of forgetting factor λ (top) and estimate of oscillation frequency $\tilde{\omega}_{\text{osc}}$ (bottom).

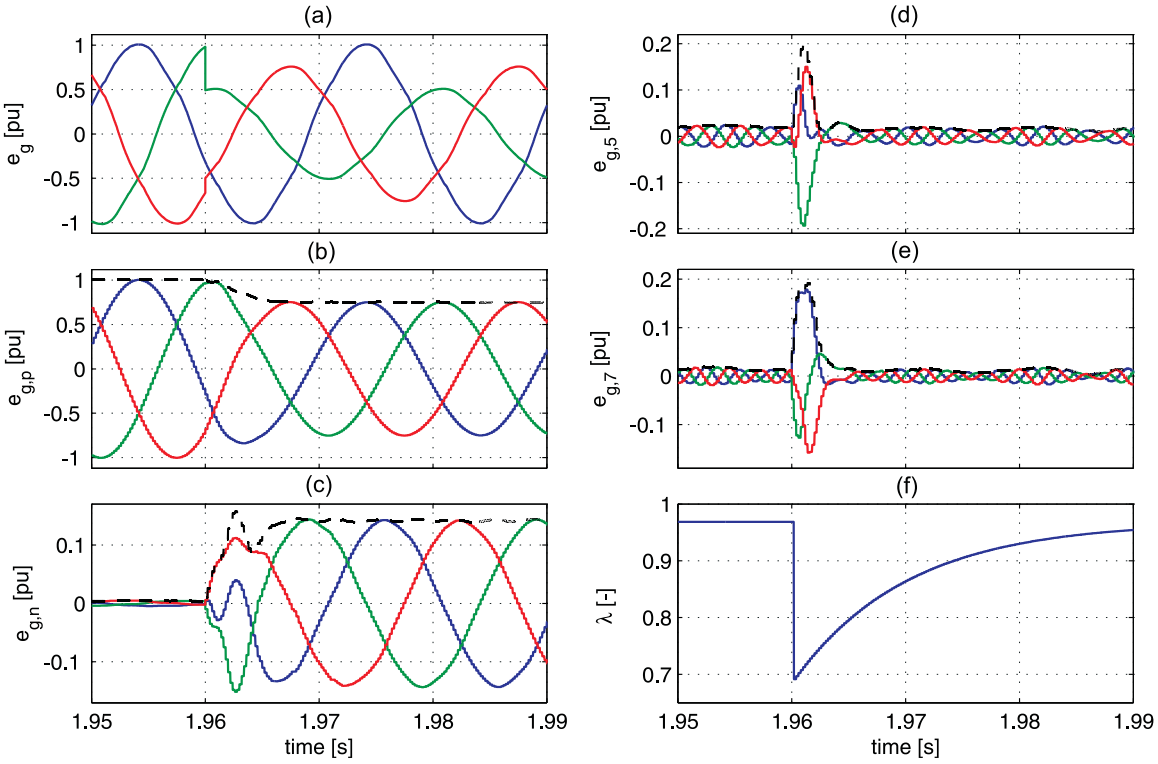

Fig. 7.6 Sequence and harmonic estimation in three phase system. (a) Grid voltage, (b) Positive sequence fundamental component, (c) 50 Hz Negative sequence component, (d) Negative sequence 5^{th} order harmonic component,(e) Positive sequence 7^{th} order harmonic component, (f) Variation of the forgetting factor λ; Dashed: Magnitude of sequence and harmonic component phasor.

7.4 Experimental results on control of E-STATCOM

To evaluate the inner-loop current controller and AC voltage controller experimentally, the setup in Fig. 7.1 is used. Using a constant DC-link voltage, the basic and improved current controllers are tested by connecting the VSC directly to the stiff AC grid by closing contactor 1 and opening contactor 2. The grid voltage contains about 0.015 pu 5^{th} and 7^{th} order harmonics among others as shown in Fig. 7.7, where the FFT of the phase-to-ground grid voltage (phase a) is depicted. The parameters for the tests are given in Table 7.3.

TABLE 7.3. PARAMETERS OF THE CONTROLLERS

Sampling time, T_{s}	0.2 ms
Switching frequency f_{s}	5 kHz
Current controller bandwidth, γ_{cc}	2513.3 rad/s
Active damping, R_{a}	0.0502 Ω
harmonic compensator bandwidth, γ_{hc}	628.3 rad/s
Active damping, R_{ha}	0.0625 Ω
AC voltage controller bandwidth, γ_{vc}	125.7 rad/s
Droop constant, m	0.0 pu

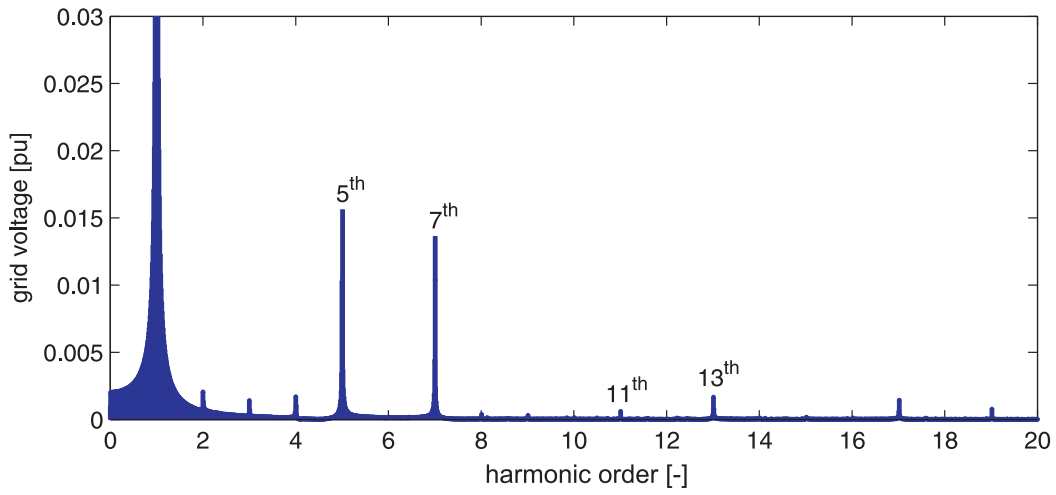

Fig. 7.7 FFT of measured phase-to-ground grid voltage.

Figure 7.8 shows the performance of the basic and improved current controllers for a step in dq current reference. The improved current controller has been designed to set to zero the 5^{th} and 7^{th} order current harmonic injected into the grid.

From the FFT in Fig. 7.7, it can be observed that the grid contains other harmonics in addition to the considered ones. Therefore, to see the effect of the improved controller on the 5^{th} and 7^{th} harmonics, the three phase current response (Fig. 7.9 (top)) is filtered to remove all disturbances except the 5^{th} and 7^{th} harmonics as in Fig. 7.9 (b, d). The FFT of the resulting filter current when using the two controllers is shown in Fig. 7.10. As can be seen from the results, the improved current controller successfully removes the 5^{th} and 7^{th} order harmonic injection to the grid.

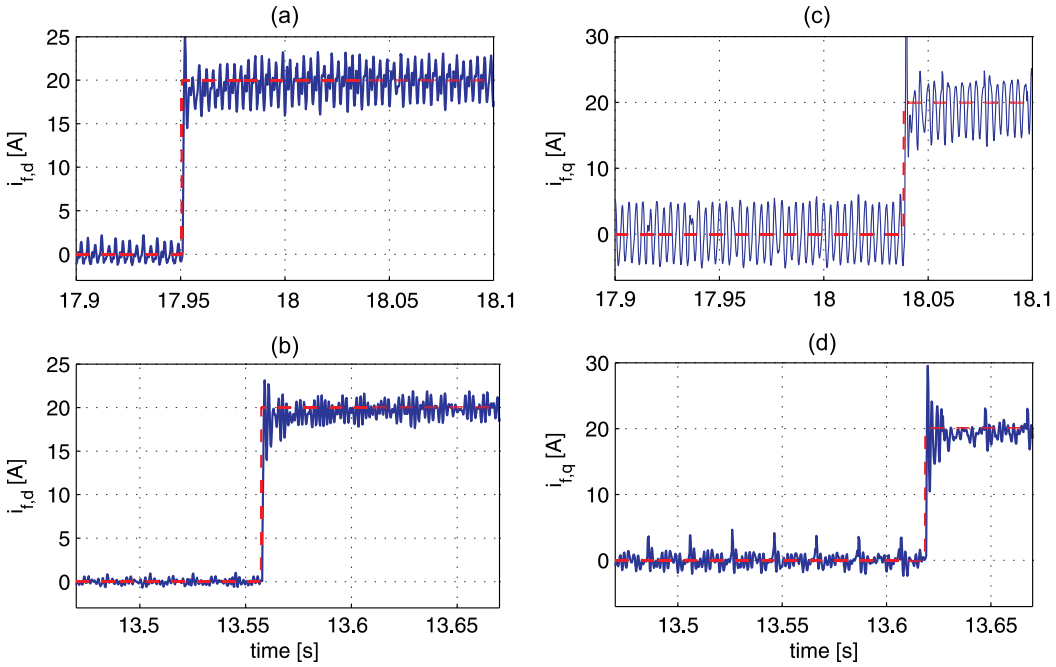

Fig. 7.8 Dynamic performance of vector current controller for a step in current reference (dashed curves); basic current controller response for d-component current (plot a) and q-component current (plot c); improved current controller response for d-component current (b) and q-component current (d).

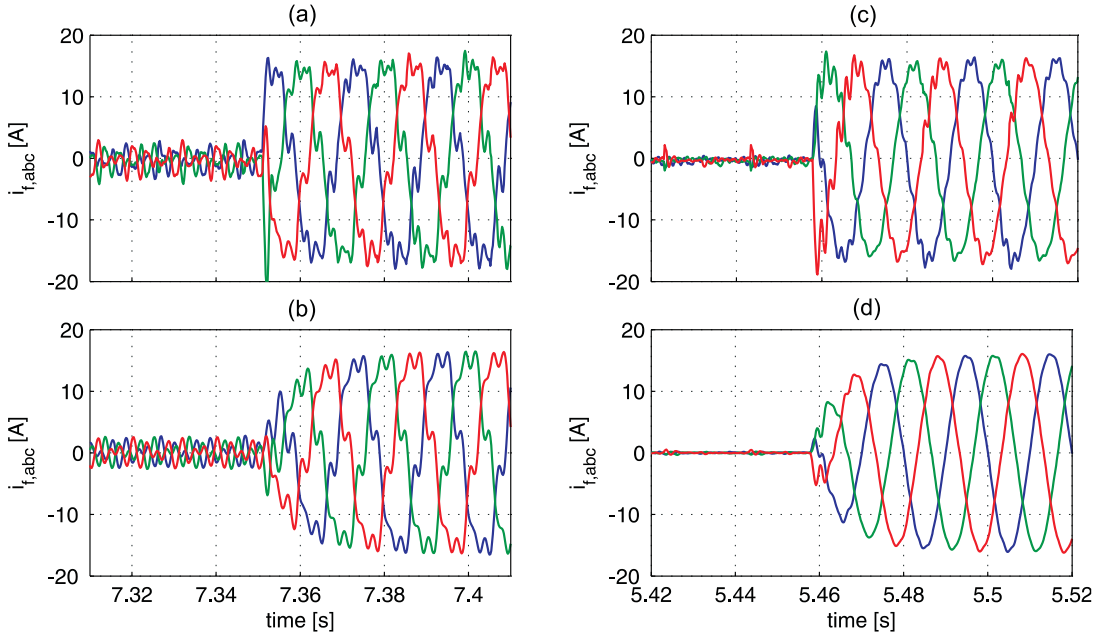

Fig. 7.9 three phase current controller response; (a, b) basic current controller, (c,d) improved current controller, (a, c) actual current and (b, d) filtered current to remove disturbances other than the 5^{th} the 7^{th} order harmonics.

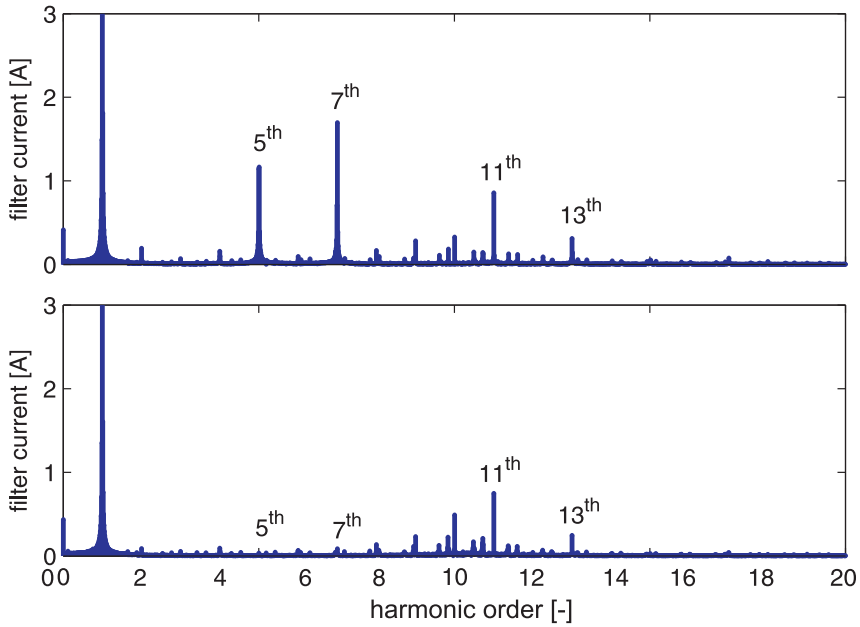

Fig. 7.10 FFT for the phase filter current when basic current controller used (top) and improved current controller used (bottom).

The AC voltage controller, with no droop, has been tested using the same setup as in Fig. 7.1. In this case, the VSC is connected to a weaker point in the transmission line (three Π sections from the strong grid) by closing contactor 2 and opening contactor 1. As this is a weak connection point, a filter capacitor C_{f} of 152 μF is used to strengthen the grid at PCC. The test was made while transferring a power of 0.2 pu from the synchronous generator to the AC grid. Figure 7.11 shows the response of the AC voltage controller for a small step in the reference for grid voltage magnitude, E_{g}. As shown in the filtered voltage response, the system is able to follow the voltage reference with the desired bandwidth.

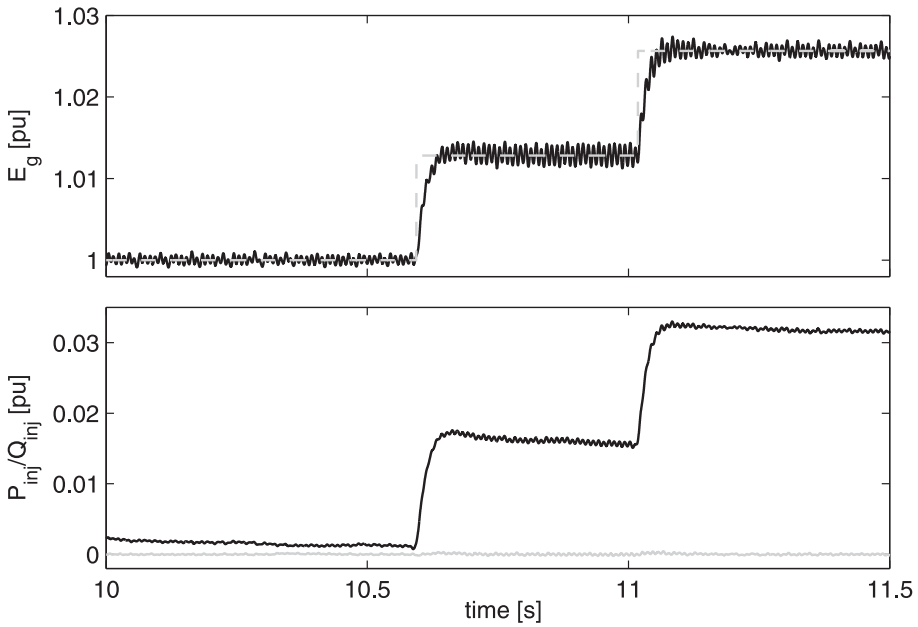

Fig. 7.11 Dynamic performance of AC voltage controller; Top: Magnitude of grid voltage reference (gray dashed), measured average voltage(black); Bottom: Injected average active power (gray) and reactive power (black).

7.5 Experimental results on POD and TSE by E-STATCOM

To verify the power oscillation damping and transient stability enhancement controllers, the setup in Fig. 7.1, which represents a single machine infinite bus system with E-STATCOM, is used. The single line diagram of the setup is shown in Fig. 7.12, where the synchronous generator is connected to an infinite bus through six Π sections of the transmission line model (without the shunt capacitors). The possible connection points of the E-STATCOM are marked as 1, 2 and 3.

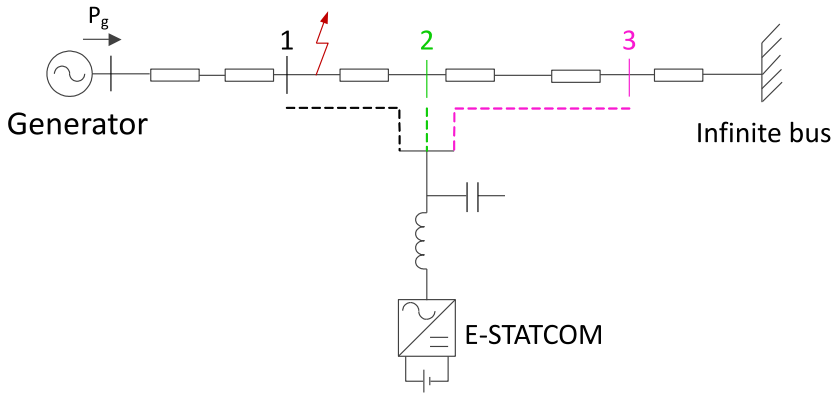

Fig. 7.12 Single line diagram of the laboratory setup for POD and TSE.

The gain values are adjusted to get the desired damping performance at bus 2 first. These values are then kept constant for all the experiments. Based on the available active and reactive power

from the converter and level of damping or transient stability enhancement needed, the gains can be chosen. First, the power oscillation damping controller is tested with three connection points of the E-STATCOM as shown in Fig. 7.12. A three-phase fault is applied at bus 1 for 250 ms and the performance of the E-STATCOM for POD using the control strategy described in Section 6.3.1 is shown in Fig. 7.13. As described in the small signal analysis in Section 6.4.2 and as shown in the measurements depicted in Fig. 7.14, the injected active power decreases with the distance from the generator where its effect to provide damping decreases. The maximum damping with active power injection is obtained when the E-STATCOM is closer to the generator, in this case at bus 1. With respect to reactive power injection, the level of additional damping provided by the compensator decreases when moving away from the electrical midpoint. As the transmitted power P_{g} is used to control reactive power, the same amount of injected reactive power is used at the three locations and maximum damping action is provided around electrical midpoint of the line, in this case at bus 2, thanks to the larger voltage modulation. When moving closer to the infinite bus, in this case at bus 3, damping provided by the POD controller decreases, in accordance with the analysis shown in Fig. 6.8. With both active and reactive power injection, effective power oscillation damping is provided by the E-STATCOM at various connection points except, of course, when the compensator is connected close to the infinite bus.

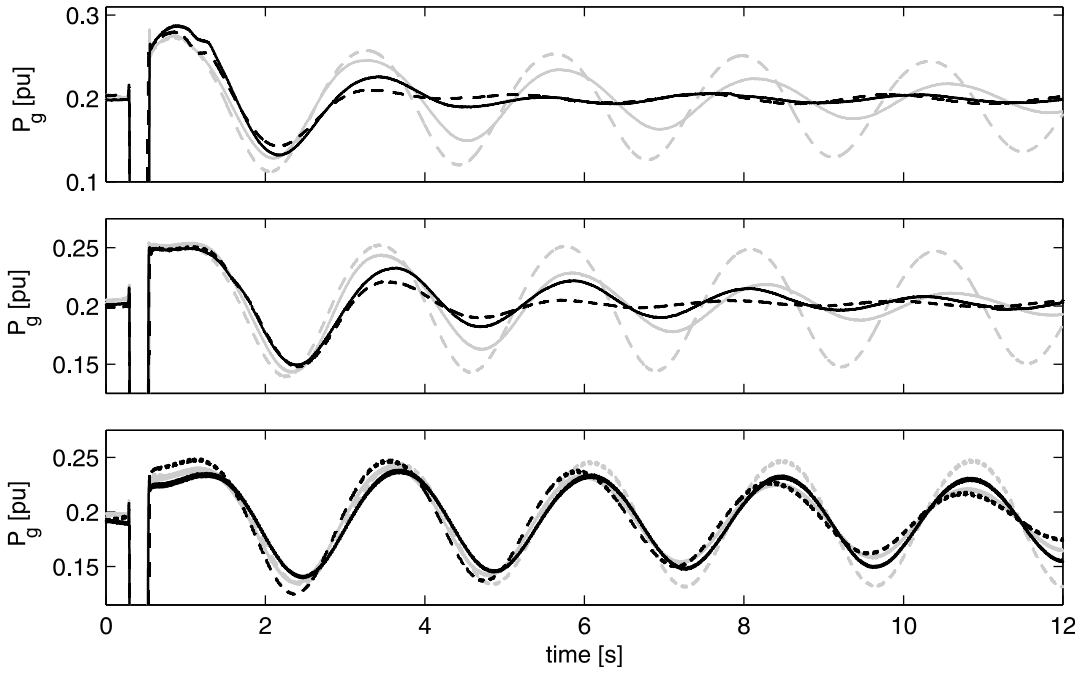

Fig. 7.13 Measured generator active power output following a three phase fault with E-STATCOM connected at bus 1 (top), bus 2 (middle) and bus 3 (bottom). POD by P_{inj} only (black solid), Q_{inj} only (gray solid), both P_{inj}, Q_{inj} (black dashed) and no POD (gray dashed).

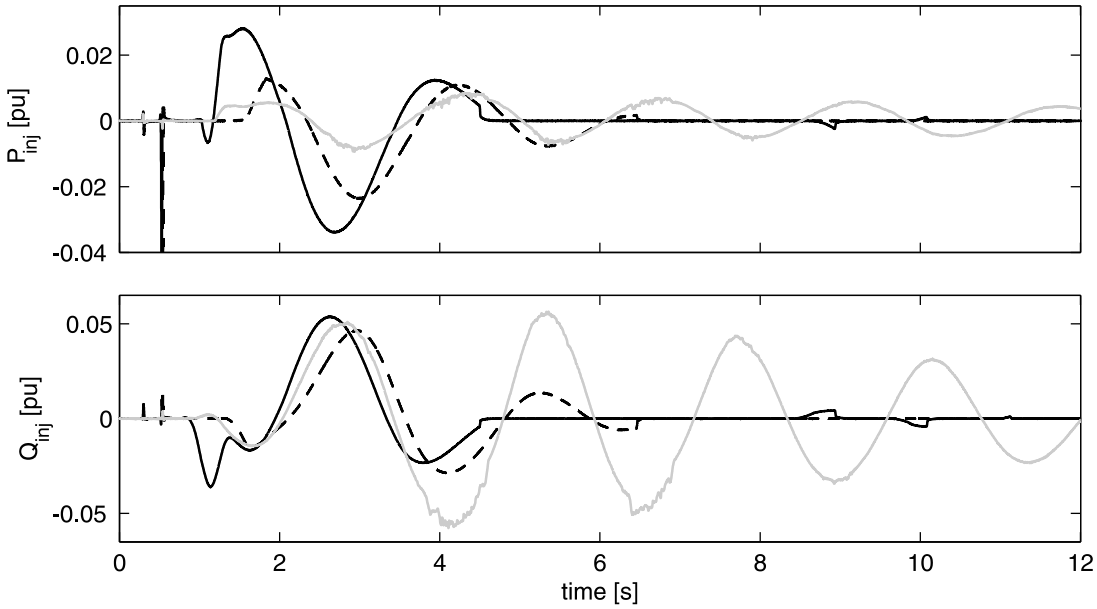

Fig. 7.14 Injected active and reactive power with E-STATCOM connected at bus 1 (black solid), bus 2 (black dashed) and bus 3 (gray solid). Active power injection (top); reactive power injection (bottom); both P_{inj} and Q_{inj} used for POD.

For the test described in Fig. 7.13 and 7.14, knowledge of the the oscillatory frequency in the transmitted active power has been considered. To test the dynamic performance of the investigated POD controller in case of inaccurate knowledge of the oscillation frequency, a second set of experiments has been carried out assuming an oscillation frequency $\omega_{\text{osc}} = 0.9$ Hz, where the actual measured oscillation frequency is 0.4 Hz. This means that an error of 100% in the estimated oscillateion frequency is here considered. Figure 7.15 shows the dynamic performance of the RLS, where both the resetting and frequency adaptation methods are implemented. With the E-STATCOM connected at bus 2, Fig. 7.16 compares the performance of the POD controller with and without the oscillation frequency adaptation. By using the frequency adaption, the phase of the oscillatory component in the input signal is corrected, thus providing a better damping. This is advantageous when compared to the use of lead-lag filter links, where the right phase shift is provided only at a particular oscillation frequency.

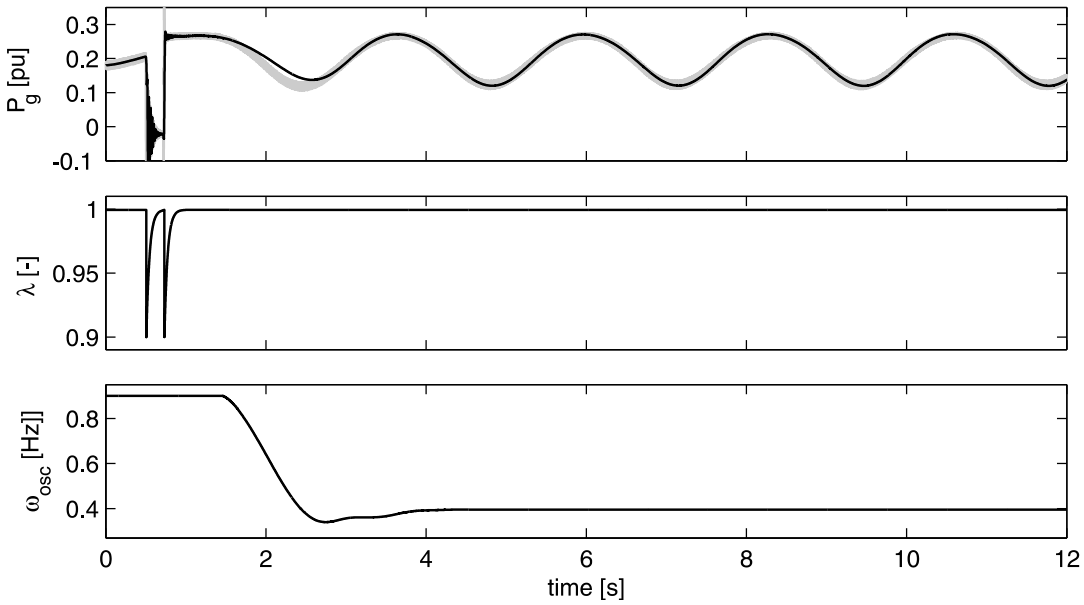

Fig. 7.15 Improved RLS based estimator; Top: Measured (gray) and estimated (black) generator active power; Middle: Variation of forgetting factor λ; Bottom: Estimated power oscillation frequency $\tilde{\omega}_{\mathrm{osc}}$.

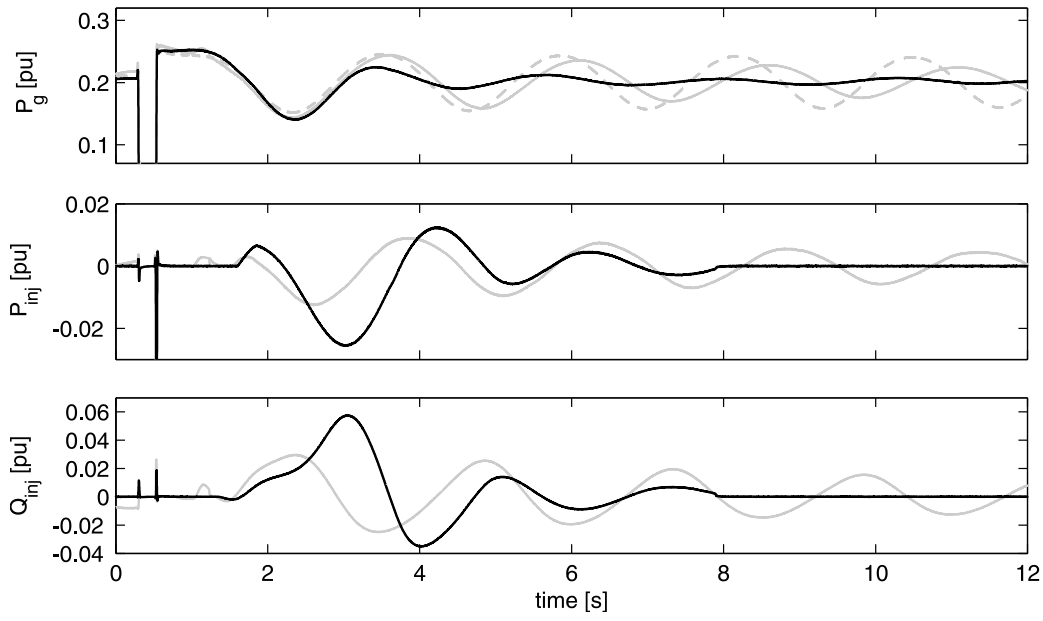

Fig. 7.16 Top: measured generator output power with frequency adaptation (black solid), without frequency adaptation (gray solid) and with no POD (gray dashed); Middle: Injected active power with frequency adaptation (black) and without frequency adaptation (gray); Bottom: Injected reactive power with frequency adaptation (black) and without frequency adaptation (gray).

On the other hand, by using the resetting of the forgetting factor, a faster estimation can be achieved. Figure 7.17 compares the performance of the POD controller with and without the forgetting factor resetting. If no resetting is used, the RLS estimator behaves like a LPF in steady state (see Section 4.2.2). Therefore, due to its limited speed, larger active and reactive power is injected in beginning of the damping operation. When the resetting function in the RLS is enabled, fast estimation of both the amplitude and phase of the oscillatory component in the transmitted active power can be achieved. Being able to know the phase of the oscillatory component faster as compared with the conventional RLS, leads to a smaller amount of required power. The use of the resetting method would be even more evident in case of multi-machine system with more than one oscillation frequency components that are close to each other.

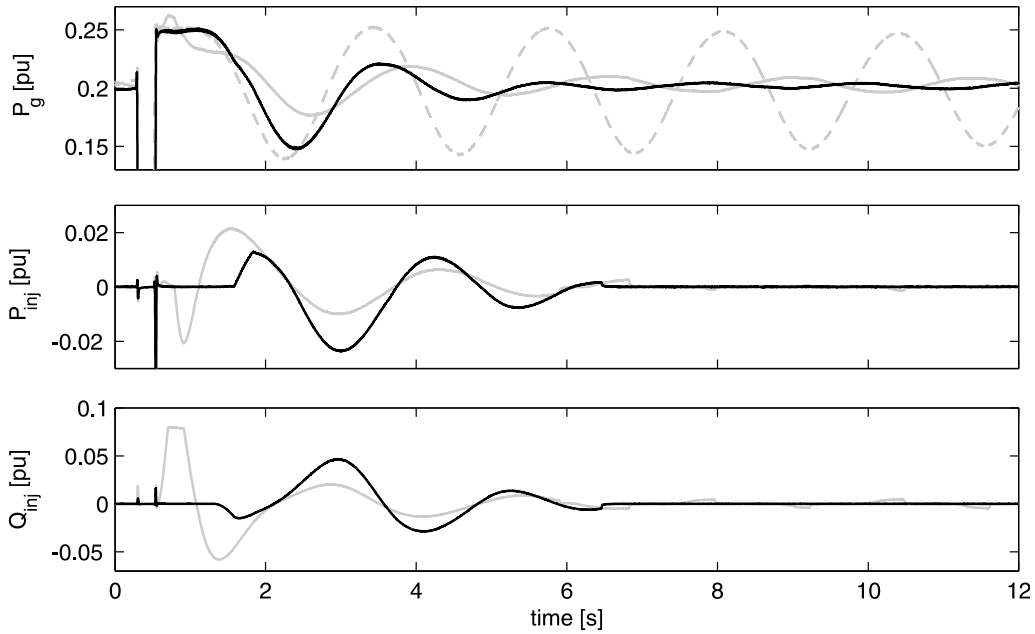

Fig. 7.17 Top: measured generator output power with λ resetting (black solid), without λ resetting (gray solid) and no POD (gray dashed); Middle: Injected active power with λ resetting (black) and without λ resetting (gray); Bottom: Injected reactive power with λ resetting(black) and without λ resetting(gray).

Even if the power oscillation can be damped using the POD controller as described, a transient stability enhancement function is required to keep the generator from losing synchronism after fault clearing. The tendency of the generator to lose synchronism increases with the fault clearing time and the amount of transmitted active power. Thus, a larger fault clearing time of 350 ms is considered for a three-phase fault applied at bus 1 in Fig. 7.12. With the E-STATCOM connected at bus 2, Fig. 7.18 shows the TSE controller performance immediately after fault clearing. Here, the TSE has been implemented to guarantee first angle stability only and then the compensator is operated in voltage control mode, in order appreciate the need for a damping controller after the system stabilization. As shown in the figure, the generator power output is increased when the TSE function is started (see the dashed circle in Fig. 7.18) and this increases the stability margin of the system. The TSE function is achieved by absorbing a constant active power (gray curves in the figure) or by controlling the PCC voltage E_{g} to 1.05 pu using

reactive power (black curves) to achieve a first swing stability enhancement as described in Section 6.3.2. Due to the limited reactive power, the required reference voltage of $E_{\mathrm{g}} = 1.05$ pu is not achieved.

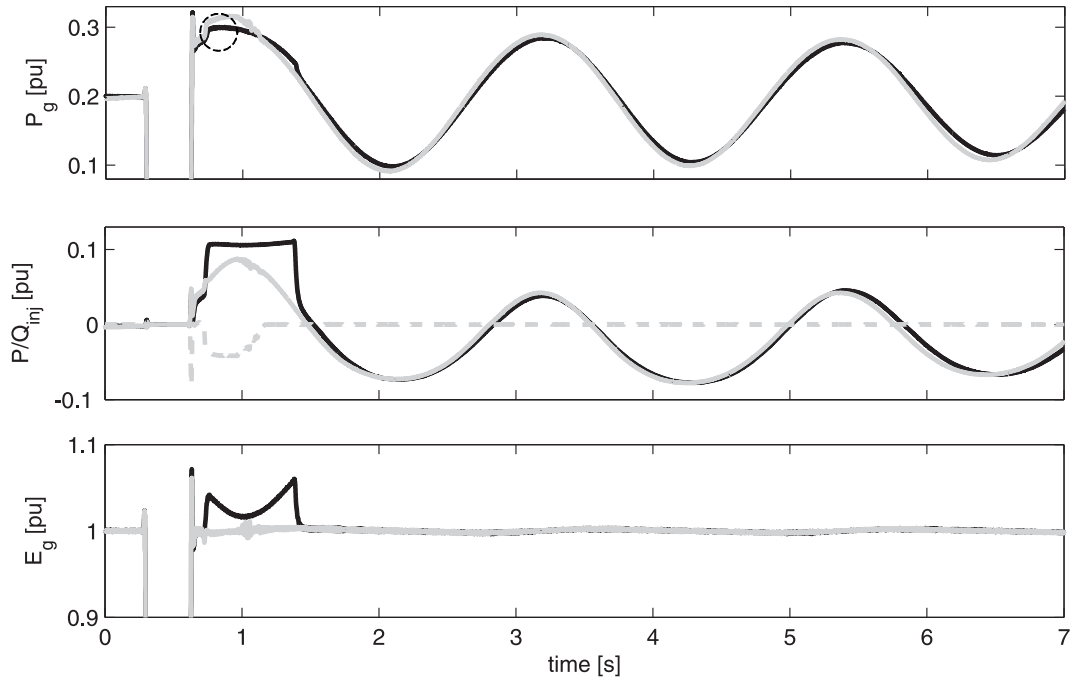

Fig. 7.18 Top: measured generator output power; middle: active and reactive power injected by the E-STATCOM; bottom: amplitude of PCC voltage. Black curves: reactive power injection only, used for voltage control and TSE; gray curves: reactive power injection used for voltage control only and active power injection (gray dashed in the middle plot) used for TSE.

As it can be seen in Fig. 7.18, The TSE function only provides more deceleration area to achieve a first swing stability enhancement. As expected, no damping is provided by the voltage controller. The same test is performed with also the damping controller activated. The performance of the TSE and POD controllers together is shown in Fig. 7.19. Immediately after fault clearing, the TSE function starts (similar to Fig. 7.18) followed by the POD function. The derivative of the measured active power leads to an activation of the TSE function for the first swing only. When damping is provided by reactive power injection, the PCC voltage is modulated around the nominal voltage (see black curves in Fig. 7.19). On the other hand, using active power injection, the PCC voltage magnitude can be kept constant and additional damping can be provided (see gray curves in Fig. 7.19). In this case, the limit of the reactive power is hit only during the TSE interval.

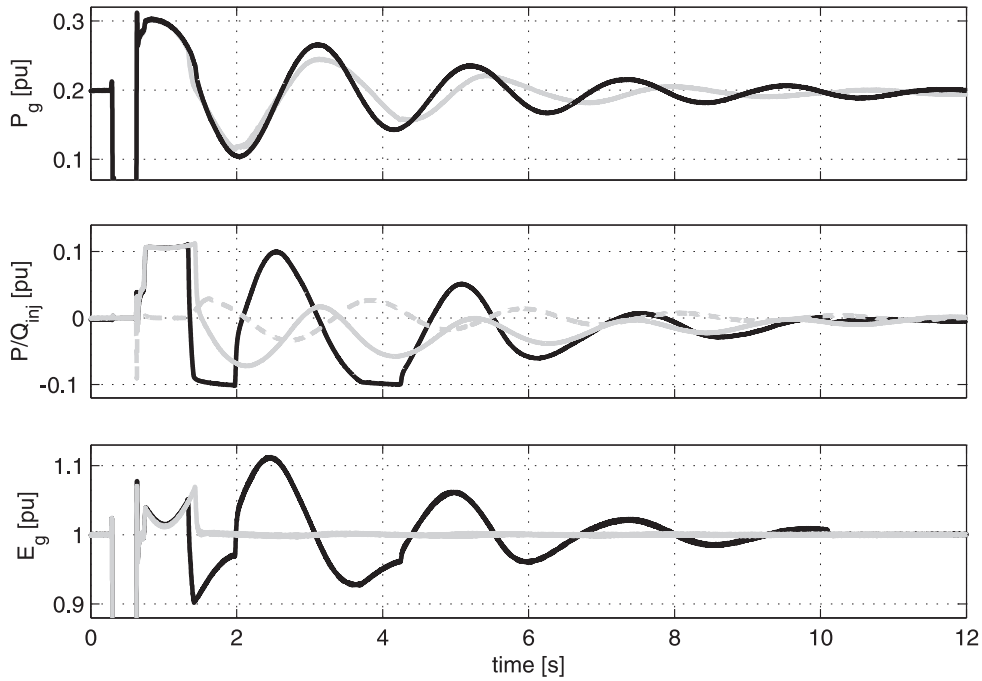

Fig. 7.19 Top: measured generator output power; middle: active and reactive power injected by the E-STATCOM; bottom: amplitude of PCC voltage. Black curves: reactive power injection used for voltage control, TSE and POD; gray curves: reactive power injection used for voltage control and TSE and active power injection (gray dashed in the middle plot) used for POD.

7.6 Conclusions

In this chapter, theoretical results on improved RLS based estimator, control of shunt-connected E-STATCOM and power system stability enhancement by E-STATCOM presented in the previous chapters have been verified through experiment. A description of the laboratory setup used for the experiments has been given and the different tests have been carried out. The performance of the improved RLS based estimator for estimation of low-frequency electromechanical oscillations, harmonics and sequence components has been shown. These results are used for design of an improved current controller and a POD controller. The performance of the improved current controller in distorted grids and the AC voltage controller has been shown. The robustness of the control algorithm for POD and TSE using E-STATCOM has been investigated. It has been shown that injection of active power for POD is minimized at locations in the power system where its effect is negligible, confirming the theoretical investigation. Using both active and reactive power injection with the control strategy as described in Section 6.3, it has been shown that stability enhancement can be achieved at several connection points of the E-STATCOM in the transmission line. Through the experimental results, it has been shown that the simulation results are verified.

Chapter 8

Conclusions and future work

8.1 Conclusions

This thesis has dealt with the application of the energy-storage equipped shunt-connected voltage source converter (here named E-STATCOM) for power system stability enhancement. In particular, the focus of the thesis has been on Power Oscillations Damping (POD) and Transient Stability Enhancement (TSE). The final aim of this work has been to identify a control strategy that allows stability enhancement from the compensator with low amount of injected active power, leading to a cost-effective utilization of the energy storage. For this purpose, accurate knowledge of the oscillatory modes in the measured signals is needed. A control algorithm for POD has been developed using a signal estimation technique based on Recursive Least Square (RLS) algorithm in Chapter 4. Advantages of the RLS over other signal estimation techniques based on the use of filters have been highlighted. Improvements to the conventional RLS approach to give a fast speed of response and still guarantee its steady state selectivity have been proposed. Furthermore, a method to be able to cope with inaccurate knowledge of the oscillatory frequency, which makes the estimation algorithm frequency adaptive, has been derived. The resulting RLS algorithm (here named Improved RLS) gives a fast and selective estimation of low-frequency electromechanical oscillations in the measured signals. The obtained estimates are then used to develop the POD controller. The investigated estimation algorithm also allows estimation of sequence and harmonic components in the measured quantities, allowing satisfactory performance of the system in case of non-ideal conditions of the grid voltage.

The control of the E-STATCOM for power system stability enhancement has been developed using a simplified two-machine power system model in Chapter 6. This simple model has also been utilized to investigate the impact of active and reactive power modulation as a function of the location of the compensator in the power system. The POD and TSE controllers have been designed using estimation of the low-frequency electromechanical oscillations following disturbances as described in Chapter 4. The robustness of the control algorithm against system parameter variation has been shown both via simulation and through an experimental setup that has been built in the Power System Laboratory at the Department of Energy and Environment at Chalmers University of Technology. By using the estimate of the grid frequency, obtained from

the Phase-Locked Loop (PLL), and the measured active power flowing in the line in conjunction with the proposed Improved RLS to control the injected active and reactive power, respectively, the E-STATCOM is able to guarantee a uniform stability enhancement regardless of its location in the power network. Furthermore, selecting the frequency variation at the connection point as the input signal for the active power modulation allows the minimization of active power injection in points of the power system where its impact on POD would be negligible, i.e. in the vicinity of the mass-scaled electrical midpoint of the line.

8.2 Future work

The main focus of the thesis has been on the development and the analysis of an energy efficient control algorithm for power oscillation damping and transient stability enhancement using combined active and reactive power injection. The investigation carried out in this thesis has been made under the assumption of having an infinitely large energy storage connected to the DC-link of the voltage source converter. It can be of interest to expand the analysis by implementing the model of an actual energy storage (for example, batteries) and investigate the impact of its dynamics as well as the limited amount of available energy on the implemented control strategy.

The dynamic performance of the system has been investigated by using a simple two machine model of the power system. In order to isolate the contribution of the compensator, the power system model did not include other components, such as loads or other dynamic components. A natural next step is to consider a larger power system model which includes also these components. However, in a large power system, which includes many generation units, loads (both static and dynamic) and compensators, interaction between different controllable objects can lead to system destabilization. This requires a coordinated control of various controllable objects for reliable operation of the power system. Therefore, the control strategy developed for a single compensator should be adapted for controlling distributed power electronics devices (STATCOMs, SVCs but also, for example, wind power plants) to provide power system stability enhancement in a large power system. For this, the interaction that could arise among the different controllable objects and loads should be studied in detail and a coordinated control algorithm that is robust against system parameter changes and does not lead to interactions between the various controllable objects and loads should be developed.

References

[1] N. G. Hingorani and L. Gyugyi, *Understanding FACTS. Concepts and technology of Flexible AC Transmission Systems*. New York: IEEE Press, 2000.

[2] G. Andersson, P. Donalek, R. Farmer, N. Hatziargyriou, I. Kamwa, P. Kundur, N. Martins, J. Paserba, P. Pourbeik, J. Sanchez-Gasca, R. Schulz, A. Stankovic, C. Taylor, and V. Vittal, "Causes of the 2003 major grid blackouts in north america and europe, and recommended means to improve system dynamic performance," *Power Systems, IEEE Transactions on*, vol. 20, no. 4, pp. 1922 – 1928, Nov. 2005.

[3] M. Klein, G. J. Rogers and P. Kundur, "A fundamental study of inter-area oscillations in power systems," *IEEE Trans. on Power Syst.*, vol. 6, no. 3, pp. 914–921, Aug. 1991.

[4] A. Domahidi, B. Chaudhuri, P. Korba, R. Majumder, and T. Green, "Self-tuning flexible ac transmission system controllers for power oscillation damping: a case study in real time," *Generation, Transmission Distribution, IET*, vol. 3, no. 12, pp. 1079 –1089, Dec. 2009.

[5] L. Ängquist and C. Gama, "Damping algorithm based on phasor estimation," in *Power Engineering Society Winter Meeting, 2001. IEEE*, vol. 3, 2001, pp. 1160 –1165 vol.3.

[6] L. Ängquist, B. Lundin and J. Samuelsson, "Power oscillation damping using controlled reactive power compensation - a comparison between series and shunt approaches," *IEEE Trans. on Power Syst.*, vol. 8, no. 2, pp. 687–700, May 1993.

[7] M. Haque, "Improvement of first swing stability limit by utilizing full benefit of shunt facts devices," *Power Systems, IEEE Transactions on*, vol. 19, no. 4, pp. 1894 – 1902, Nov. 2004.

[8] G. Shahgholian, P. Shafaghi, S. Moalem, and M. Mahdavian, "Damping power system oscillations in single-machine infinite-bus power system using a statcom," in *Computer and Electrical Engineering, 2009. ICCEE '09. Second International Conference on*, vol. 1, Dec. 2009, pp. 130 –134.

[9] G. Cao, Z. Y. Dong, Y. Wang, P. Zhang and Y. T. Oh, "VSC based STATCOM controller for damping multi-mode oscillations," in *Power and Energy Society General Meeting - Conversion and Delivery of Electrical Energy in the 21st Century, 2008 IEEE*, July 2008, pp. 1–8.

References

[10] M. Zarghami and M. Crow, "Damping inter-area oscillations in power systems by STATCOMs," in *Power Symposium, 2008. NAPS '08. 40th North American*, Sept. 2008, pp. 1 –6.

[11] J. Svensson, P. Jones and P. Halvarsson, "Improved power system stability and reliability using innovative energy storage technologies," in *Proc. of* 8^{th} *IEEE International Conference on AC and DC Power Transmission*, vol. 2, Mar. 2006, pp. 220–224.

[12] Z. Yang, C. Shen, L. Zhang, M.L. Crow and S. Atcitty, "Integration of a statcom and battery energy storage," *IEEE Trans. on Power Sys.*, vol. 16, no. 2, pp. 254–260, May 2001.

[13] A. Arsoy, Y. Liu, S. Chen, Z. Yang, M. L. Crow and P. F. Ribeiro, "Dynamic performance of static synchronous compensator with energy storage," in *IEEE Power Engineering Society Winter Meeting*, vol. 2, Jan. 2001, pp. 605–610.

[14] A. Arulampalam, J. B. Ekanayake and N. Jenkins, "Application study of a STATCOM with energy storage," in *Generation, Transmission and Distribution, IEE Proceedings*, vol. 150, July 2003, pp. 373–384.

[15] N. Wade, P. Taylor, P. Lang, and J. Svensson, "Energy storage for power flow management and voltage control on an 11 kV UK distribution network," CIRED paper 0824, Prague, Czech Republic, June 2009.

[16] P. Lang, N. Wade, P. Taylor, P. Jones, and T. Larsson, "Early findings of an energy storage practical demonstration," in 21^{st} *International Conference on Electricity Distribution*, 2011, The Institution of Engineering and Technology, paper no. 0413.

[17] A. Adamczyk, R. Teodorescu, and P. Rodriguez, "Control of full-scale converter based wind power plants for damping of low frequency system oscillations," in *PowerTech, 2011 IEEE Trondheim*, June 2011, pp. 1 –7.

[18] N. R. Ullah and T. Thiringer, "Variable speed wind turbines for power system stability enhancement," *Energy Conversion, IEEE Transactions on*, vol. 22, no. 1, pp. 52 –60, Mar. 2007.

[19] H. Xie, "On Power-system Benefits, Main-circuit Design, and Control of Statcoms with Energy Storage," Ph.D. dissertation, Royal Institute of Technology (KTH), Stockholm, Sweden, 2009.

[20] K. Kobayashi, M. Goto, K. Wu, Y. Yokomizu and T. Matsumura, "Power system stability improvement by energy storage type STATCOM," in *Proc. of IEEE Power Tech Conference in Bologna*, vol. 2, June 2003.

[21] L. Zhang and Y. Liu, "Bulk power system low frequency oscillation suppression by FACTS/ESS," in *Power Systems Conference and Exposition, 2004. IEEE PES*, Oct. 2004, pp. 219–226.

[22] R. Kuiava, R. A. Ramos and N. G. Bretas, "Control design of a STATCOM with energy storage system for stability and power quality improvements," in *IEEE International Conference on Industrial Technology, 2009. ICIT 2009.*, Feb. 2009, pp. 1–6.

[23] A. Arsoy, Liu Yilu, P. F. Ribeiro and F. Wang, "Power converter and SMES in controlling power system dynamics," in *Industry Applications Conference, 2000*, vol. 4, Oct. 2000, pp. 2051–2057.

[24] P. Kundur, *Power System Stability and Control*. United States of America: McGraw-Hill, 1994.

[25] J. Machowski, J. W. Bialek, and J. R. Bumby, *Power System Dynamics and Stability*. United States of America: John Wiley and Sons, 1997.

[26] M. Bongiorno, "On Control of Grid-Connected Voltage Source Converters," Ph.D. dissertation, Chalmers University of Technology, Gothenburg, Sweden, 2007.

[27] L. Ängquist, "Synchronous Voltage Reversal Control of Thyristor Controlled Series Capacitor," Ph.D. dissertation, Royal Institute of Technology (KTH), Stockholm, Sweden, 2002.

[28] M. Beza and M. Bongiorno, "A fast estimation algorithm for low-frequency oscillations in power systems," in *Power Electronics and Applications (EPE 2011), Proceedings of the 2011-14th European Conference on*, 30 2011-Sept. 1 2011, pp. 1 –10.

[29] ——, "Application of recursive least square (RLS) algorithm with variable forgetting factor for frequency components estimation in a generic input signal," in *Energy Conversion Congress and Exposition (ECCE), 2012 IEEE*, Sept. 2012 [*Accepted for publication*].

[30] K. J. Åström and B. Wittenmark, *Adaptive Control*. Addison-Wesley, 1995.

[31] A. Vidal, F. Freijedo, A. Yepes, P. Fernandez-Comesañ anda, J. Malvar, O. Lopez, and J. Doval-Gandoy, "A fast, accurate and robust algorithm to detect fundamental and harmonic sequences," in *Energy Conversion Congress and Exposition (ECCE), 2010 IEEE*, Sept. 2010, pp. 1047 –1052.

[32] H.-S. Song, K. Nam, and P. Mutschler, "Very fast phase angle estimation algorithm for a single-phase system having sudden phase angle jumps," in *Industry Applications Conference, 2002. 37th IAS Annual Meeting. Conference Record of the*, vol. 2, Oct. 2002, pp. 925 –931 vol.2.

[33] P. Rodriguez, A. Luna, I. Candela, R. Mujal, R. Teodorescu, and F. Blaabjerg, "Multiresonant frequency-locked loop for grid synchronization of power converters under distorted grid conditions," *Industrial Electronics, IEEE Transactions on*, vol. 58, no. 1, pp. 127 –138, Jan. 2011.

[34] A. Timbus, T. Teodorescu, F. Blaabjerg, M. Liserre, and P. Rodriguez, "PLL algorithm for power generation systems robust to grid voltage faults," in *Power Electronics Specialists Conference, 2006. PESC '06. 37th IEEE*, June 2006, pp. 1 –7.

[35] P. Rodriguez, R. Teodorescu, I. Candela, A. Timbus, M. Liserre, and F. Blaabjerg, "New positive-sequence voltage detector for grid synchronization of power converters under faulty grid conditions," in *Power Electronics Specialists Conference, 2006. PESC '06. 37th IEEE*, June 2006, pp. 1 – 7.

[36] L. Harnefors, "Modeling of three-phase dynamic systems using complex transfer functions and transfer matrices," *Industrial Electronics, IEEE Transactions on*, vol. 54, no. 4, pp. 2239 –2248, Aug. 2007.

[37] L. Ängquist and M. Bongiorno, "Auto-normalizing phase-locked loop for grid-connected converters," in *Energy Conversion Congress and Exposition, 2009. ECCE 2009. IEEE*, Sept. 2009, pp. 2957 –2964.

[38] N. Mohan, T. M. Underland, and W. P. Robbins, *Power Electronics: Converters, Applications and Design*. United States of America: John Wiley and Sons, 2003.

[39] M. Bongiorno, "Control of voltage source converters for voltage dip mitigation in shunt and series configurations," Chalmers University of Technology, Gothenburg, Sweden, Licentiate Thesis, 2004.

[40] R. Teodorescu, F. Blaabjerg, M. Liserre, and P. Loh, "Proportional-resonant controllers and filters for grid-connected voltage-source converters," *Electric Power Applications, IEE Proceedings* -, vol. 153, no. 5, pp. 750 –762, september 2006.

[41] L. Zhang, L. Harnefors, and H.-P. Nee, "Power-synchronization control of grid-connected voltage-source converters," *Power Systems, IEEE Transactions on*, vol. 25, no. 2, pp. 809 –820, may 2010.

[42] J. Hu, Y. He, L. Xu, and D. Zhi, "Predictive current control of grid-connected voltage source converters during," *Power Electronics, IET*, vol. 3, no. 5, pp. 690 –701, september 2010.

[43] L. Harnefors, L. Zhang, and M. Bongiorno, "Frequency-domain passivity-based current controller design," *Power Electronics, IET*, vol. 1, no. 4, pp. 455 –465, Dec. 2008.

[44] L. Harnefors and H.-P. Nee, "Model-based current control of ac machines using the internal model control method," *Industry Applications, IEEE Transactions on*, vol. 34, no. 1, pp. 133 –141, Jan./Feb. 1998.

[45] M. Beza and M. Bongiorno, "Improved discrete current controller for grid-connected voltage source converters in distorted grids," in *Energy Conversion Congress and Exposition (ECCE), 2012 IEEE*, Sept. 2012 [*Accepted for publication*].

[46] E. Adzic, D. Marcetic, V. Katic, and M. Adzic, "Grid-connected voltage source converter operation under distorted grid voltage," in *Power Electronics and Motion Control Conference (EPE/PEMC), 2010 14th International*, Sept. 2010, pp. T11–44 –T11–51.

[47] Y. Quan, H. Nian, J. Hu, and J. Li, "Improved control of the grid-connected converter under the harmonically distorted grid voltage conditions," in *Electrical Machines and Systems (ICEMS), 2010 International Conference on*, Oct. 2010, pp. 204 –209.

[48] P. Chapman and S. Sudhoff, "A multiple reference frame synchronous estimator/regulator," *Energy Conversion, IEEE Transactions on*, vol. 15, no. 2, pp. 197 –202, June 2000.

[49] P. Mattavelli, "Synchronous-frame harmonic control for high-performance ac power supplies," *Industry Applications, IEEE Transactions on*, vol. 37, no. 3, pp. 864 –872, May/June 2001.

[50] M. Bongiorno and J. Svensson, "Voltage dip mitigation using shunt-connected voltage source converter," *Power Electronics, IEEE Transactions on*, vol. 22, no. 5, pp. 1867 –1874, Sept. 2007.

[51] H. Xie, L. L. Ängquist, and H.-P. Nee, "Design study of a converter interface interconnecting an energy storage with the dc-link of a vsc," in *Innovative Smart Grid Technologies Conference Europe (ISGT Europe), 2010 IEEE PES*, oct. 2010, pp. 1 –9.

[52] M. Beza and M. Bongiorno, "Power oscillation damping controller by static synchronous compensator with energy storage," in *Energy Conversion Congress and Exposition (ECCE), 2011 IEEE*, Sept. 2011, pp. 2977 –2984.

[53] DS1103 PPC Controller Board, *Hardware Installation and Configuration*. Germany: dSPACE GmbH, 2009.

[54] M. Gustafsson and N. Krantz, "Voltage collapse in power systems," Chalmers University of Technology, Gothenburg, Sweden, Licentiate Thesis TR-215L, Dec. 1995.

References

Appendix A

Transformations for three phase systems

A.1 Introduction

In this appendix, the necessary transformations from three phase quantities into vectors in stationary $\alpha\beta$ and rotating dq reference frames and vise versa will be described.

A.2 Transformation of three phase quantities to vectors

A three phase system constituted by three quantities $v_1(t)$, $v_2(t)$ and $v_3(t)$ can be transformed into a vector $\underline{v}_{\alpha\beta}(t)$ in a stationary complex reference frame, usually called $\alpha\beta$-frame, by applying the transformation defined by (A.1).

$$\underline{v}_{\alpha\beta}(t) = v_\alpha(t) + \mathrm{j}v_\beta(t) = K_{\mathrm{tran}}(v_1(t) + v_2(t)e^{\mathrm{j}\frac{2}{3}\pi} + v_3(t)e^{\mathrm{j}\frac{4}{3}\pi}) \tag{A.1}$$

The transformation constant K_{tran} can be chosen to be $\sqrt{2/3}$ or $2/3$ to ensure power invariant or amplitude invariant transformation respectively between the two systems. Equation (A.1) can be expressed in matrix form as in (A.2).

$$\begin{bmatrix} v_\alpha(t) \\ v_\beta(t) \end{bmatrix} = T_{32} \begin{bmatrix} v_1(t) \\ v_2(t) \\ v_3(t) \end{bmatrix} \tag{A.2}$$

where the matrix T_{32} is given by

$$T_{32} = K_{\mathrm{tran}} \begin{bmatrix} 1 & -\frac{1}{2} & -\frac{1}{2} \\ 0 & \frac{\sqrt{3}}{2} & -\frac{\sqrt{3}}{2} \end{bmatrix}$$

The inverse transformation, assuming no zero-sequence, is given by (A.3).

$$\begin{bmatrix} v_1(t) \\ v_2(t) \\ v_3(t) \end{bmatrix} = T_{23} \begin{bmatrix} v_\alpha(t) \\ v_\beta(t) \end{bmatrix} \tag{A.3}$$

with the matrix T_{23} given by

$$T_{23} = \frac{1}{K_{\text{tran}}} \begin{bmatrix} \frac{2}{3} & 0 \\ -\frac{1}{3} & \frac{1}{\sqrt{(3)}} \\ -\frac{1}{3} & -\frac{1}{\sqrt{(3)}} \end{bmatrix}$$

A.3 Transformation between fixed and rotating coordinate systems

For the vector $\underline{v}_{\alpha\beta}(t)$ rotating in the $\alpha\beta$-frame with the angular frequency $\omega(t)$ in the positive (counter-clockwise) direction, a dq-frame that rotates in the same direction with the same angular frequency $\omega(t)$ can be defined. The vector $\underline{v}_{\alpha\beta}(t)$ will appear as fixed vectors in this rotating reference frame. A projection of the vector $\underline{v}_{\alpha\beta}(t)$ in the d-axis and q-axis of the dq-frame gives the components of the vector in the dq-frame as illustrated in Fig.A.1.

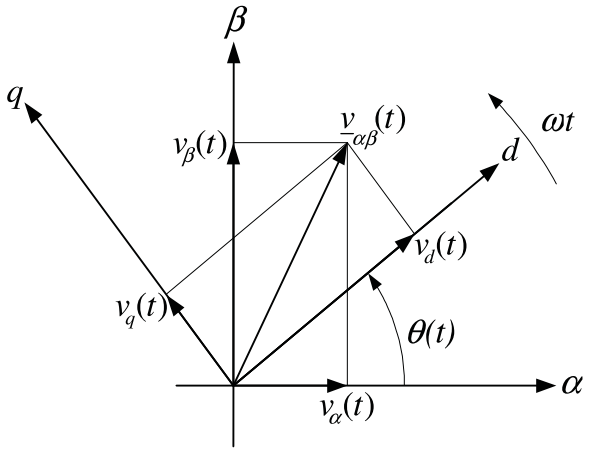

Figure A.1: Relation between $\alpha\beta$-frame and dq-frame.

The transformation can be written in vector form as in (A.4).

$$\underline{v}_{dq}(t) = v_d(t) + \mathrm{j}v_q(t) = \underline{v}_{\alpha\beta}(t)e^{-\mathrm{j}\theta(t)} \tag{A.4}$$

with the angle $\theta(t)$ in Fig.A.1 given by

$$\theta(t) = \theta_0 + \int_0^t \omega(\tau)d\tau$$

The inverse transformation, from the rotating dq-frame to the fixed $\alpha\beta$-frame is defined by (A.5).

$$\underline{v}_{\alpha\beta}(t) = \underline{v}_{dq}(t)e^{\mathrm{j}\theta(t)} \tag{A.5}$$

In matrix form, the transformation between the fixed $\alpha\beta$-frame and rotating dq-frame can be written as in (A.6) - (A.7).

$$\begin{bmatrix} v_d(t) \\ v_q(t) \end{bmatrix} = R(-\theta(t)) \begin{bmatrix} v_\alpha(t) \\ v_\beta(t) \end{bmatrix} \tag{A.6}$$

$$\begin{bmatrix} v_\alpha(t) \\ v_\beta(t) \end{bmatrix} = R(\theta(t)) \begin{bmatrix} v_d(t) \\ v_q(t) \end{bmatrix} \tag{A.7}$$

where the projection matrix is

$$R(\theta(t)) = \begin{bmatrix} \cos(\theta(t)) & -\sin(\theta(t)) \\ \sin(\theta(t)) & \cos(\theta(t)) \end{bmatrix}$$